ABSTRACT

Title of Dissertation:	CFD INVESTIGATION OF A PULSE JET MIXED VESSEL WITH RANS, LES, AND LBM SIMULATION MODELS
	Jung W. Kim, Doctor of Philosophy, 2022
Dissertation directed by:	Professor Richard V. Calabrese, Department of Chemical and Biomolecular Engineering

Pulse Jet Mixed (PJM) vessels are used to process nuclear waste due to their maintenance free operation. In this study we model the turbulent velocity field in water during normal PJM operation to gain insight into vessel operations and to evolve a modeling strategy for process design and operator training. Three transient simulation models, developed using Large Eddy Simulation (LES), unsteady Reynolds-Averaged Navier-Stokes (RANS), and Lattice Boltzmann Method (LBM) techniques, are compared to velocity measurements acquired for 3 test scenarios at 3 locations in a pilot scale vessel at the US DOE National Energy Technology Laboratory (NETL). The LES and RANS simulations are performed in ANSYS Fluent, and the LBM simulations in M-STAR.

The LES model well predicts the experimental data provided that the operational pressure profile within the individual pulse tubes is considered. While the RANS model failed to predict

the data and exhibited significant differences from LES with respect to turbulence quantities, it is a useful comparison tool that can quickly predict averaged flow parameters. The LBM model's rigid grid system is deemed unsuitable, as currently configured, for the NETL PJM vessel's wide range of length scales and curved boundaries, resulting in the longest simulation time and least accurate velocity predictions. Predicted velocity and turbulence metrics are explored to better understand the strengths and failures of the three models.

Because the LES model produced the most accurate predictions, it is exploited to generate animations and still images on various 2D planes that depict extremely complex flow patterns throughout the vessel with numerous local jets and mixing layer vortices The study concludes with recommendations for future research to improve the model development and validation strategy.

CFD Investigation of A Pulse Jet Mixed Vessel with RANS, LES, and LBM Simulation Models

By

Jung W. Kim

Dissertation submitted to the Faculty of the Graduate School of the
University of Maryland, College Park, in partial fulfillment
of the requirements for the degree of
Doctor of Philosophy
2023

Advisory Committee:

Professor Richard Calabrese, Chair
Professor Jeffery Klauda
Professor Johan Larsson
Professor Chen Zhang
Professor Cecilia Huertas

Acknowledgements

I express my gratitude to my advisor, Dr. Richard Calabrese, and the members of my dissertation committee. I sincerely appreciate everyone's mentorship, guidance, and patience throughout this project. I am truly thankful for the opportunities made available by the HSMRP and other research groups at the University of Maryland. I will never forget the academic and life lessons I gained while participating in the program.

I would like to thank Dr. Chris Guenther and the National Energy Technology Laboratory (NETL) for providing the CAD files containing the geometry of the laboratory scale PJM vessel as well as the vertical velocity data collected through a series of laboratory experiments. NETL also partially funded the study through the Oak Ridge Institute for Science and Education (ORISE) program, which greatly aided the research.

I sincerely appreciate ANSYS and Dr. John Thomas for providing me with academic licenses for FLUENT and M-STAR. The CFD codes provided the foundation for the study's simulation models.

I would also like to thank UMD's HPCC Allocations and Advisory Committee for allowing me to use the University's High-Performance Computing (HPC) clusters. It would not have been possible to run the LES and LBM simulations without the computation time on Deep Thought II and MARCC. "I acknowledge the University of Maryland supercomputing resources (http://www.it.umd.edu/hpcc) made available for conducting the research reported in this paper."

Table of Contents

List of Tables

List of Figures

List of Abbreviations and Nomenclature

Abbreviations	
CFD	Computation Fluid Dynamics
CPM	Continuous Pulsing Mode
DNS	Direct Numerical Simulation
DOE	The US Department of Energy
HLW	High Level Waste
IGL	Ideal Gas Law
IPP	Individual Pressure Profile
LAW	Low Activity Waste
LBM	Lattice Boltzmann Method
LES	Large Eddy Simulation
PJM	Pulse Jet Mixer
RANS	Reynolds Averaged Navier-Stokes equations
TDR (ε)	Turbulence Dissipation Rate
TKE (k)	Turbulent kinetic energy
UPP	Uniform Pressure Profile
VOF	Volume Of Fluid
WALE	Wall-Adapting Local Eddy-Viscosity
WTP	Waste Treatment and Immobilization Plant
NETL	National Energy Technology Laboratory

Nomenclatures	
ρ	Density
$\boldsymbol{u}$	Velocity
t	Time
σ	Stress tensor
f_b	Body force
τ	Viscous stress tensor
$\bar{P}$	Pressure
μ	Viscosity
g	Gravitational acceleration
τ_t	Reynolds stress
k	Turbulent kinetic energy
ϵ	Turbulence dissipation rate
P_k, P_ε	Production terms for k and ϵ
τ_{sgs}	SGS stress
μ_{sgs}	SGS viscosity
α	Volume fraction
f	Boltzmann particle distribution function
Δt	Time-step size
t_r	Relaxation time
$t*$	Confidence interval critical value

1. Introduction

1.1. Motivation

For more than 40 years, the nuclear reactors at the US Depart of Energy's Hanford site produced plutonium for America's defense program. The reactors and downstream separation processes were widely used during the Second World War and Cold War, despite the fact that the process was inefficient and unsustainable. As a result, the Hanford Nuclear Reservation in southeastern Washington State now has 177 underground storage tanks holding 56 million gallons of "nuclear waste". Processing the material is difficult but necessary because the underground tanks are nearing the end of their expected life, and leaks exceeding one million gallons have been identified [1].

Research indicates that leaked radioactive contaminants may have serious impacts on the surrounding soil, groundwater, and the Columbia River [2]. While projects to mitigate the damage, such as underground physical barriers and chemical deactivation of contaminants, are underway, a permanent solution that prevents any further influx of waste material into the environment is of greater importance. As a result, developing a method to safely process and transport the materials in the 177 waste vessels for long-term storage in a timely manner is critical.

The US Department of Energy (DOE) plans to use the vitrification process to achieve the goal. The technology entails combining the waste with glass-forming materials and heating them to temperatures above 2,000 °F. The molten mixture is then poured into steel containers to cool and solidify. In the final glass form, the waste is stable and environmentally resistant to safely dissipate its radioactivity over hundreds to thousands of years.

The process will be implemented at the Hanford site in three primary facilities that are depicted in Figure 1: pretreatment (PT), low activity waste (LAW) vitrification, and high level waste (HLW) vitrification [3].

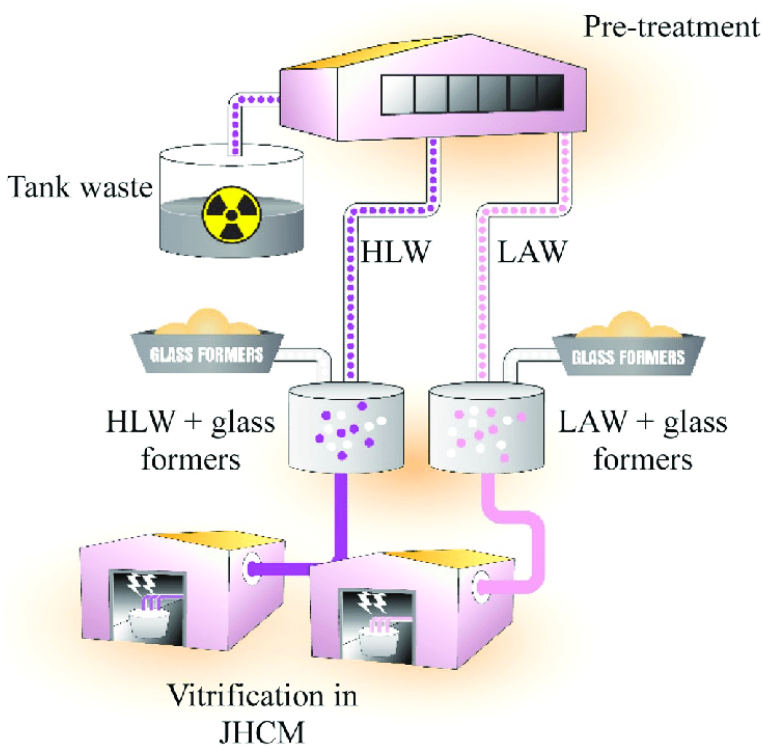

Figure 1. Vitrification Processes at Pre-treatment, HLW, and LAW Plants. Image excerpted from [5].

The primary function of the pretreatment facility is to accept the waste transported by pipe from the underground tanks and separate the stream into two variants. The majority of the solids and radionuclides are filtered and sent to the HLW plant, while the remaining much larger volume of low-activity solution is sent to the LAW facility. The LAW solution contains either spent ion-exchange resin in liquid form or process recycle streams with low concentrations of solids — typically less than 5% by weight. The high activity solutions are highly loaded with solids and exhibit non-Newtonian behavior. However, the low activity dilute solids solutions are expected to be Newtonian [4]. All three plants, PT, HLW and LAW contain both dilute and concentrated solids streams. DOE initially planned to treat HLW and LAW concurrently, but later decided that a sequential approach would be more practical. The current plan is to bypass PT and treat LAW first, followed by HLW about a decade later [3]. An important step in all 3 plants, but particularly the LAW plant operation is to keep the Newtonian fluid solutions homogeneous and well mixed to prevent any accumulations of the radioactive materials.

To minimize the radiation risk, the process vessels will be completely encapsulated behind thick reinforced concrete walls. Figure 2 illustrates the construction of the walls. This area, known as the "black cell," will be sealed and inaccessible to workers for the duration of the plant's operational life (~40 years), severely limiting vessel maintenance capabilities. As a result, PJM (Pulse Jet Mixer) technology was chosen due to the device's complete lack of moving parts in the vessel and a track record of dependable operation [4].

Figure 2. "Black Cell" Construction with a 38-ft-diameter Vessel with 16 PJM's. Image excerpted from [8].

As discussed in the next Section, the device's mixing performance is determined by geometry and a variety of physical dimensions and operational settings, and the full-scale models of the vessel can be as large as 38-ft in diameter. DOE estimated that the costs of testing full-scale vessel designs would be prohibitively expensive, with project timelines of years. As a result, in the hope that the strategy would significantly reduce project costs and duration, the DOE commissioned smaller-scale tests supported by CFD (Computational Fluid Dynamics) simulations. A 1-m-diameter scale model, for example, was built at DOE's National Energy Technology Laboratory (NETL) in Morgantown, West Virginia. The test program is an excellent candidate for supplementation with CFD simulations. CFD can offer rapid evaluation of design options and details on key flow phenomena that testing alone cannot provide. Experimental measurements are taken during the development phase to validate the CFD models. Subsequently, the validated simulation models produce numerical data that can be used to improve the laboratory and plant by identifying and testing potential equipment or operational issues.

1.2. Pulse Jet Mixer (PJM) Mixed Vessel

Pulse Jet Mixers (PJM's) were first developed in the 1970s for use in nuclear reprocessing plants at Sellafield in the United Kingdom. An extensive research and development program was put in place, with a focus on mixing and processing highly radioactive solutions. The effort resulted in the installation of over 200 vessels on the site during the 1980s. Since then, they have been steadily gaining acceptance for radioactive and hazardous chemical processing plants operations [6].

The basic components of the mixing technology are depicted in Figure 3, which shows a PJM and a Jet Pump Pair (JPP), a two-directional air pump that controls and modulates the mixer's operations.

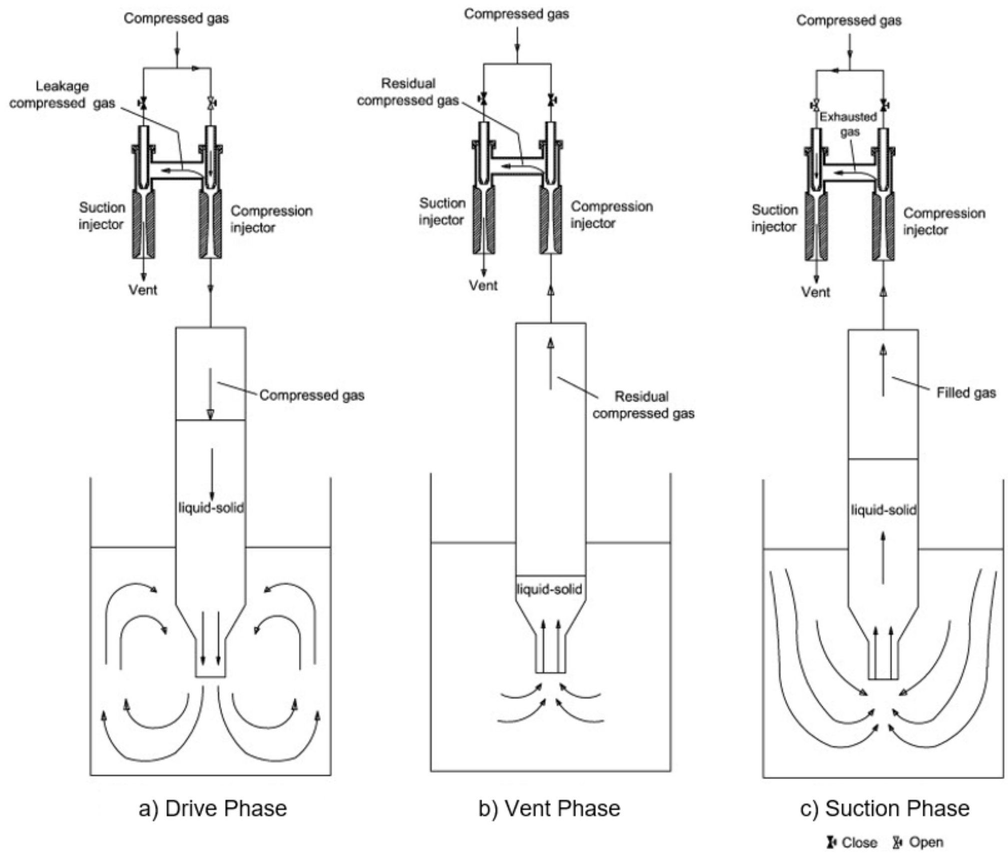

Figure 3. Jet Pump Pair (JPP) and Pulse Jet Mixer (PJM) in Three Operation Modes – a) Drive, b) Vent, and c) Suction Phases (images excerpted from [8]). Compressed air pushed working liquid out of the PJM during drive phases, propelling the nozzle jet. Compressed air is vented to the atmosphere during vent phases. During the suction phase, the internal pressure drops below the hydrostatic pressure at the nozzle, allowing working liquid to return to the PJM.

A typical PJM operation involves three phases – drive, vent, and suction. During a drive phase, the JPP injects compressed air from outside the black cell into the PJM body, pushing the working liquid out through the PJM's nozzle. During this phase, the PJM expels a fluid jet through its nozzle into its containing vessel to create fluid flows and drive scalar mixing and particle suspension. A venting phase then follows, during which the JPP opens its valves to the atmosphere, quickly depressurizing the PJM fluid. A suction phase begins as the JPP applies a partial vacuum to the PJM and the working liquid is drawn back into the PJM body through the nozzle. The PJM fluid level slowly rises back to the initial height, and the cycle is completed. Since a primary PJM objective is to prevent particle settling and promote resuspension, the discharge nozzle is located close to the vessel bottom. The process is repeated until the mixing and suspension requirements are satisfied. Figure 4 depicts a PJM pressure profile for a twelve-second cycle. While larger scale models typically have longer cycles, this is the typical duration for the NETL laboratory scale model.

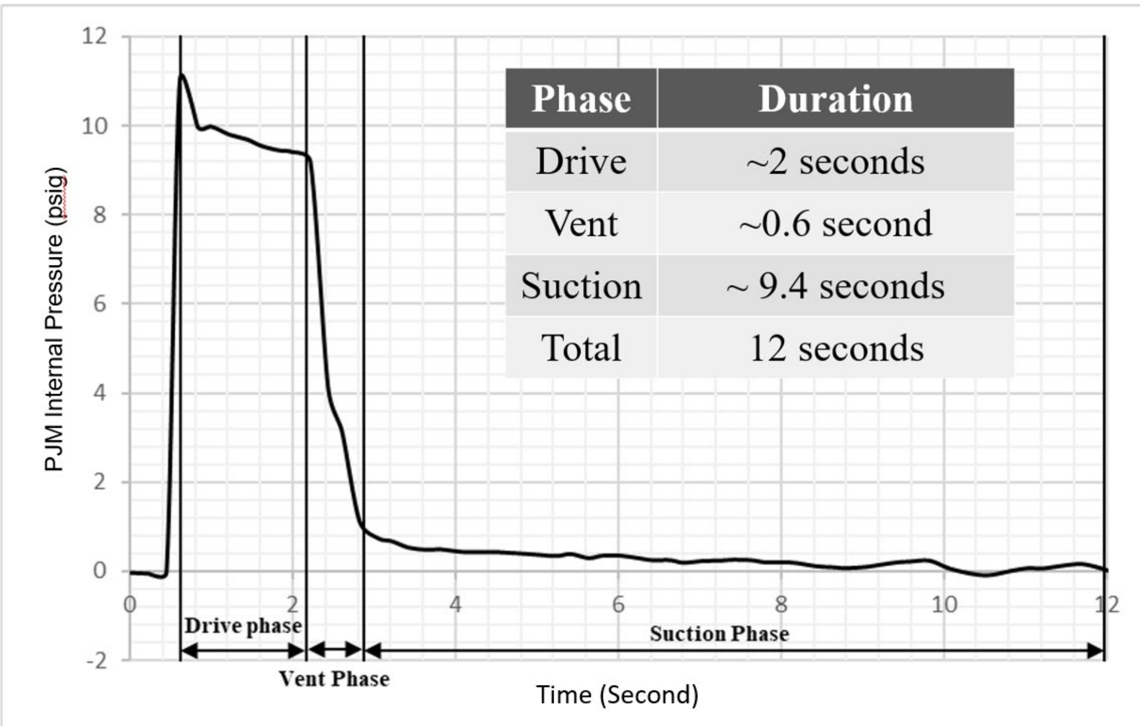

Figure 4.PJM internal pressure data provided by NETL during a mixing cycle. During the 1.6 seconds drive phase, internal pressure is high. The pressure rapidly drops during the vent phase and remains low during the suction phase, which lasts approximately 9.4 seconds.

Depending on the mixing requirements, multiple PJMs are frequently placed in a vessel in various configurations. The PJM scale has a limit beyond which its efficiency decreases [1]. As a result, when scaling up a PJM mixed vessel, it is preferable to increase the number of PJMs rather than their size. For instance, Figure 5 shows a 3-ft diameter scale vessel with four PJMs on the left and a 4-ft diameter scale with six PJMs on the right.

Figure 5. 1-m Diameter (left) which contains 4 PJMs and 1.2-m Diameter (right) which contains 6 PJMs (images excerpted from [7]).

The vessel's bottom is typically dish-shaped to allow gravity to draw the particles towards the center. To effectively lift the particles, the PJM nozzles face the dish bottom in close proximity and create strong impingement and floor-jet structures. The flows then congregate toward the vessel's center, forming an upward moving “central upwash plume”, which is depicted with a green arrow in Figure 6.

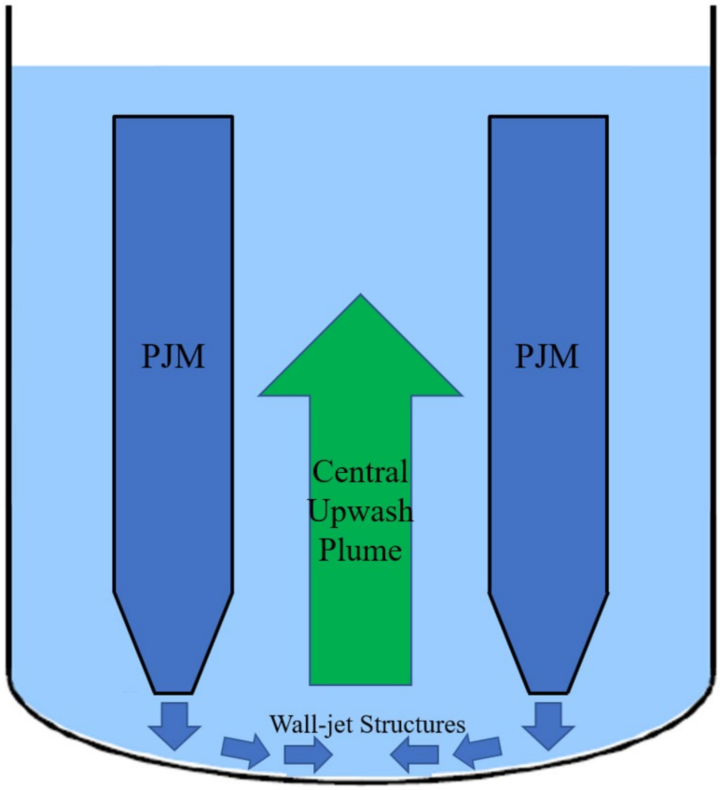

Figure 6. PJM nozzle jet flows converging towards the center to form a central upwash plume.

Test results reveal a close relationship between the plume's vertical velocity and complete clearance of particle accumulations from the vessel bottom [7]. Guenther et al. [8] showed that, for dilute suspensions, the mixture can be treated as a single fluid with increased viscosity. The studies also addressed validation of the single liquid assumption, which established single fluid experimental and simulation data to be valid for solutions lightly loaded with non-cohesive solid particles. As a result, while the simulations presented in this study use a single phase working fluid, the conclusions drawn can be extended to the particle clearance criteria required for LAW processing and dilute suspensions more generally [4], [9].

1.3. National Energy Technology Laboratory (NETL) PJM Vessel

As previously mentioned, NETL developed a 1-m diameter pulse jet mixed (PJM) vessel for the laboratory experiments. This is a scaled-down version of the full-scale PJM vessel development program, which will contain vessels up to 4-m in diameter. The main goal of the quarter-scale exercise is to characterize the device's mixing performance and identify an optimal operation scenario, as well as to develop and validate CFD models. The outcomes of the project will be incorporated into the design and construction of the full-scale model. The key dimensions of the NETL laboratory scale PJM vessel are described in Figure 7. The PJM's are vertically oriented with their nozzles pointing vertically towards the curved dish bottom. The vertical clearance between each nozzle and the bottom is 0.037 m.

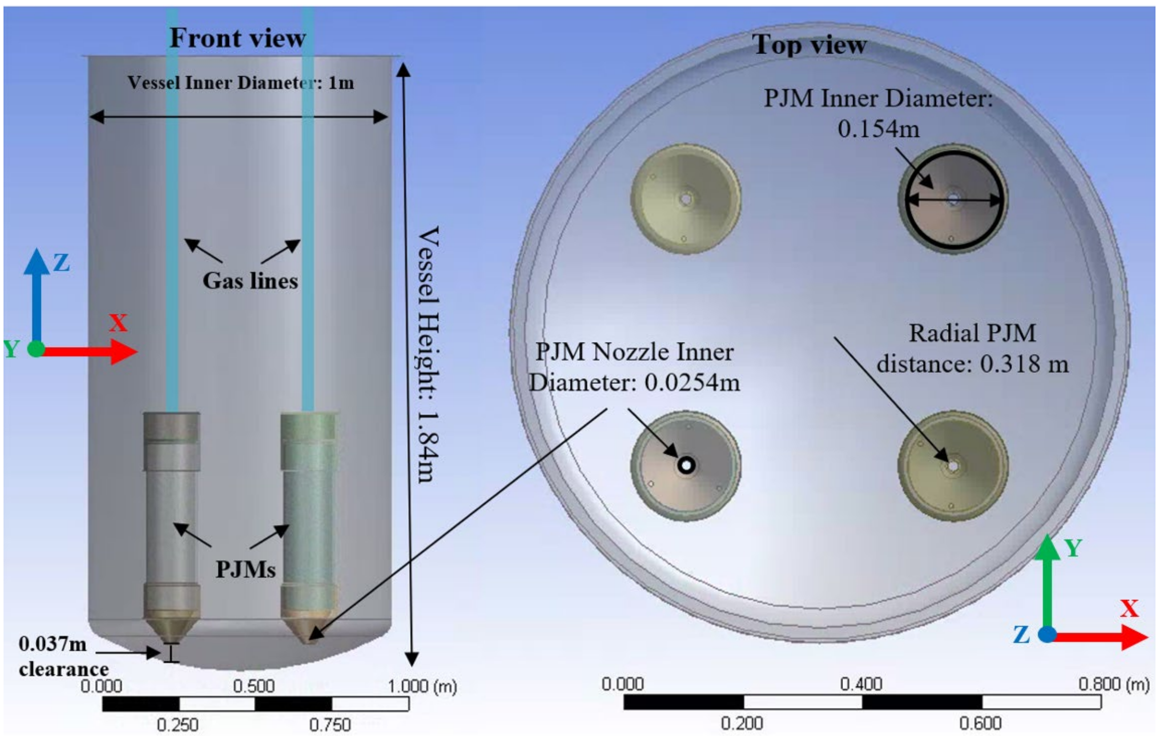

Figure 7. Side (left) and top (right) views of NETL laboratory scale PJM vessel. The 1.84-m tall and 1-m wide vessel contains four 0.154-m wide PJMs that are pointing towards the vessel's dish bottom with their nozzles.

The 1.84 m tall vessel contains 4 PJM's that operate in unison. While the PJMs are linked to a single JPP via gas lines to reduce synchronization delays, the length and pathway of each gas line varies significantly, resulting in differences in the internal pressure delivered to each PJM. The possibility of asymmetric jet flows originating from the PJMs rendered the use of symmetric planes inappropriate, despite the fact that the two planes divide the vessel into four identical quadrants. Section 3.2 will provide greater detail on the subject.

1.4. Project Objectives

The goal of this study is to develop several CFD models for the 1-m diameter NETL laboratory-scale PJM vessel and assess the simulation performance and potential applications of each. Three simulation techniques are developed and compared to identify an efficient and effective CFD strategy for the PJM device design. In the first part of the study, the performance of each model is validated against NETL's experimental data. Experiment and model limitations are discussed. In the following Sections, the simulation results are exploited and utilized to visualize flow fields and output turbulence metrics. The data are analyzed to gain a fundamental understanding of each model's strengths and weaknesses before making final recommendations on how to use the models and experiments in the program's research and development process.

1.5. Organization of Dissertation

The dissertation is divided into seven chapters. Chapter 1 provides the motivation, objectives, and outline of the study. It also introduces the NETL 1-m diameter laboratory-scale PJM vessel. The physical dimensions, pulse jet tube arrangements, and key physical and operating characteristics of the device are provided with figures.

The models employed and the key simulation model settings for the study are described in Chapter 2. Three simulation techniques are compared in this study. The first two are implemented in Ansys Fluent, a commercial CFD software package based on the finite volume method. The two models differ in the simulation techniques they use: one is based on the Reynolds Averaged Navier-Stokes equations (RANS) and the other uses Large Eddy Simulation

(LES) techniques. The third model employs M-STAR, a commercial CFD code based on the Lattice Boltzmann Method (LBM), in a manner analogous to LES.

In chapter 3, the NETL experiments and resulting data are described. NETL placed three electromagnetic (EM) velocity probes at different heights in the central upwash region of the vessel. The probe locations and measurement methods are described – the details that are employed in the simulation models for the validation process. The chapter also discusses a pressure synchronization issue discovered by analyzing individual PJM internal pressure profiles, as well as its potential impact on mixing and the developed velocity fields.

The development and refinement processes for the CFD simulations are discussed in Chapter 4. Details of several preliminary studies are provided, demonstrating the validity of the key assumptions regarding gas phase compressibility and liquid phase viscosity range. The mesh independence study for each modeling technique is described, and the final grid is justified. The statistical analysis methods for each model comparison are also provided and discussed.

Chapter 5 demonstrates the performance of each CFD model by comparing its central upwash plume (shown in Figure 6) vertical velocity predictions to the NETL experimental measurements. To emphasize the importance of applying the PJM's internal pressure accurately, the results are divided into two sections: the first for simulations that apply uniform (average) internal pressure to all PJMs, and the second for simulations that reflect individual PJM internal pressure settings.

The simulation models, tested and validated with the EM probe velocity data, are used in Chapter 6 to generate various velocity fields and turbulence metrics. The Section first describes how the internal pressure synchronization issue affects the central plume structure and general flow fields, and then proceeds to compare analyze predictions from the three CFD models to provide a fundamental understanding of the differences in their results and their accuracy levels. The analysis includes a series of velocity and turbulence data presented on 2D planes in still images and animations (contained in a PowerPoint file that accompanies this manuscript).

Based on the main findings, Chapter 7 discusses methods for best utilizing the simulation models in the research and development process of PJM mixed vessels. The chapter concludes with a summary and suggestions for future research.

The Appendix contains a collection of charts and plots created for this study but not discussed in the main Chapters.

2. Computational Fluid Dynamics (CFD) Simulations

With the aid of computer technology, the science of computational fluid dynamics (CFD) generates quantitative forecasts of fluid flow phenomena based on the governing conservation laws. Fluid mechanics, applied mathematics, and engineering all intersect in the area of CFD. Because its processes rely heavily on CPU and memory, its evolution has been closely linked to that of computer technology. With the advent of High Performance Computers (HPC), better solutions and applications for CFD are becoming available on a daily basis.

CFD has become a key approach in a variety of engineering fields of study. It provides useful information on the fundamental transport phenomena that would otherwise be prohibitively expensive or impossible to obtain. Ongoing research produces CFD solutions that improve the accuracy and speed of complex simulation scenarios like highly turbulent flows.

Three simulation techniques are developed and compared in this study in order to identify an efficient and effective CFD strategy for the NETL laboratory scale PJM vessel. Two commercial CFD codes are used: Ansys Fluent and M-Star.

2.1. Fundamental Equations

The Section lists fundamental equations of fluid mechanics, including conservation of mass and linear momentum. On a macroscopic scale, where typical lengths are much greater than inter-atomic distances, matter's discrete structure can be ignored, and materials can be modeled as continua. Fundamental laws that express conservation principles are used to derive the mathematical models that describe the physics of continua.

The study of the behavior of continua in response to mechanical forces is known as continuum mechanics. The continuity equation expresses the balance of mass through a control volume:

$$\frac{\partial \rho}{\partial t} + \boldsymbol{\nabla} \cdot (\rho \boldsymbol{u}) = 0 \tag{1}$$

where ρ is the density, and $\boldsymbol{u}$ is the velocity along the continuum.

The relationships between density and thermodynamic variables such as pressure and temperature are described by equations of state (EOS). The simulations in this study are based on the constant density model. During the PJM operations, there is no discernible temperature variation in the liquid, and the choice of EOS models in the air phase was tested to be negligible (Section 4.1.1).

The resultant force acting on the continuum is equal to the time rate of change of linear momentum:

$$\rho \left(\frac{\partial \boldsymbol{u}}{\partial t} + \boldsymbol{u} \cdot (\boldsymbol{\nabla} \boldsymbol{u}) \right) = \boldsymbol{\nabla} \cdot \boldsymbol{\sigma} + f_b \tag{2}$$

where, f_b is the resultant of the body forces (such as gravity and centrifugal forces) per unit volume acting on the continuum, and σ is the stress tensor. For a fluid, the stress tensor is often written as sum of normal stresses and shear stresses, $\sigma = -\bar{P}I + \tau$, where $\bar{P}$ is the pressure and τ is the viscous stress tensor.

As previously mentioned in Section 1.2, the study treats the lightly loaded solutions as a single Newtonian fluid [8]. Therefore, the viscous stress tensor can be expressed as follows:

$$\boldsymbol{\tau} = \mu \left(\boldsymbol{\nabla} \boldsymbol{u} + (\boldsymbol{\nabla} \boldsymbol{u})^T \right) \tag{3}$$

2.2. Simulation Models

The majority of continuum fluid flows of engineering interest are turbulent, having irregularly fluctuating flow quantities. These fluctuations are frequently at such small scales and high frequencies that resolving them in space and time incurs exorbitant computational costs. It is therefore often opted to solve for averaged or filtered quantities and approximate the impact of small fluctuating structures rather than solving for the exact governing equations of turbulent flows (i.e., utilizing Direct Numerical Simulation). CFD simulation models offer a variety of approaches for modeling these turbulence structures.

During the drive phase of the NETL PJM vessel, the Reynolds number varies from a few thousands to hundreds of thousands in different regions (Table 1). As such, turbulence modeling is a critical part of the simulation configurations.

Table 1. Reynolds Number Variation in the NETL PJM Vessel

	Length Scale (m)	Characteristic Velocity (m/s)	Reynolds Number, Re
PJM Body	0.154	0.252	38,700
Nozzle	0.0254	8.52	218,000
Vessel Core Area*	0.410	0.0198	8,106

**A central region with a diameter of 0.41 m that captures the upward plume velocity. Depicted in Figure 28.*

While all existing simulation models for turbulence are approximations of physical turbulence phenomena, the degree of approximation in a given model depends on the nature of the modeled flow. As a result, the model must be carefully chosen based on the nature of the application. In this study, simulations based on the Reynolds Averaged Navier-Stokes equations (RANS) and the Large Eddy Simulation (LES) method are performed in a commercial CFD code, Ansys Fluent.

The Reynolds Averaged Navier-Stokes equations (RANS) utilize empirical models to simulate turbulence quantities and mean velocity fields. As a result, the impact of turbulence is not resolved, and eddy structures are not captured in the velocity field results. While RANS offers a significant advantage in computational efficiency, studies indicate its limitations in simulating flows with strong pressure gradient and vorticity, resulting in inaccurate energy dissipation rate and flow velocity predictions [10], [11], [12].

Due to the shortcomings of RANS, Large Eddy Simulation (LES) is often opted for instead. LES attempts to fill the gap between RANS and resource intensive method such as Direct Numerical Simulation (DNS). LES utilizes a filtering equation to resolve large eddies and relies on subgrid-scale empirical model to limit the computational burden.

The Lattice Boltzmann method (LBM), like LES, is capable of resolving turbulent structures larger than the grid scale. The method employs a simplified algorithm that includes collision and streaming steps. The method's primary differences compared to LES and RANS include a meshless preprocessing environment and highly scalable numerical schemes. While these factors can lead to significantly faster turnaround times for some applications, simulations involving delicate geometries and highly temporal flow phenomena can result in inefficient computation resource management and inaccurate results. Due to the fact that the method has not been widely used for PJM devices, its performance on the laboratory scale vessel must be closely monitored and analyzed.

2.2.1. RANS (Reynolds Averaged Navier-Stokes equations)

RANS equations are derived by time-averaging decomposed pressure and velocity expressions. In a process called Reynolds decomposition, the flow and pressure variables in the Navier-Stokes equations are first separated into the time-averaged and fluctuating components. The following equation depicts the splitting of a velocity term in this manner:

$$u_i = \overline{u_i} + u_i' \tag{4}$$

where $\overline{u_i}$ is the mean and u_i' is the fluctuating component of velocity u_i. After being decomposed, the equations are time averaged to output the RANS equations. The averaging process eliminates the fluctuating terms in expressions with linear terms. For example, after going through the process, the continuity equation takes the following form:

$$\frac{\partial \rho}{\partial t} + \frac{\partial}{\partial x_i} \rho \overline{u_i} = 0 \tag{5}$$

where $\overline{u_i}$ is averaged velocity and ρ is density. Except for the time averaged velocity term, this is the same as the original form.

When the same process is applied to the Navier-Stokes equations. The fluctuating components do not completely disappear due to the non-linear term:

$$\rho\left(\frac{\partial \overline{u_i}}{\partial t} + \frac{\partial}{\partial x_j}(\overline{u_i}\overline{u_j})\right) = -\frac{\partial \overline{P}}{\partial x_i} + \frac{\partial}{\partial x_j}\left[\mu\left(\frac{\partial \overline{u_i}}{\partial x_j} + \frac{\partial \overline{u_j}}{\partial x_i}\right)\right] - \frac{\partial}{\partial x_j}\rho\overline{u_i'u_j'} + \rho g \tag{6}$$

The non-linear term is called the Reynolds stress ($\tau_t = \rho\overline{u_i'u_j'}$). A closure model is required to approximate the term without resolving the turbulence phenomena. Realizable k-∈ model is used in this study because of its advanced capabilities in simulating high pressure gradients [13], which is required for the transition regions between the PJM's and the vessel. The realizable k-ε model estimates Reynolds stress as follows:

$$\tau_t = \rho\overline{u_i'u_j'} = -\mu_t\left(\frac{\partial \overline{u_j}}{\partial x_i} + \frac{\partial \overline{u_i}}{\partial x_j}\right), \qquad \mu_t = \rho f_\mu C\frac{k^2}{\varepsilon}. \tag{7}$$

where k is turbulent kinetic energy and ε is turbulence dissipation rate.

The model introduces transport equations for k and ε which are defined below:

$$\frac{\partial}{\partial t}(\rho k) + \frac{\partial(\rho k \bar{u_i})}{\partial x_i} = \frac{\partial}{\partial x_j}[(\mu + \frac{\mu_t}{\sigma_k})\frac{\partial k}{\partial x_j}] + P_k - \rho\varepsilon + S_k \tag{8}$$

$$\frac{\partial}{\partial t}(\rho\varepsilon) + \frac{\partial}{\partial x_i}(\rho\varepsilon\bar{u_i}) = \frac{\partial}{\partial x_j}[(\mu + \frac{\mu_t}{\sigma_\varepsilon})\frac{\partial\varepsilon}{\partial x_j}] + \frac{\varepsilon}{k}C_{\varepsilon 1}P_\varepsilon - C_{\varepsilon 2}f_2\rho(\frac{\varepsilon^2}{k}) + S_\varepsilon \tag{9}$$

where P_k and P_ε represent production terms for k and ε, respectively. They are defined as follows:

$$P_k = \mu_t|S|^2 \tag{10}$$

$$P_\varepsilon = f_c|S|k \tag{11}$$

where f_c is the curvature correction factor and $|S|$is the modulus of the mean strain rate tensor, which is defined as follows:

$$|S| = \sqrt{2S_{ij}S_{ij}}, \quad S_{ij} = \frac{\partial u_i}{\partial x_j} + \frac{\partial u_j}{\partial x_i} \tag{12}$$

2.2.2. Large Eddy Simulation (LES)

The LES models resolve the transient nature of the largest eddies and utilize closure functions to account for eddies smaller than the computation grid scales. Therefore, the numerical solution only accounts for the motions of eddies larger than the grid scale. Each solution variable ϕ is decomposed into a filtered value $\tilde{\phi}$ and sub-grid value ϕ'.

$$\phi = \tilde{\phi} + \phi' \tag{13}$$

Eddies whose scales are less than the filter width or grid spacing utilized in the computation are effectively removed throughout the filtering procedure. The omitted information from the filtered scales is accounted for by a subgrid-scale (SGS) closure model. The model arranges the filtered equations as the RANS model does the time averaged equations, with SGS stress term replacing the Reynolds stress term. The LES form of the continuity and Navier-Stokes equations are shown below, with τ_{sgs} representing the SGS stress term.

$$\frac{\partial \rho}{\partial t} + \frac{\partial \rho \widetilde{u_i}}{\partial x_i} = 0 \tag{14}$$

$$\rho\left(\frac{\partial \widetilde{u_i}}{\partial t} + \frac{\partial}{\partial x_j}(\widetilde{u_i}\widetilde{u_j})\right) = -\frac{\partial \overline{P}}{\partial x_i} + \frac{\partial}{\partial x_j}\left[\mu\left(\frac{\partial \widetilde{u_i}}{\partial x_j} + \frac{\partial \widetilde{u_j}}{\partial x_i}\right)\right] - \frac{\partial}{\partial x_j}\tau_{sgs} \tag{15}$$

In this study, the Wall-Adapting Local Eddy-Viscosity (WALE) SGS model is employed, which is an improved form of the popular Smagorinsky-Lilly model. It was chosen because it has been shown to perform better for wall-bounded flows and wall impingement structures due to its inherent ability to provide accurate scaling at walls [14], [15].

The model defines τ_{sgs} as follows:

$$\tau_{sgs} = 2\mu_{sgs}|S|, \qquad \mu_{sgs} = \rho l^2 S_w \tag{16}$$

where $|S| = \sqrt{2S_{ij}S_{ij}}$ is the modulus of the resolved strain rate tensor ($S_{ij} = \frac{1}{2}(\frac{\partial \tilde{u}_i}{\partial x_j} + \frac{\partial \tilde{u}_j}{\partial x_i})$), μ_{sgs} is the SGS viscosity, l is the grid length scale, and $S_w$is a deformation parameter, which is defined:

$$S_w = \frac{\mathrm{S}_d{:}\mathrm{S}_d{}^{3/2}}{\mathrm{S}_d{:}\mathrm{S}_d{}^{5/4} + \mathrm{S}{:}\mathrm{S}^{5/2}}, \qquad S_d = \frac{1}{2}\left(\frac{\partial \tilde{u}_k}{\partial x_i}\frac{\partial \tilde{u}_j}{\partial x_k} + \frac{\partial \tilde{u}_k}{\partial x_j}\frac{\partial \tilde{u}_i}{\partial x_k}\right) - \frac{1}{3}\delta_{ij}\frac{\partial \tilde{u}_k}{\partial x_l}\frac{\partial \tilde{u}_l}{\partial x_k} \tag{17}$$

From the modeled parameters, sub-grid scale turbulence kinetic energy (k) and turbulence dissipation rate (ϵ) are derived as follows:

$$k_{SGS} = 3.5\frac{\mu_{sgs}}{\rho}|S|, \qquad \epsilon_{SGS} = \frac{\mu_{sgs}}{\rho}|S|^2 \tag{18}$$

Because the filtered variables are resolved by the grid scale, their turbulence metrics are derived directly from the definitions. Turbulence kinetic energy (k) is characterized by measured root-mean-square (RMS) velocity fluctuations.

$$k_{Res} = \overline{(\tilde{u}_i')^2} + \overline{(\tilde{u}_j')^2} + \overline{(\tilde{u}_k')^2}, \qquad \epsilon_{Res} = \nu\frac{\partial u_i'}{\partial x_k}\frac{\partial u_i'}{\partial x_k} \tag{19}$$

where $\overline{u_i'} = \frac{1}{T}\int_0^T (\tilde{u}_i(t) - \bar{u})dt$. $\tilde{u}$, as defined above, is filtered velocity. T represents the sample size in this study. Turbulence production of the resolved scale (P_{Res}) depends on the RMS fluctuations as well as the averaged velocity ($\overline{u_i}$):

$$P_{Res} = \rho\overline{\widetilde{u_i}\widetilde{u_j}}\frac{\partial\overline{u_i}}{\partial x_j} \tag{20}$$

2.3. Multiphase Modeling of Gas-Liquid Interfaces

Multiphase flow numerical simulations require more complexity than single phase flow simulations due to the presence of an interface across which there is a jump in fluid-fluid properties and the exchange of mass and momentum between the phases. For modeling purposes, such flows can be classified as dispersed (bubbly flow, droplet flow), intermittent (slug flow, churn flow), and stratified based on increasing spatial scales of interface between the phases. Within the scope of this study, the interfaces between the gas and liquid phases are limited to the free surfaces within each PJM and at the top of the vessel. The interfaces are best described as stratified because they move slowly with wavy movements on the free surfaces. Other operation scenarios that would allow high pressure air to reach the PJM nozzle and introduce bubbles into the vessel would render the model inapplicable. In such a scenario, one of the dispersed multiphase models should be used.

Volume tracking and interface capturing methods like Volume of fluid (VOF) are well suited for simulating stratified multiphase flows with large scale interfaces. VOF is a popular model in which all phases share one set of momentum equations. Based on the shared momentum calculations, VOF tracks each component's volume fraction in every cell, which determines the cell's material properties.

The volume fraction (α_i) describes the phase distributions and the location of interfaces. For each cell in the simulation space, the Phase *i* volume fraction is defined as:

$$\alpha_i = \frac{V_i}{V} \tag{21}$$

where V_i is the volume of phase i in the cell and V is the cell volume. The presence of different phases or fluids in a cell can be distinguished based on the value of the volume fraction. For example, $\alpha_i = 0$ indicates that phase *i* is completely absent from the cell, while $\alpha_i = 1$ indicates that the phase completely fills it. Values between the two indicate the presence of a phase interface.

The material properties at each cell are determined by the phase components. For instance,

$$\rho = \sum_i \rho_i \alpha_i \tag{22}$$

where ρ is the density of the cell, and ρ_i is the density of phase *i*.

All phase volume fractions in a cell must add up to one:

$$\sum_{i=1}^{N} \alpha_i = 1 \tag{23}$$

where N represents the total number of phases.

The phase mass conservation equation shown below drives the distribution of each phase.

$$\frac{\partial}{\partial t}\left(\int_V \rho \, dV\right) + \int_A \rho u \cdot da = \int_V S dV \qquad (24)$$

where **a** is the surface area vector, **u** is the fluid velocity, S is the phase source term ($S = \sum_i S_{\alpha_i} \cdot \rho_i$, where S_{α_i} is a user-defined source term for each phase i).

2.4. Mesh

The mesh for the RANS and LES simulation models were developed in ANSYS Meshing. A challenging aspect of meshing the PJM vessel originates from its dynamic ranges of length and velocity scales. Tetrahedral and polyhedral methods were considered for their flexibility, and polyhedral was opted for its better stability modeling rotational flows. Mesh independence studies were performed on each simulation model to achieve accurate and efficient grid scales and cell counts. For example, the initial mesh is with minimal resolutions sufficient to capture the vessel's features in RANS. The mesh was then refined gradually, focusing on the nozzles, dish bottom, and core regions. The key metrics demonstrated convergence behavior at approximately 1.8 million cell counts. Section 4.1.1 provides greater detail about the procedure. The final result is displayed in Figure 8 on a vertical cross-sectional plane that includes two opposing PJM's. The plane cuts across the center of the vessel and two of the four PJM's. A highly dense mesh is used around the PJM nozzles and at the dish bottom to capture jet impingements and central plume formations. The mesh density is reduced gradually in the mid and top regions as the velocity gradients are lower in this area.

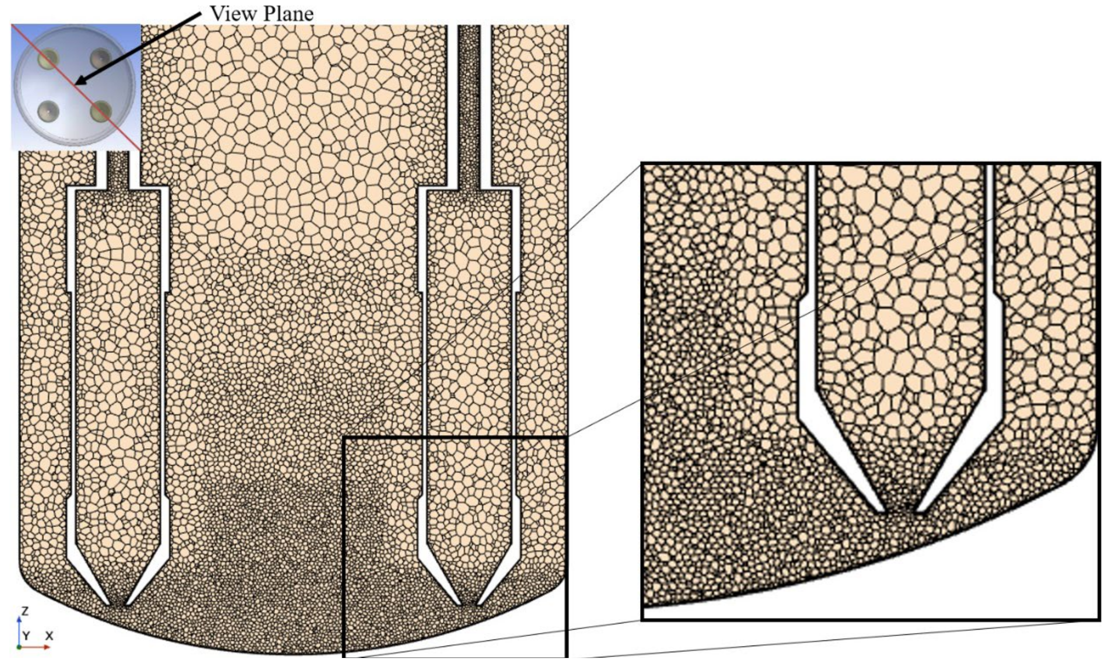

Figure 8. The final mesh for RANS simulation with 1.8 million cells. Regional mesh refinements are applied in the central and bottom regions to capture steep gradients.

A similar process is performed on the LES model (Section 4.2.2). Figure 9 shows the final results with 12 million cells. LES requires significantly smaller cell sizes than RANS as they determine the resolution of captured eddies.

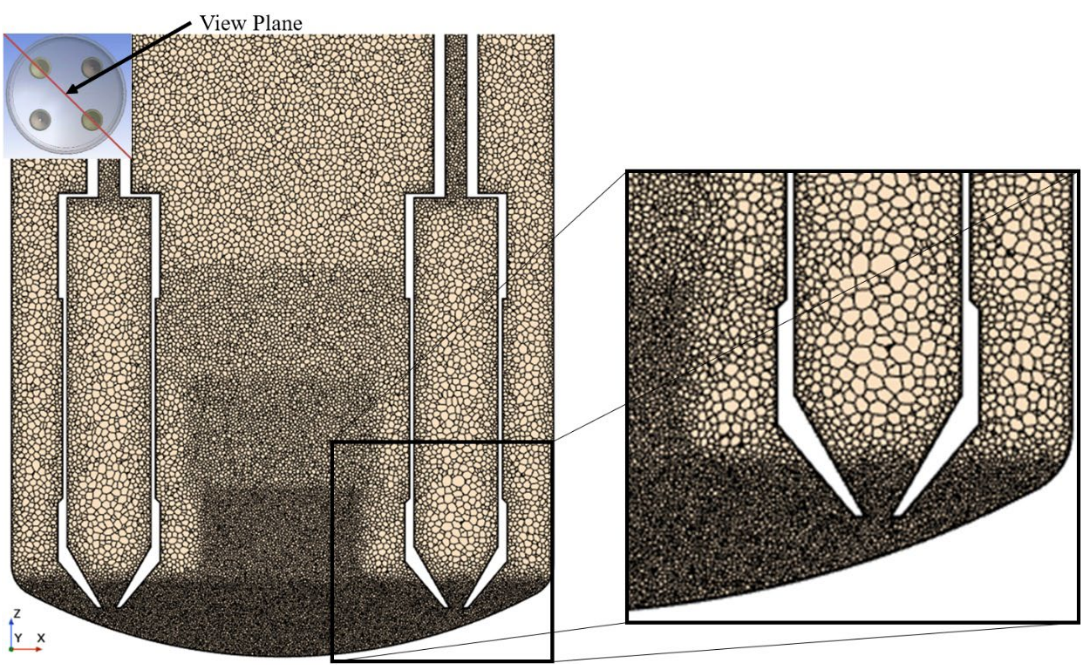

Figure 9. The final mesh for LES simulation with 12 million cells. Compared to the RANS mesh, the resolution in the core plume and bottom regions are significantly more refined.

2.5. Lattice Boltzmann Method (LBM)

M-Star CFD, a commercial code, was used in this study for Lattice Boltzmann Method (LBM) simulations. The LBM has recently gained popularity in CFD communities for its short turnaround time and ability to account for physicochemical phenomena. As currently available commercial solvers rely mostly on homogeneous grid structures without surface mesh, there are significantly less configuration steps and the solvers scale up almost linearly in High Performance Computing (HPC) environments.

The simpler implementation, however, may also limit the method's adjustability and hinder its efficiency, stability, or accuracy for simulations with complex boundaries or flows. For instance, studies reported poor performance of LBM simulating flows with strong velocity gradients, wide length and velocity scales, or highly curved boundaries [16], [17], [18]. In other examples without those challenging elements, LBM showed promising results [19], [20], [21].

Simulating PJM vessel flows will be a meaningful test for LBM, considering that the system offers all the aforementioned challenges. PJM flows experience dramatic changes in length and velocity scales when the fluid exits the PJM's through the nozzles into the vessel. Modeling curved boundaries is crucial since the vessel bottom that PJM jets impinge upon is curved to direct the impingement flows to the center of the vessel. If LBM successfully models the flows, it may be considered a meaningful alternative to LES which can be cost-prohibitive in many industrial applications.

In LBM, the physical space occupied by fluids is discretized into a homogeneous grid known as the lattice. Within the structure, the method solves the Boltzmann or transport equations of molecular probability distribution functions that define the density and velocity at each node. The molecular velocities are discretized into a finite number of velocity vectors. Figure 3 depicts an example of D2Q9 scheme, in which velocity vectors are discretized into 9 directions in a 2D space. A set of particles that represent fluid molecules carry one of the nine vectors (e0, e1, e2,..., e8). The motion, taken as a whole, describe the macroscopic flow of fluids within the volume. In a 3D simulation, a D3Q19 scheme is commonly used, which is the option offered in M-Star, the commercial solver employed in this study.

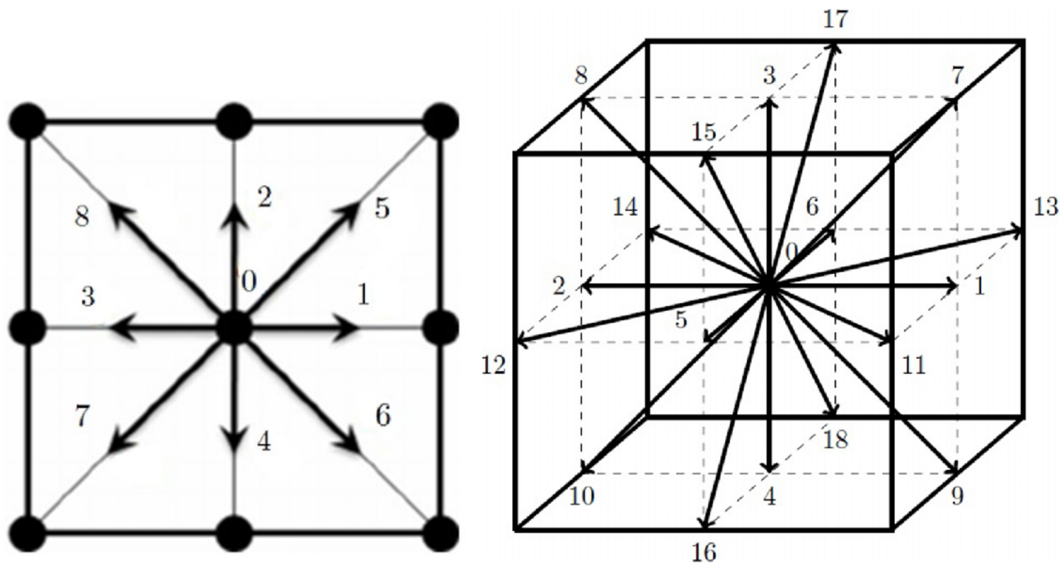

Figure 10. The Lattice Boltzmann Method D2Q9 (left) and D3Q19 (right) velocity vector discretization schemes describe allowed directional paths for particles.

The Boltzmann equation, in contrast to traditional top-down numerical approaches such as the Navier Stokes equations, can be described as bottom-up. It depicts the collective actions of molecules via probability distribution functions, which are manifested through streaming and collision steps. The Boltzmann equation below describes the particle distribution function (f_i).

$$\frac{\partial f_i}{\partial t} + e_i \frac{\partial f}{\partial e_i} = -\frac{1}{t_r}(f - f^0) \tag{25}$$

$$f_i(x + Ce_i \Delta t, t + \Delta t) - f_i(x,t) = -\frac{\left[f_i(x,t) - f_i^{eq}(x,t)\right]}{t_r} \tag{26}$$

$f_i^{eq}(\vec{x},t)$ is the equilibrium distribution, t_r is the relaxation time-scale, Δt is the time-step, and e_i is the non-dimensional velocity at the lattice point. The LHS of eq. (30) describes the streaming step, during which particles are allowed to move from one lattice node to another along the prescribed directions. The streaming step is graphically represented in the figure below.

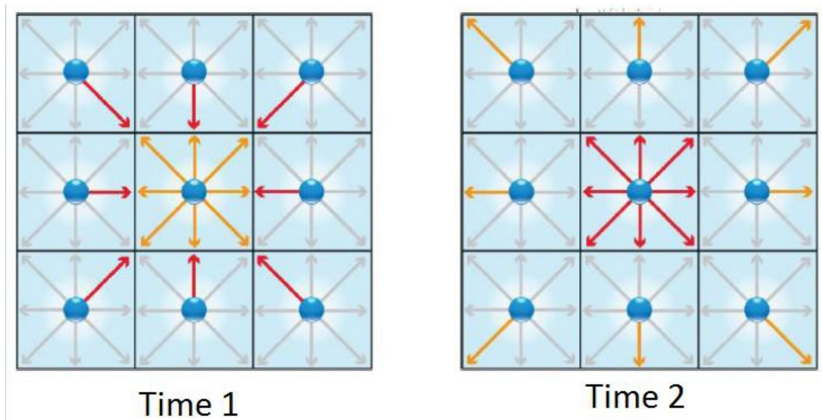

Figure 11. Illustration of the streaming step. Red and orange arrows indicate how fluid movements progress through the time step process.

The RHS of eq. (30) describes the collision step. The equilibrium distribution is calculated based on the particle distribution and velocity at the lattice node, and t_r is the relaxation time towards equilibrium. Eq. (27) shows t_r, which is related to the kinematic viscosity of the fluid.

$$t_r = \frac{2t_r - 1}{6} \tag{27}$$

Finally, the collective properties of the particle distribution define the macroscopic properties such as density and momentum, as described in equations 28 and 29, respectively.

$$\rho(\vec{x}, t) = \sum_{i=0}^{a} f_i(\vec{x}, t) \tag{28}$$

$$\rho u(\vec{x}, t) = \sum_{i=0}^{a} \vec{e_i} f_i(\vec{x}, t) \tag{29}$$

3. NETL Experimental Measurements

The geometry and dimensions of the NETL PJM test vessel are given in Section 1.3. In the NETL experiments, velocity probes were placed at three locations as shown in Figure 12. Measurements of the vertical velocity components were made over 80 PJM discharge cycles for each of the operation scenarios listed in Table 2. The probes are named after their relative positions: bottom, middle, and top. Drive pressure is the maximum air pressure inside PJM tubes during a drive phase and drive time is the duration for which the drive pressure is maintained. Vessel liquid fill height indicates the location of the free surface when the PJM operation begins.

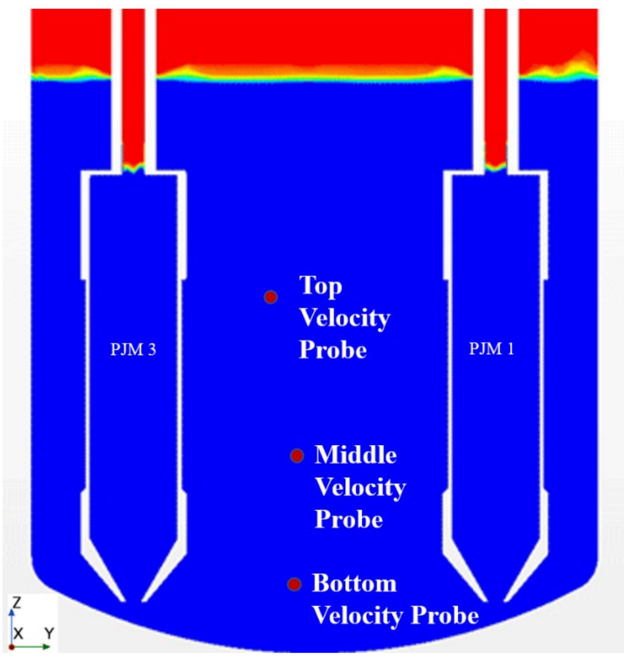

Probe location	r (cm)	θ (deg)	z (m)
Top	4.1	7.5	0.62
Middle	2.6	-14	0.35
Bottom	3.5	-15	0.19

Figure 12. Illustration of velocity probe locations. They are located off-center at varying height levels at z = 0.19, 0.35, and 0.62 m to capture the upward plume's vertical velocity at bottom, middle, and top regions, respectively. The left figure illustrates the probes' locations on a vertical plane, and the right table lists the probe locations in cylindrical coordinates. θ = 0 refers to the angle between the center and the PJM 3.

Table 2. The Experiment Operation Conditions

Scenario No.	Drive Pressure (psig)	Vessel Liquid Fill Height (m)	Drive Time (s)	Total Cycle Time (s)
1	19.60	1.07	1.64	12
2	20.44	1.67	1.64	12
3	19.60	1.07	1.56	12

3.1. Statistical Analysis

The NETL vertical velocity data obtained with three EM probes were acquired at a sampling frequency of 10 Hz, producing 120 measurements for each PJM discharge cycle which is 12 seconds long. The raw data for100 cycles were provided to us, which were ensemble averaged to produce one representative cycle that comprises the mean value at each time point in the discharge cycle. The 95% confidence interval is also calculated at each point. The limits are described in the equation below:

$$\left(\bar{x} - t^* \frac{s}{\sqrt{n}}, \bar{x} + t^* \frac{s}{\sqrt{n}}\right) \tag{30}$$

where $\bar{x}$ is the sample mean, t^* is the critical value, s is the sample standard deviation, and n is the sample size. Student's t-distribution table [22] was utilized for the critical value (t^*= 1.984 for 95% confidence interval and degrees of freedom = 99).

When the averaged data for each point in a cycle are utilized to validate the simulation results, the confidence intervals will be provided alongside to indicate the variability of the dataset, and whether the differences in the mean or averaged values are statistically significant.

3.2. PJM Pressure Synchronization

Pressure readings from each of the four PJM tubes are included in the NETL experimental measurements. A pressure sensor was installed near the compression injector (shown in Figure 3). The pressure data measured during Scenario 1 of PJM operation is shown in Figure 13. The data reveals significant differences among the four PJM pressure levels. For example, the drive phase pressure differs by 30% between PJM 1 and PJM 3. Similar differences among the PJM's are observed in Scenario 2 and 3, and the figures are attached in the Appendix Section 8.1. Early simulation studies of the mixing vessel applied the average value (represented by the dashed line in Figure 13) to all four PJM's [4], effectively assuming axial symmetry in the vessel since the pressure differences do not significantly influence the character of the jets emanating from the PJM nozzles.

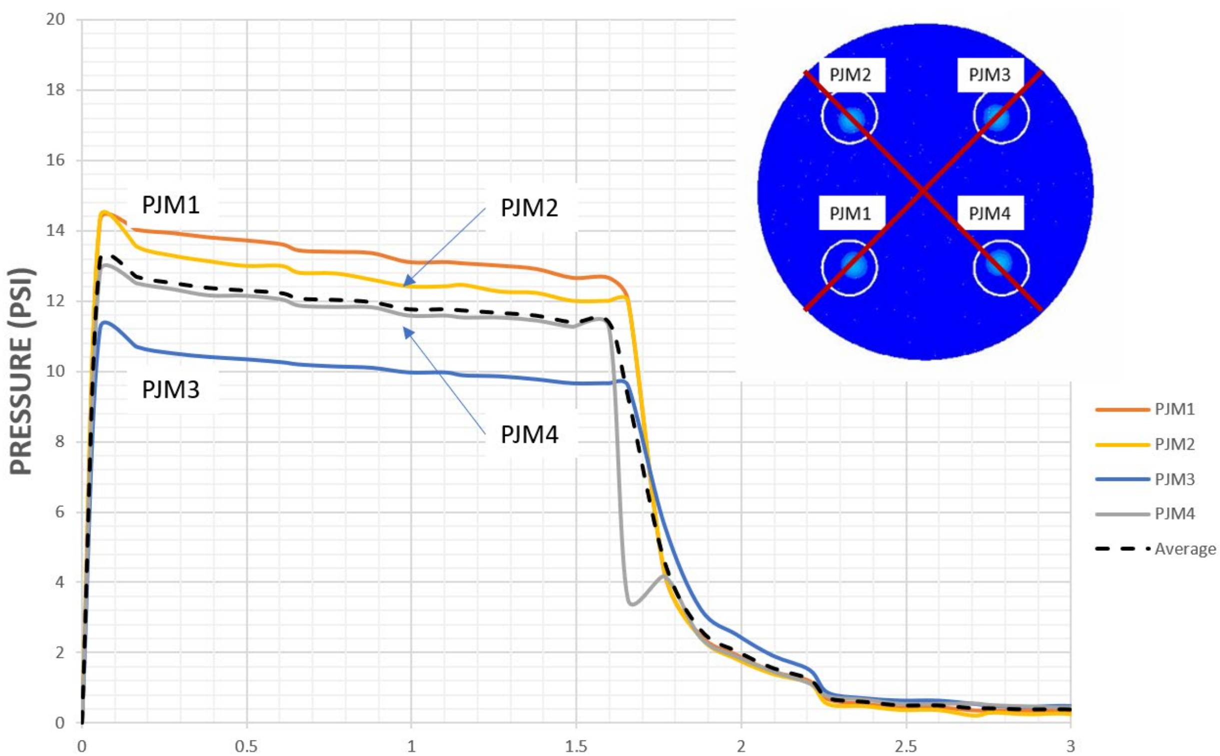

Figure 13. Internal air pressure for each PJM during Scenario 1 (Table 2) mixing operation. The internal drive pressures differ by up to 30% among the PJMs. The dashed line represents the

averaged value for the PJMs. The red lines on the top-right corner diagram represent the symmetry planes that cut the vessel into identical quarters.

To understand the impact of the imbalance, two pressure profile cases are considered. The Uniform Pressure Profile (UPP) case will follow this assumption and uses the average pressure for all PJM's. The Individual Pressure Profile (IPP) accurately reflects each PJM's measured pressure data. RANS, LES, and LBM models will be run utilizing the two profiles and the results are reported and compared in Sections 5.1 and 5.2. For the UPP, the jet emanating from each nozzle will be the same, so symmetry in the central upwash plume is expected. If differences in each jet's discharge characteristics are significant, this symmetry may be broken. This makes it more difficult to interpret the fixed EM probe measurements and to take advantage of symmetry to reduce computational cost.

3.3. Experimental Vertical Velocity Plots

The figures below depict the vertical velocity measured by the top, middle, and bottom probes for the three experiment operational scenarios. As previously stated, the NETL data are for 100 cycles for each scenario, and the dashed lines represent the ensemble average. 95% confidence intervals were calculated as discussed in Section 3.1 for each data point and are represented by bars in the figures.

While there are differences in liquid height and drive time among the operating conditions for the three scenarios (Table 2), the velocity probe measurements are very close to each other. At each vertical location, the probe measurements from the three scenarios are within the 95% confidence intervals.

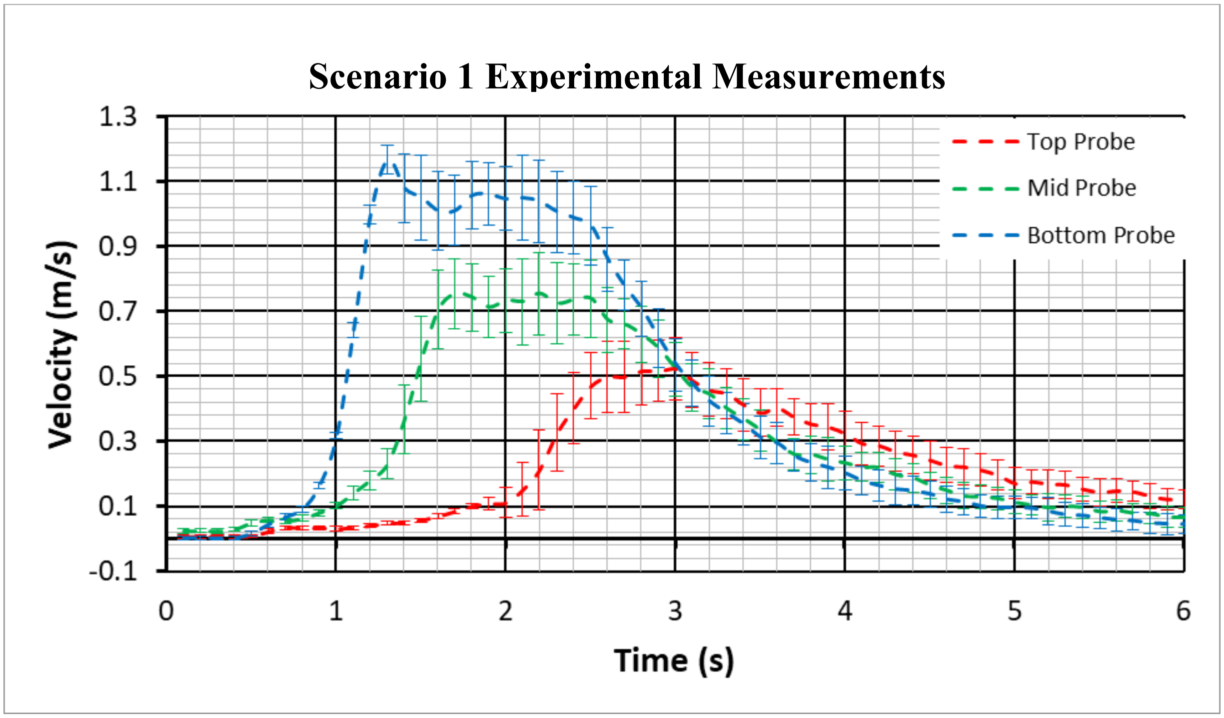

Figure 14. NETL experimental vertical velocity measurements at the three EM probes - Scenario 1. Red, green, and blue lines indicate the measurements from top, middle, and bottom probes, respectively. The bars indicate 95% confidence intervals.

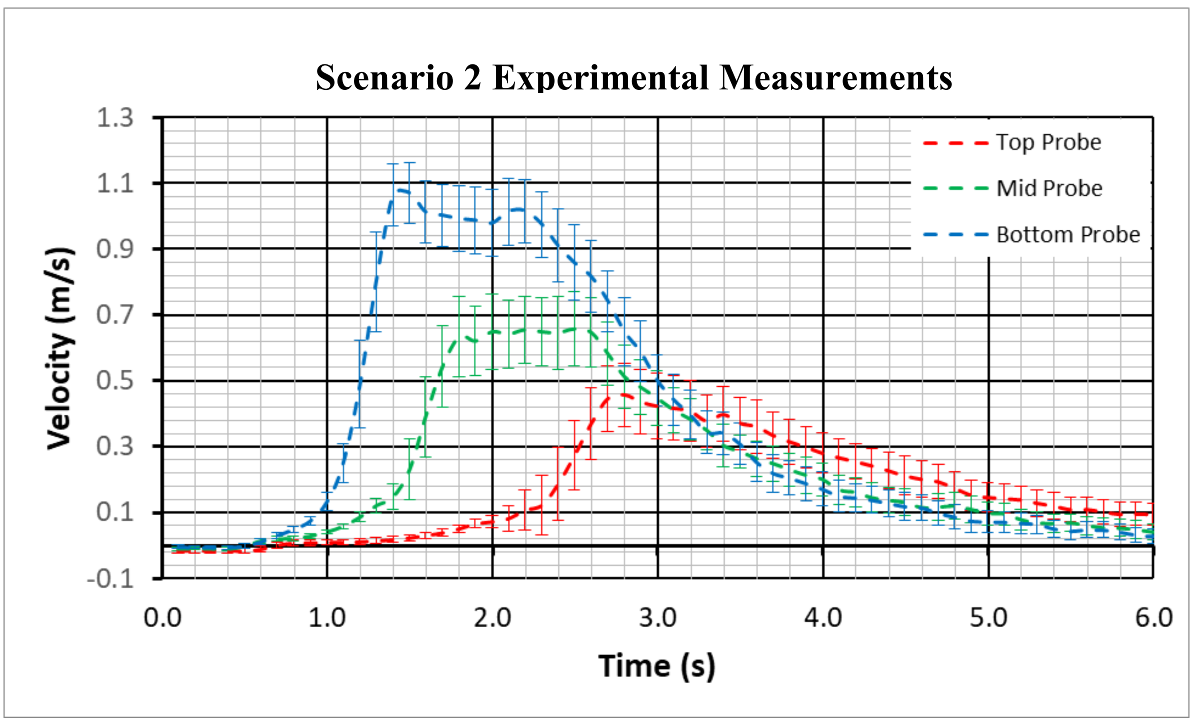

Figure 15. NETL experimental vertical velocity measurements at the three EM probes - Scenario 2. Red, green, and blue lines indicate the measurements from top, middle, and bottom probes, respectively. The bars indicate 95% confidence intervals.

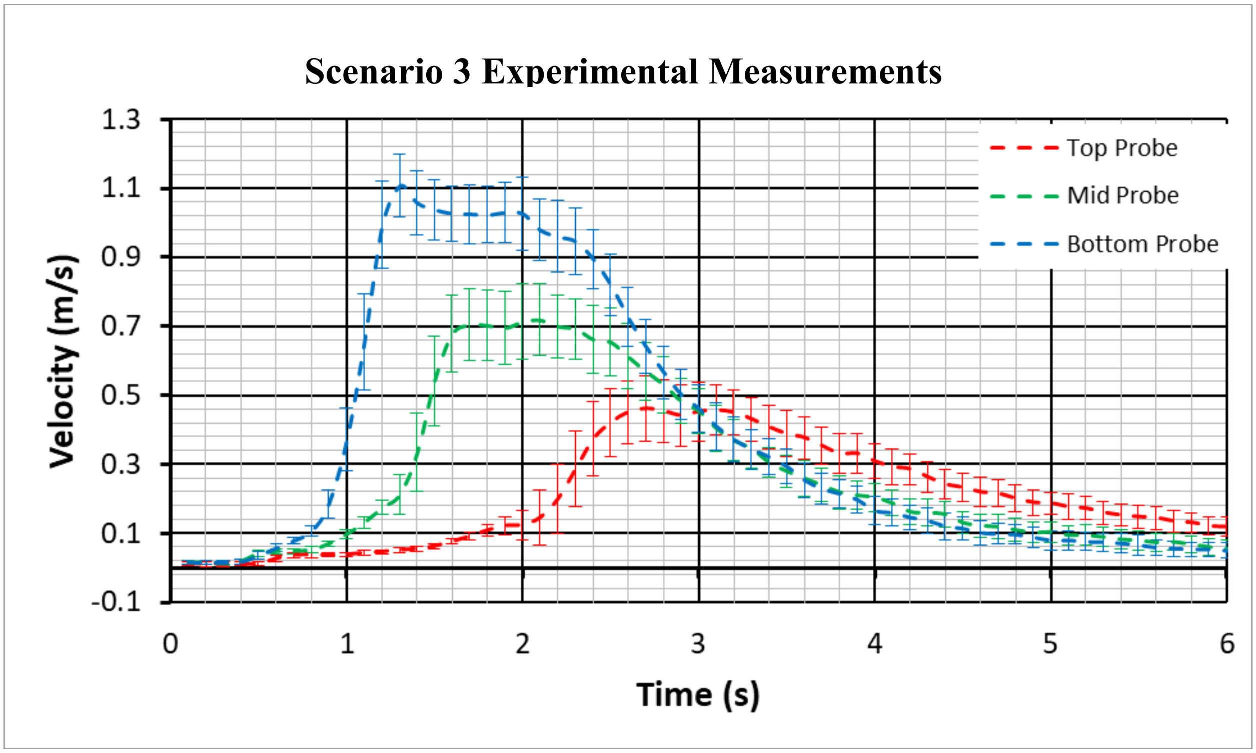

Figure 16. NETL experimental vertical velocity measurements at the three EM probes - Scenario 3. Red, green, and blue lines indicate the measurements from top, middle, and bottom probes, respectively. The bars indicate 95% confidence intervals.

4. Simulation Model Development

Unsteady RANS, LES, and LBM simulation models are tested for the NETL PJM vessel. The development and refinement processes for the three models are discussed in this chapter. Several preliminary studies conducted with the RANS model are described in detail, demonstrating the validity of assumptions regarding gas phase compressibility and liquid phase viscosity range. While other cases were occasionally tested, Scenario 1 on UPP was primarily used for development purposes.

Grid independence studies for RANS, LES, and LBM models are discussed in this chapter to justify the final grids. The overall cell count for each model was gradually increased in an attempt to identify a level at which the key metrics converged. While the cell counts were selectively increased focusing on key regions in the RANS and LES models, the grid was uniformly refined in the LBM model due to its homogeneous lattice structure, by reducing the lattice length scale.

The statistical analyses performed on the LES and LBM models are also discussed in the chapter. Unsteady RANS does not require this effort because it outputs time-averaged prediction at each time during the PJM drive, vent, and suction phases by default. The Section describes how ensemble averages are calculated to represent mean flow fields within the PJM vessel, as well as 95% confidence intervals for numerical data variations around the mean values. It then explains how 95% confidence interval data were used to justify the number of PJM operation cycles simulated for the LES and LBM models.

4.1. Unsteady RANS Model Development

4.1.1. Mesh Independence

Mesh models of varying resolution were created and tested to determine the point at which mesh independence is achieved. The initial mesh was created with the minimal resolution sufficient to capture the essential shapes the vessel and PJM. The mesh was then gradually refined until convergence of key metrics such as the nozzle and central upwash plume velocities (Section 1.2) were identified. The refinement process concentrated on the nozzle, dish bottom, and vessel core regions, which are shown in Figure 17. Good resolution in the nozzle regions is essential for accurately simulating the nozzle flows that drive the PJM operations. Highly refined cells were required in this region as it has the greatest velocity gradient in the vessel. While having lower velocity gradient, the dish bottom region contains highly turbulent and complex flows as a result of nozzle jets colliding with the dish bottom and wall jets along the bottom converging to produce the upwash plume. While the mesh resolution at the bottom of the vessel core region needs to be maintained to ensure a smooth transition from the dish bottom, the fluid velocity in the upper core region is significantly lower and does not require high resolution. As a result, the cell sizes in the core region gradually increase from bottom to top.

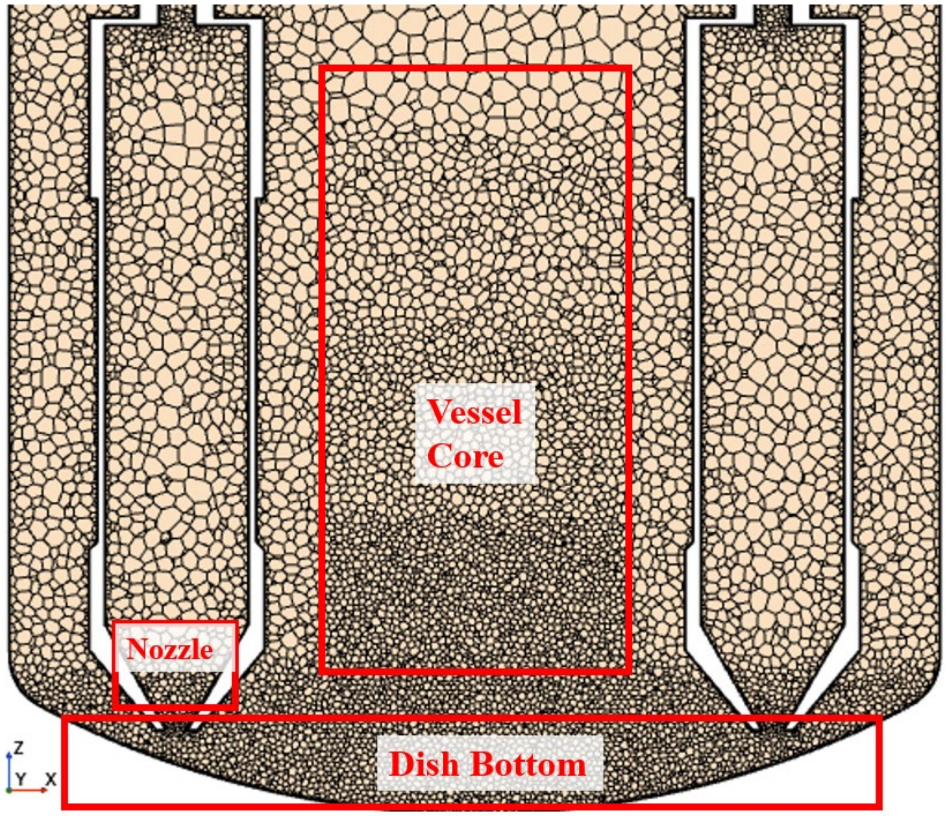

Figure 17. Mesh refinement zones for the NETL PJM vessel displayed on RANS mesh with 1.8 million cells. The refinement process focuses on the nozzle, dish bottom, and vessel core regions to accurately capture velocity and pressure gradients in the area. The example displayed is for UPP, Scenario 1 case.

Figure 18 shows a comparison of nozzle velocities during a drive phase for four different mesh levels with 1.1, 1.5, 1.8, and 2.1 million cells. The nozzle velocities are averaged over the surface marked in pink shown in the figure. The nozzle velocity data vary through 1.5 million cells mesh level but no longer changes beyond the 1.8 million cells mesh level, indicating a convergence behavior. As the average difference in nozzle velocities between 1.8 and 2.1 million cell levels during the drive phase is only 1.2%, the mesh resolution in the nozzle area is determined to be sufficient at this point and is no longer refined.

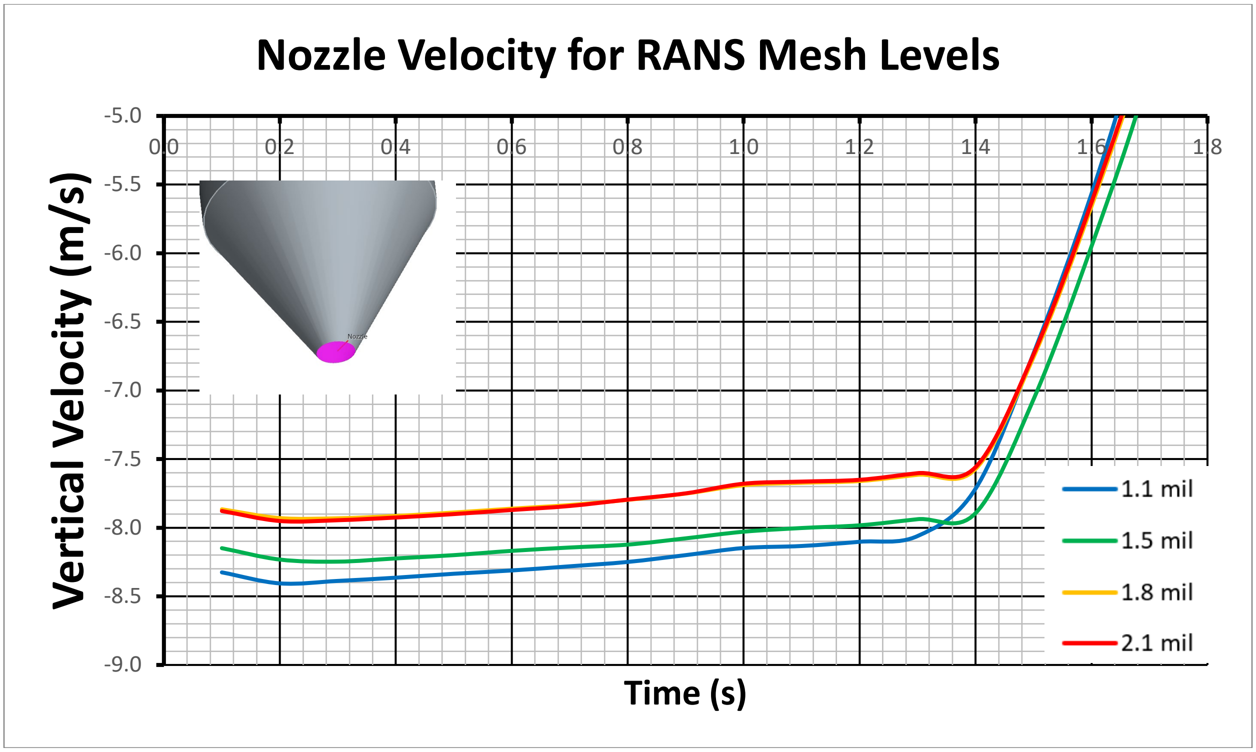

Figure 18. Nozzle velocity for various RANS mesh levels with 1.1 (blue), 1.5 (green), 1.8 (yellow), and 2.1 (red) million cells. The sign is negative because the nozzle jet is pointing in the negative z-direction. Part of the yellow curve is obscured by the red curve due to their similar simulation results.

Figure 19 displays velocity magnitude scalar plots in a nozzle area from RANS mesh levels with 1.1 (left) and 1.8 million cells (right). Compared to the 1.8 million cells mesh, the 1.1 million cells mesh lacks refinement to smoothly capture velocity gradients in the nozzle flow, resulting in artificially high velocity in the area marked by a black circle in the figure. When the 1.8 and 2.1 million cell levels are compared as depicted in Figure 20, the added resolution has no significant effect on the nozzle velocity.

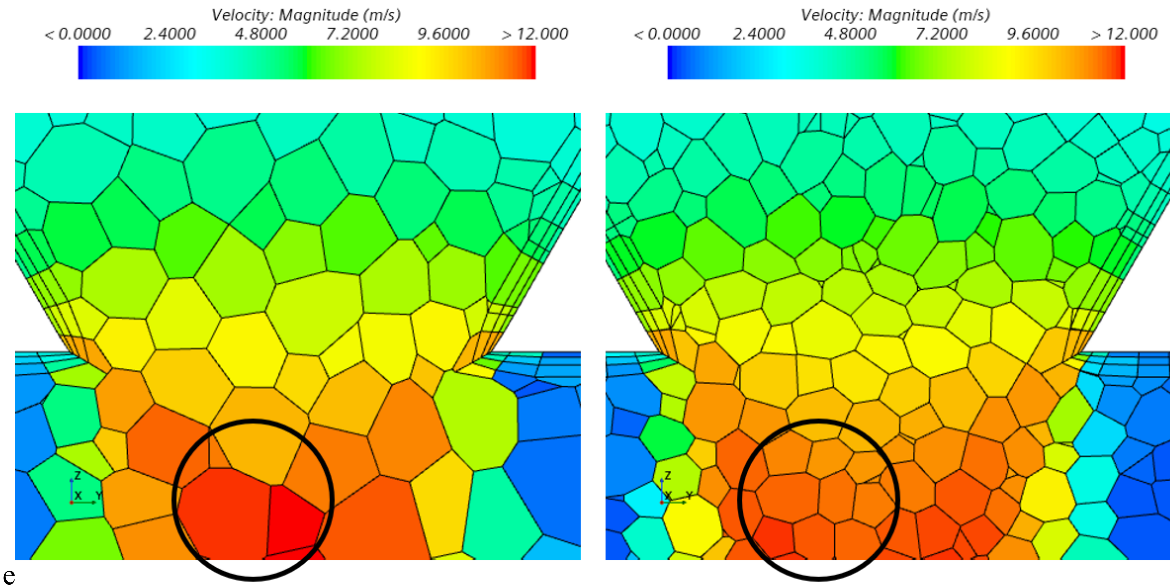

e

Figure 19. Velocity magnitude scalar plot displaying PJM nozzle flows in RANS mesh levels with 1.1 (left) and 1.8 (right) million cells. Colors represent velocity magnitude varying from 0 to 12 m/s, according to the bar provided at the top.

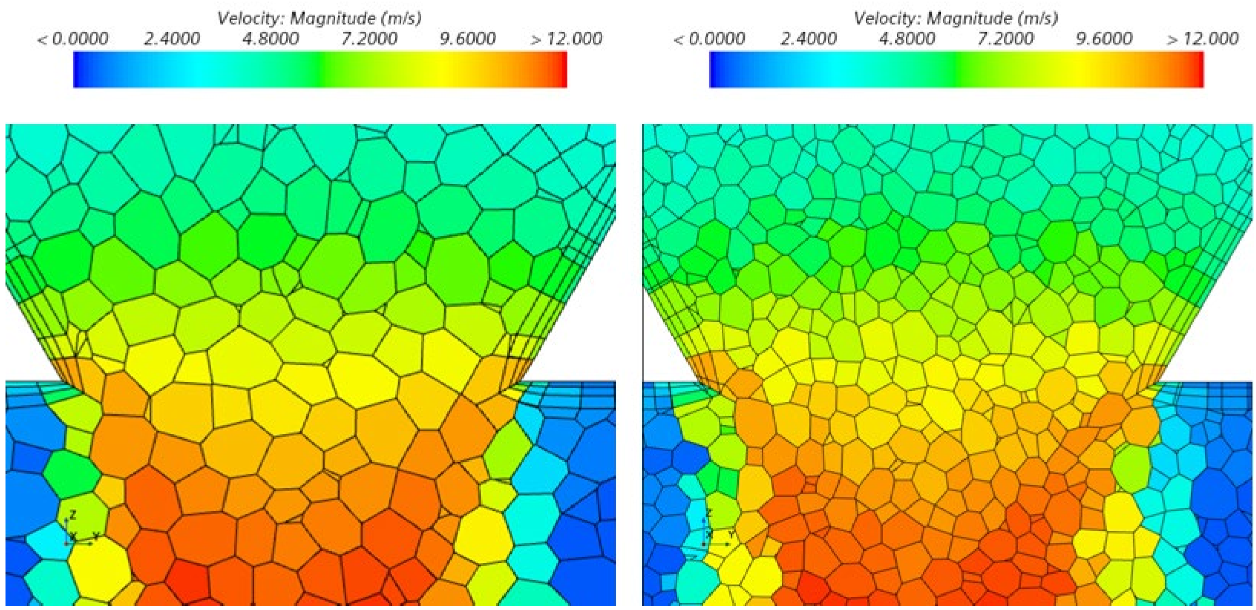

Figure 20. Velocity magnitude scalar plot displaying PJM nozzle flows in RANS mesh levels with 1.8 (left) and 2.1 (right) million cells. Colors represent velocity magnitude varying from 0 to 12 m/s, according to the bar provided at the top.

The same technique was used for vertical plume velocity data to determine mesh independence. The plume velocity data are collected along the vertical center line (shown in Figure 21) at the end of a drive phase and depicted in Figure 22. The figure shows four curves that represent data from 1.1, 1.5, 1.8, and 2.1 million cells mesh levels. On average, the data between mesh levels of 1.8 and 2.1 million cells differ by 2.1%, clearly showing a convergence behavior.

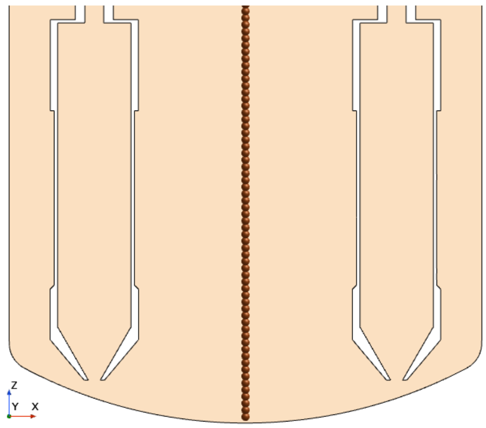

Figure 21. Red dots represent velocity collection points utilized to construct plume central vertical velocity displayed in Figure 22.

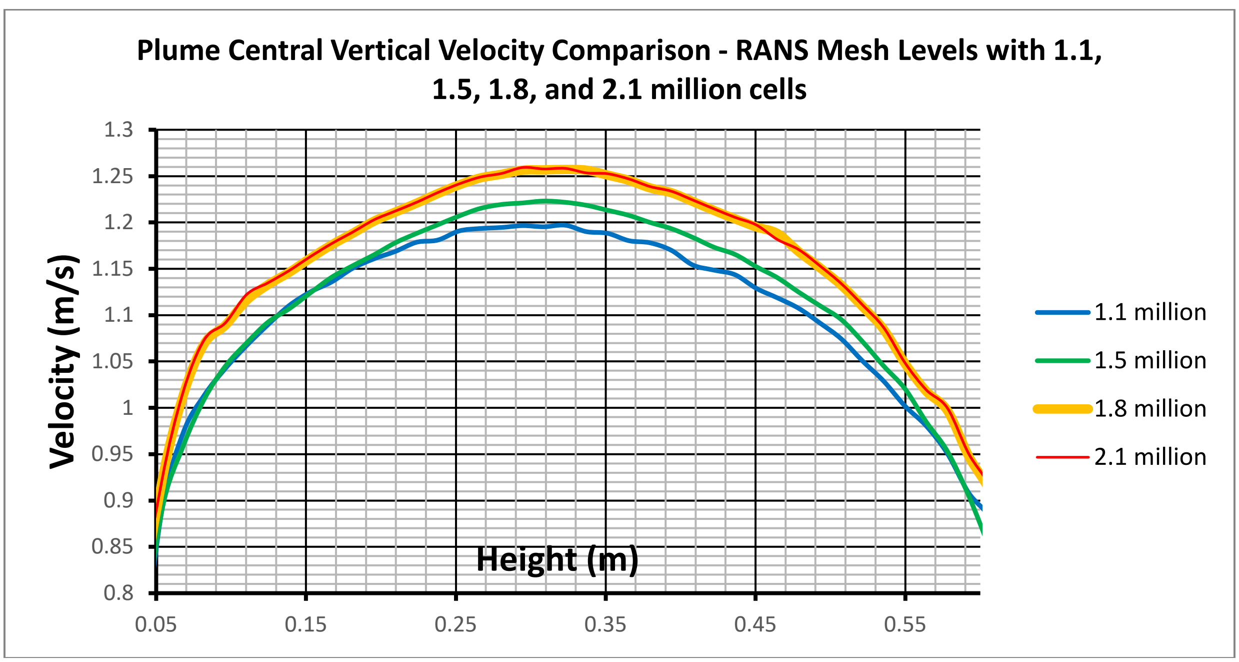

Figure 22. Plume vertical velocity at the end of a drive phase for RANS mesh levels with 1.1, 1.5, 1.8, and 2.1 million cells. The curves for 1.8 million cells (yellow) and 2.1 million cells (red) overlap as the data are nearly identical. Scenario 1, UPP.

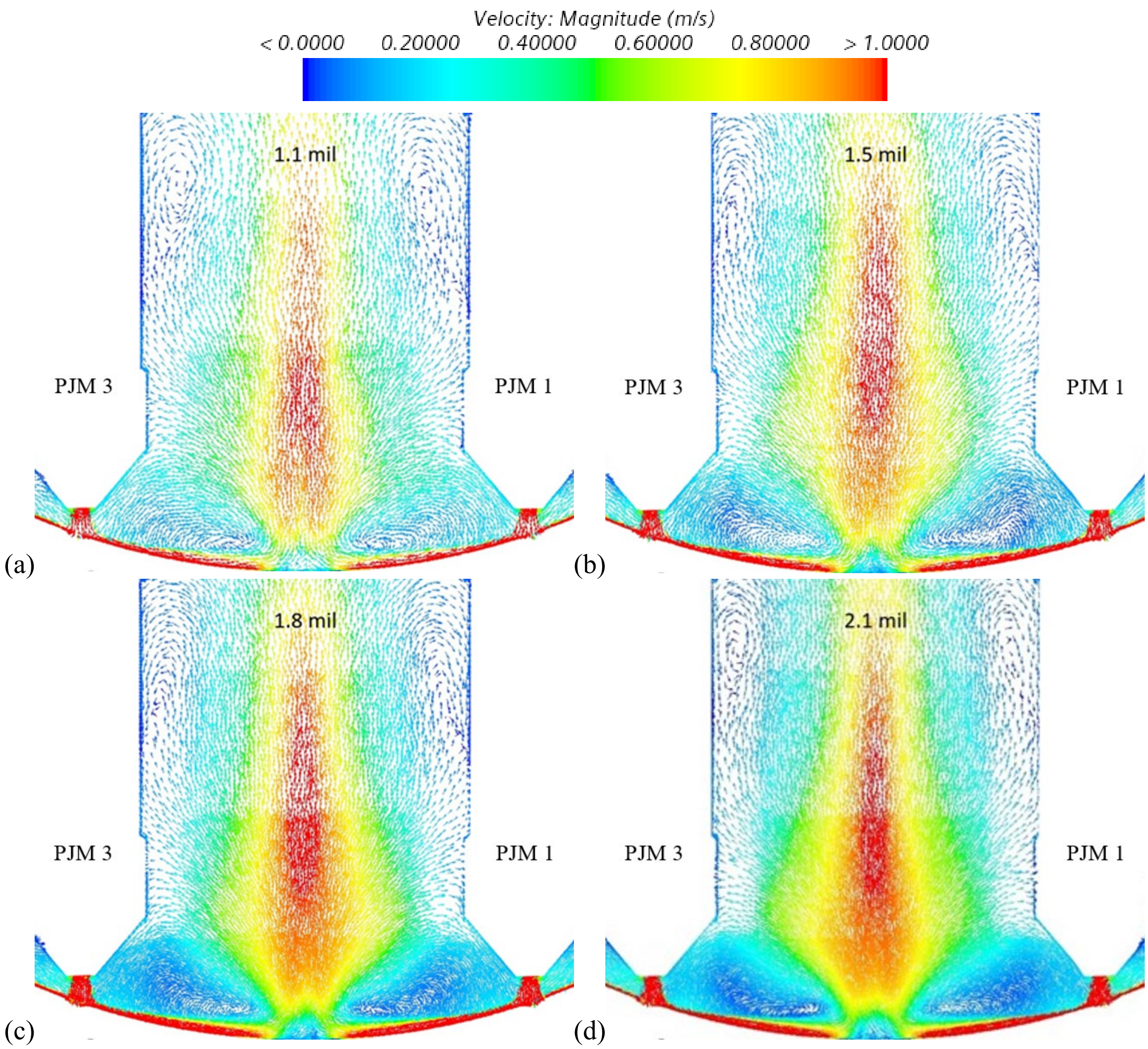

Figure 23. Velocity plots display predictions at the end of a drive phase – (a) 1.1, (b) 1.5, (c) 1.8, and (d) 2.1 million Cells Mesh

Figure 23 shows velocity vector plots on a vertical cross-sectional plane for the four mesh levels at the end of a drive phase. The plane contains two PJM 1 and 3. The PJM arrangement is depicted in Figure 13. While the central plume is captured by all four mesh levels, the higher resolution grids better illustrate velocity gradients around the central plume and the two vortices near the dish bottom. Specifically, the regions exceeding 1.0 m/s (marked by vectors with red color) are wider for the mesh levels with 1.1 and 1.5 million cells, which appear to dilute the core momentum of the plume and contribute towards the lower plume velocities that were discussed for Figure 22.

Finally, velocity measurements at the locations of the EM velocity probes (Figure 12) are compared across the four mesh levels. It is critical to establish mesh independence at these locations since the experimental data from these locations will be used to validate the simulation models (Section 3.3). Figure 24 shows the vertical velocities measured at the bottom, middle, and top probe locations from mesh levels with 1.1, 1.5, 1.8, and 2.1 million cells. The figure shows that only the results from the 1.8 million cell level are comparable to those from the 2.1 million cell level.

To confirm that the velocities data are mesh independent at 1.8 million cells level, a quantitative analysis is performed. Percentage differences of the velocity measurements at the bottom probe location are calculated between subsequent mesh levels and listed in Table 3. While the 8.2% maximum difference between the 1.8 and 2.1 million cells mesh levels appears significant, it only occurs briefly during the drive phase and the average difference is significantly lower at only 2.5%. Furthermore, an additional mesh refinement level of 2.5 million cells did not reduce the maximum difference, as shown in Table 3.

Based on the convergence behaviors of the PJM nozzle, vertical plume, and EM probe location velocities, it is determined that for the 1.8 million cell and larger meshes, resolution is not a factor in simulation performance. As a result, the 1.8 million cell mesh is used in the study for the RANS model, including the preliminary studies described below.

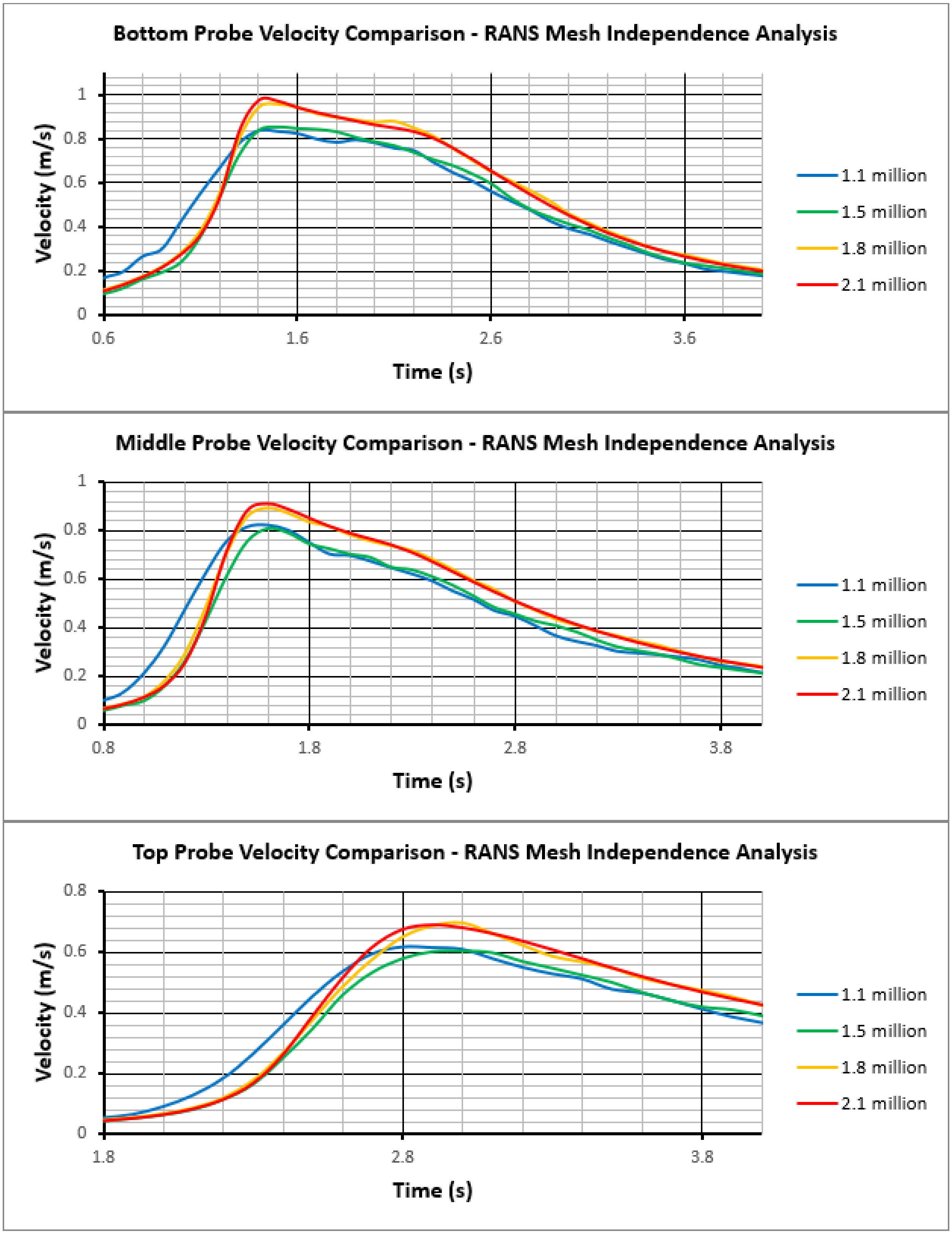

Figure 24. Vertical velocity predictions vs. Time at the three (bottom, middle, and top) EM probe locations of Figure 12. Four curves represent data from 1.1, 1.5, 1.8, and 2.1 million cells mesh levels. Convergence behavior identified at 1.8 million cells level. Scenario 1, UPP.

Table 3. Maximum and average percentage difference in vertical velocity measurements at the bottom probe location of Figure 12. The differences are calculated between subsequent mesh levels to identify convergence.

	Max Difference (%)	**Average Difference (%)**
1.1 mil vs. 1.5 mil	34	14
1.5 mil vs. 1.8 mil	15.7	8.2
1.8 mil vs. 2.1 mil	8.2	2.5
2.1 mil vs. 2.5 mil	8.6	2.4

4.1.2. Effect of Gas Compressibility

The internal air pressure supplied to the PJM's via the jet pump pair drives the water discharge from the PJM nozzle into the vessel. The compressibility of the gas phase may affect the volumetric flow rate at the nozzle and the motion of the upward plume. So far, simulation studies of PJM mixed vessels have treated the gas phase as incompressible [8], but no validation records for the assumption have been presented. Studies have shown that a volume of air trapped by incompressible liquid and solid boundaries can cause pressure oscillations due to air-cushion effects, with varying consequences depending on the scale and complexity of the geometry [23], [24].

To test the role of compressibility, two RANS simulations cases were performed: one assuming that the gas phase is incompressible and the other assuming that the air behaves like an ideal gas. Figure 25 and Figure 26 show the resulting nozzle velocity and PJM pressure predictions for the two models. The nozzle velocity is averaged over the cross section of the nozzle opening, and the PJM pressure is measured at the junction between a PJM and a gas line (illustrated in Figure 7). According to the numerical data, the ideal gas case predicts slightly higher pressure than the incompressible case, with a 0.5% increase in nozzle velocity on average. A comparison of simulation run times between the two cases revealed that the incompressible gas model requires 3% less simulation time per cycle than the ideal gas model. Based on the insignificant difference in results and the slight performance advantage, all subsequent simulations of the study treated the air phase as incompressible.

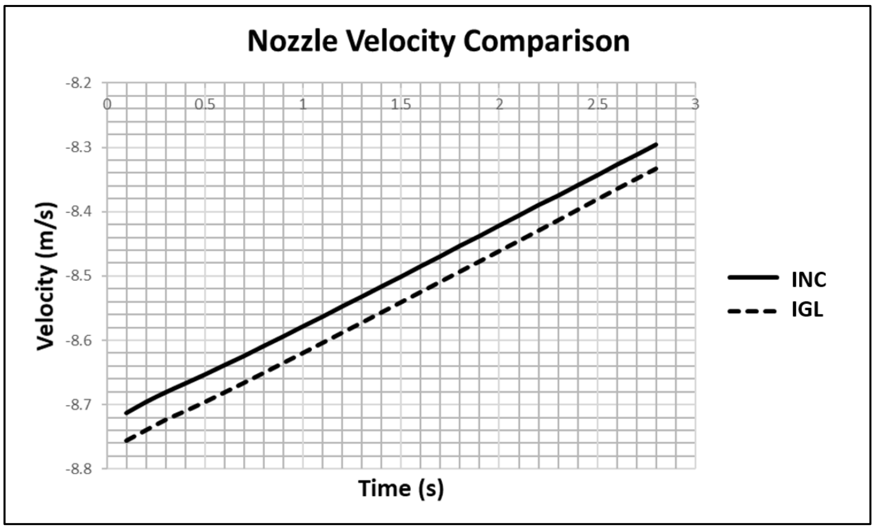

Figure 25. Nozzle velocity comparison between incompressible gas (INC) and ideal gas law (IGL) RANS simulations throughout a drive phase. While INC case shows slightly lower values, the differences are not significant. Scenario 1, UPP.

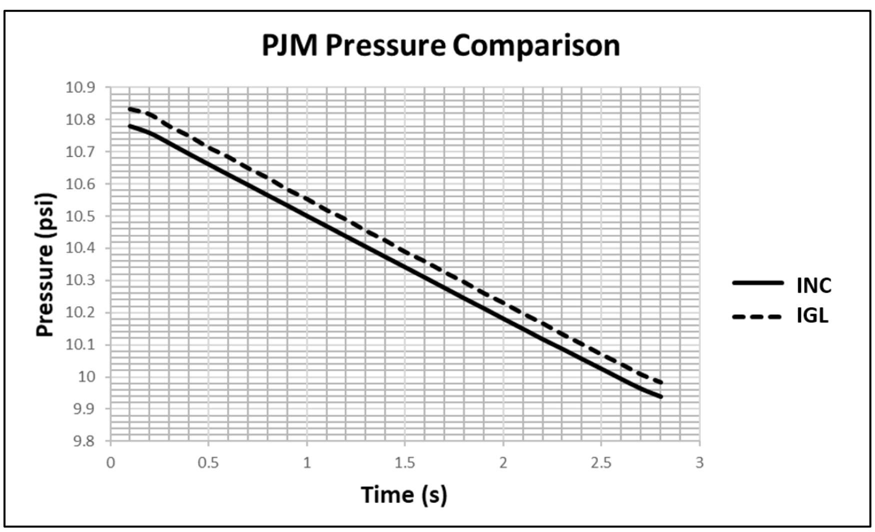

Figure 26. PJM pressure comparison between incompressible gas (INC) and ideal gas law (IGL) RANS simulation cases throughout a drive phase. While INC case shows slightly higher values, the differences are not significant. Scenario 1, UPP.

4.1.3. *Fluid Viscosity*

Although the NETL laboratory PJM vessel study only used water for the experimental measurements, fluid viscosity remains an important factor for the device's future development. When the single liquid assumption is valid, waste solutions with low non-cohesive solid loads (less than 5% in weight) can be simulated using Newtonian fluids of varying viscosity [8].

To better understand the effect of fluid viscosity on the stability and performance of the NETL PJM simulation model, it was tested with an arbitrary simulant called 30-cP fluid, which has fluid properties of water except for its 30-cP viscosity. The 1.8 million-cell mesh and UPP were utilized for this test. Figure 27 depicts a comparison of nozzle velocities over a PJM cycle for water and 30-cP fluid simulations. The results show that the nozzle velocity and PJM pressure profiles in the water and 30-cP simulations are nearly identical, with the difference peaking at 0.05% during the drive phase. This is due to the high velocity near the nozzle, which places the flow in both simulation cases well within the turbulent regime, minimizing the impact of fluid viscosity.

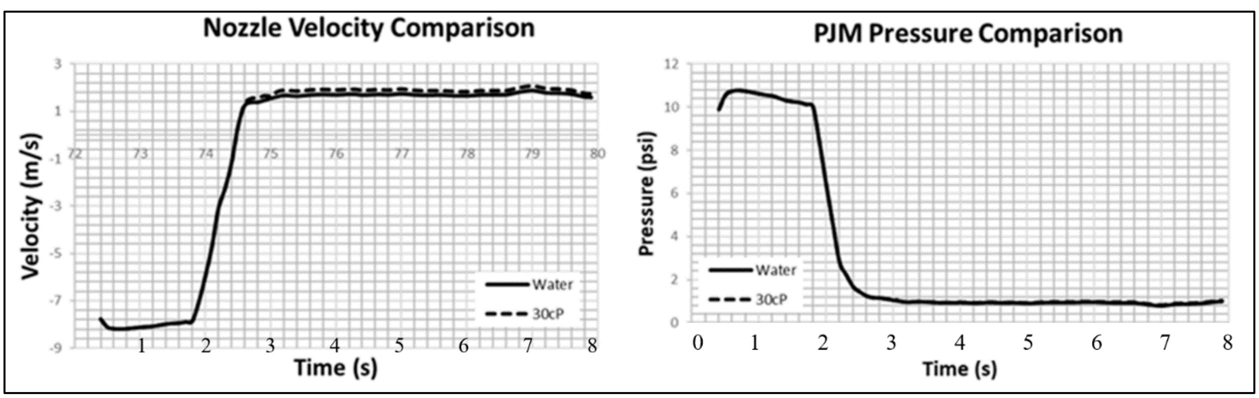

Figure 27. Cross-sectionally averaged Nozzle velocity and PJM internal pressure data from water (solid line) and 30-cP fluid (dashed line) cases of the RANS simulation model. The curves overlap as there are no significant differences among the data. Scenario 1, UPP.

To understand the effect of fluid viscosity on the rest of the vessel flows, Reynolds numbers are calculated and listed in Table 4 for various regions including the PJM and vessel core. The vessel core is taken as a cylindrical area with a diameter of 0.41 m that is located in the vessel's center, as shown in Figure 28 (b). The region is selected to contain the majority of the central plume's upward movement. According to the table, the Reynolds numbers for the PJM and vessel core are significantly lower than those for the nozzle, and the flows in the 30-cP simulation case are not fully turbulent.

Table 4. Reynolds numbers at various NETL PJM vessel regions during a drive cycle

	Length Scale (m)	**Drive Velocity* (m/s)**	**Reynolds Number**	
			Water	30-cP
PJM	0.154	0.252	38700	1290
Nozzle	0.0254	9.83	249000	8320
Vessel Core	0.410	0.0298	12200	407

**Averaged over a drive phase*

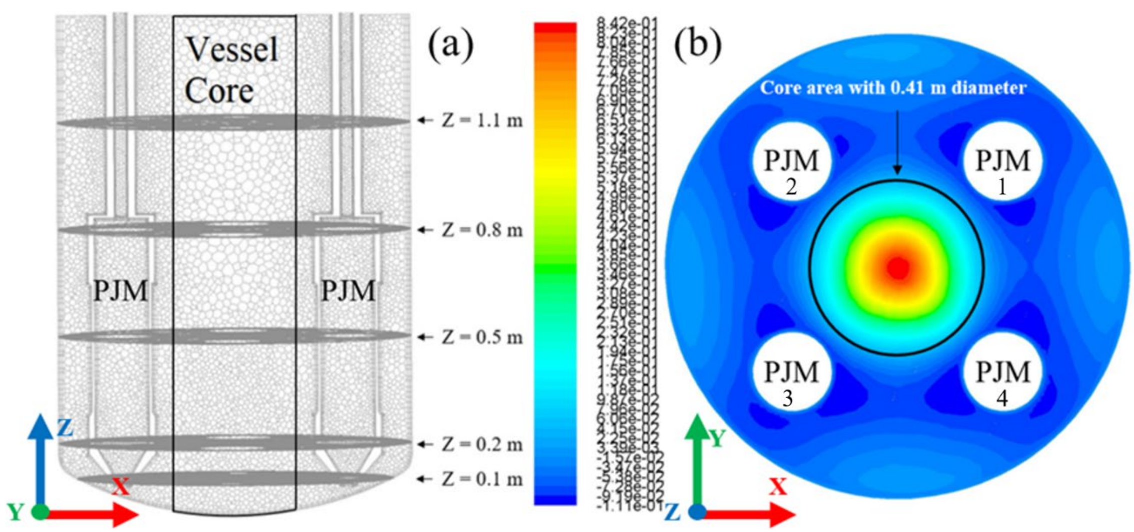

Figure 28. (a) shows vertical plane locations in the vessel. The height values are calculated from the central point of the vessel bottom. (b) illustrates the vessel core area, which is utilized to calculate vessel core averaged values, as shown in Figure 29.

To investigate how fluid viscosity affects flows in a region with low Reynolds number, five planes of varying heights (z = 0.1, 0.2, 0.5, 0.8, 1.1 m) are defined within the vessel core, as shown in Figure 28 (a). Average velocities are calculated on each plane, and the results from the water and 30-cP fluid RANS simulations are provided in Figure 29.

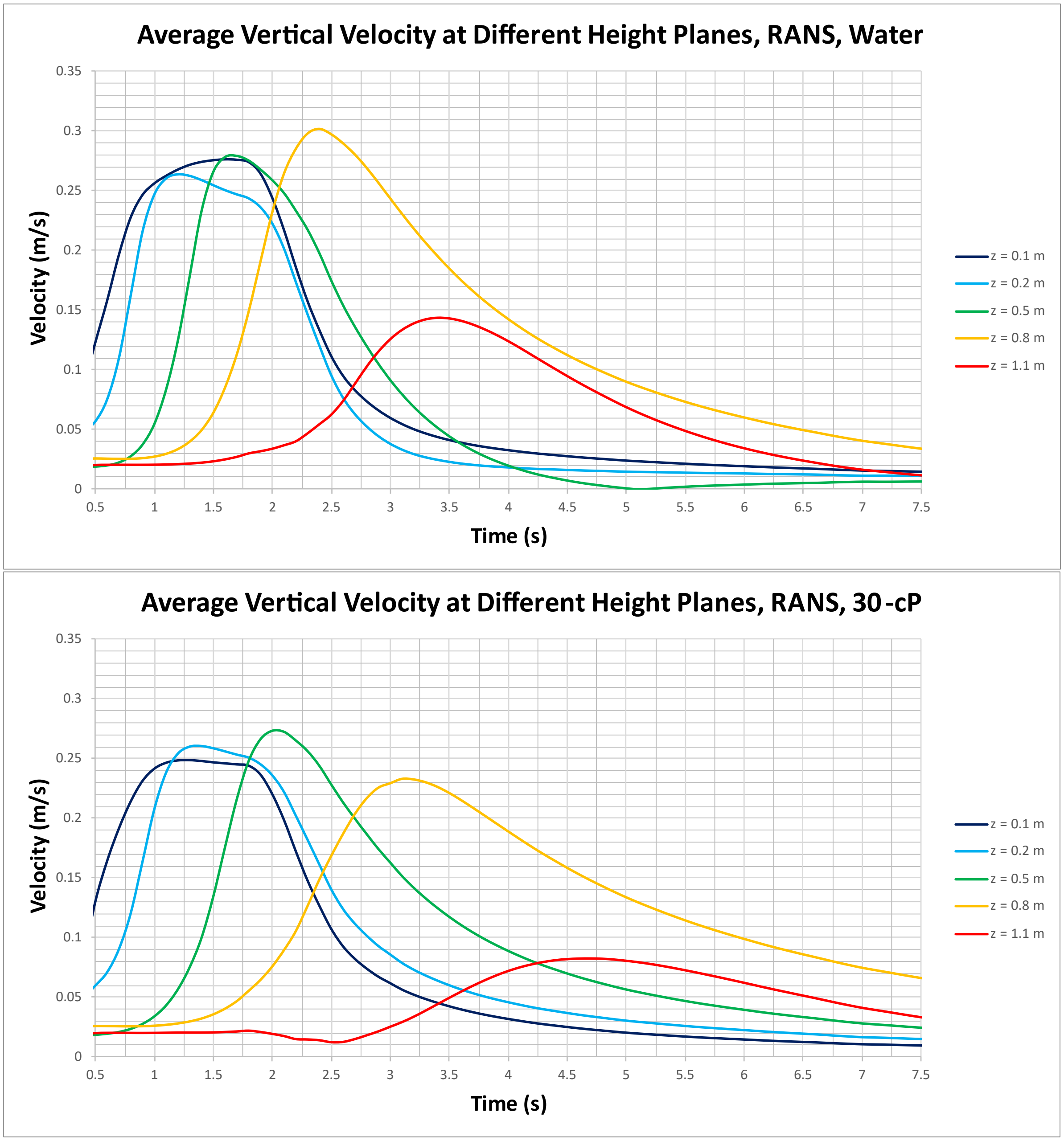

Figure 29. Average vertical velocity of vessel core at different heights taken from RANS simulation Water (top) and 30-cP Fluid (bottom) cases. The velocities are plotted against time throughout a PJM mixing cycle. Scenario 1, UPP

There are two factors that cause the 30-cP data curves to appear "stretched" in comparison: compared to the water case, the vertical velocities are generally lower, and the maximum values occur later into the PJM cycle in the 30-cP fluid case. This is caused by the higher viscosity of the 30-cP fluid that works against the formation and movement of the central plume.

The impact of fluid viscosity is more noticeable in the upper regions where the fluid flows are characterized by even lower Reynolds number. While the velocity curves of the two cases are similar in shape at z = 0.1 and 0.2 m, they differ significantly at z = 0.8 m (yellow curve) and z = 1.1 m (red curve). To make the comparison quantitatively, the magnitude and timing of the maximum velocity at each height are provided in Table 5. The data clearly shows stronger impact of fluid viscosity at higher planes.

Table 5. The magnitude and timing of vessel core vertical velocity at each plane height. RANS water and 30-cP fluid simulation cases. Scenario 1, UPP.

	Max. velocity (m/s)		**Max. time* (s)**	
	Water	**30-cP fluid**	**Water**	**30-cP fluid**
z = 0.1 m	0.26	0.26	1.1	1.3
z = 0.2 m	0.28	0.25	1.5	1.2
z = 0.5 m	0.28	0.27	1.6	1.9
z = 0.8 m	0.30	0.23	2.3	3.0
z = 1.1 m	0.14	0.083	3.3	4.6

**Time at which the max. velocity is achieved at each height plane.*

The exercise demonstrates the model's ability to incorporate the effects of fluid viscosity in PJM vessel simulations. While the findings cannot be validated due to a lack of empirical data, they are consistent with other experimental studies. A PJM vessel study revealed that when water and highly viscous non-Newtonian clay were used, PJM pressure and nozzle velocities were comparable [21]. Other research has shown that in high viscosity fluids, higher nozzle velocities are required to achieve a comparable degree of plume vertical velocity [4], [5]. Given the Reynolds number magnitude away from the nozzle a RANS formalism cannot be expected to perform well in more quiescent regions of the vessel, demonstrating a need for more sophisticated models such as the LES and LBM models discussed below.

4.2. LES Model Development

The development of the LES simulation models is described in this Section. While statistical analysis and mesh independence are discussed separately, the two components were used in tandem during the development process; mixing cycles were repeatedly simulated at each mesh level until statistical analyses showed convergence. Sections 4.2.1 and 4.2.2 will present the process in greater detail.

4.2.1. Statistical Analysis

Because LES generates instantaneous filtered flow fields, statistical analysis is required for model verification and validation which utilize time averaged mean data at various points during the PJM drive and suction cycles. The procedure described in Section 3.1 is applied to calculate the ensemble mean along with 95% confidence intervals (eq. 22) to show the variability of the data.

The simulation model accumulates data samples for statistical analysis by repeating PJM operation cycles until the confidence intervals demonstrate convergence behavior. With a large enough sample size, the intervals should shrink to an insignificant range, indicating that the mean value is a good representation of the flow field. Figure 30 shows how 95% confidence intervals change as 20, 60, 80, and 100 cycles of simulated PJM cycles accumulate. The simulation data are collected at the location of the bottom velocity probe location because it shows the most variability among the velocity probe locations and its data are the last to converge.

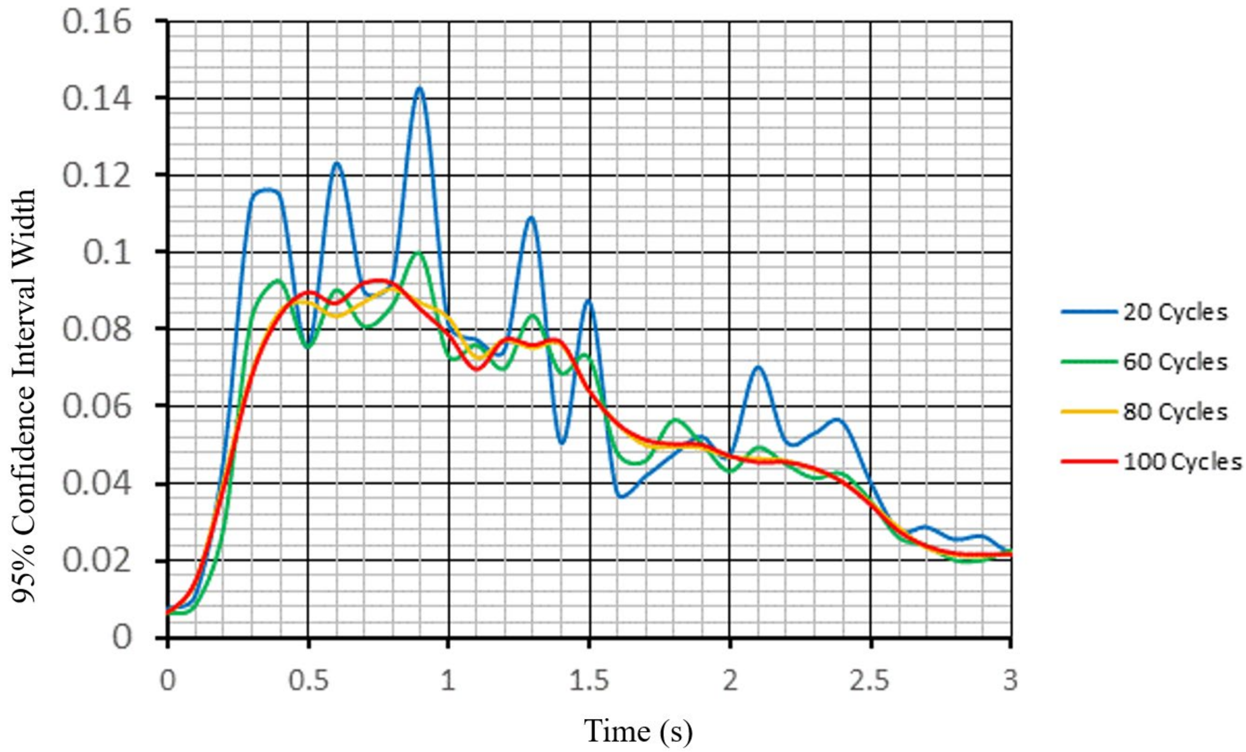

Figure 30. Bottom probe location velocity 95% confidence interval calculated with LES simulation sample sizes of 20, 60, 80, and 100 cycles. As the sample size grows, the fluctuations subside. Scenario 1, UPP.

The confidence intervals calculated from the first 20 cycles show significant variability, as shown by the blue curve. With 60 cycles of simulation data accumulated, the green curve is noticeably smoother, indicating that the data are converging. Finally, the yellow and red curves look nearly identical, indicating that additional data no longer has a significant impact on the confidence intervals beyond accumulating 80 cycles.

Expanding the field of view, Figure 31 shows two-dimensional velocity vector plots of LES mean velocity data from 20, 60, 80, and 100 cycles. As a reference, the top two plots (a and b) show instantaneous velocity data. The bottom four plots (c, d, e, and f) show the ensemble average of 20, 60, 80, and 100 simulated cycles at the end of the drive phase, demonstrating how averaged flow fields converge as more simulated cycles are accumulated. When the plot of 60 averaged cycles (d) is compared to that of 20 cycles (c), the central plume structure is more clearly visible; the velocity changes smoothly from the center of the plume to the periphery. The ensemble average of 80 and 100 cycles (plots e and f) appear qualitatively identical.

To quantify the convergence behavior, the velocity difference between each subsequent sample size is calculated as an average over the entire vertical cross section. Table 6 summarizes the findings. At 1.94 % averaged difference compared to the previous level, the sample size of 100 cycles is deemed sufficient to produce statistically significant results. Consequently, all LES simulation cases in this study are run out to achieve a sample size of 100 cycles.

Table 6. The percentage of vertical cross section velocity difference between each subsequent sample size.

Sample Size	Average Difference* (%)
20 cycles vs 60 cycles	23.3
60 cycles vs 80 cycles	5.12
80 cycles vs. 100 cycles	1.94

**averaged over the entire vertical cross section displayed in Figure 31.*

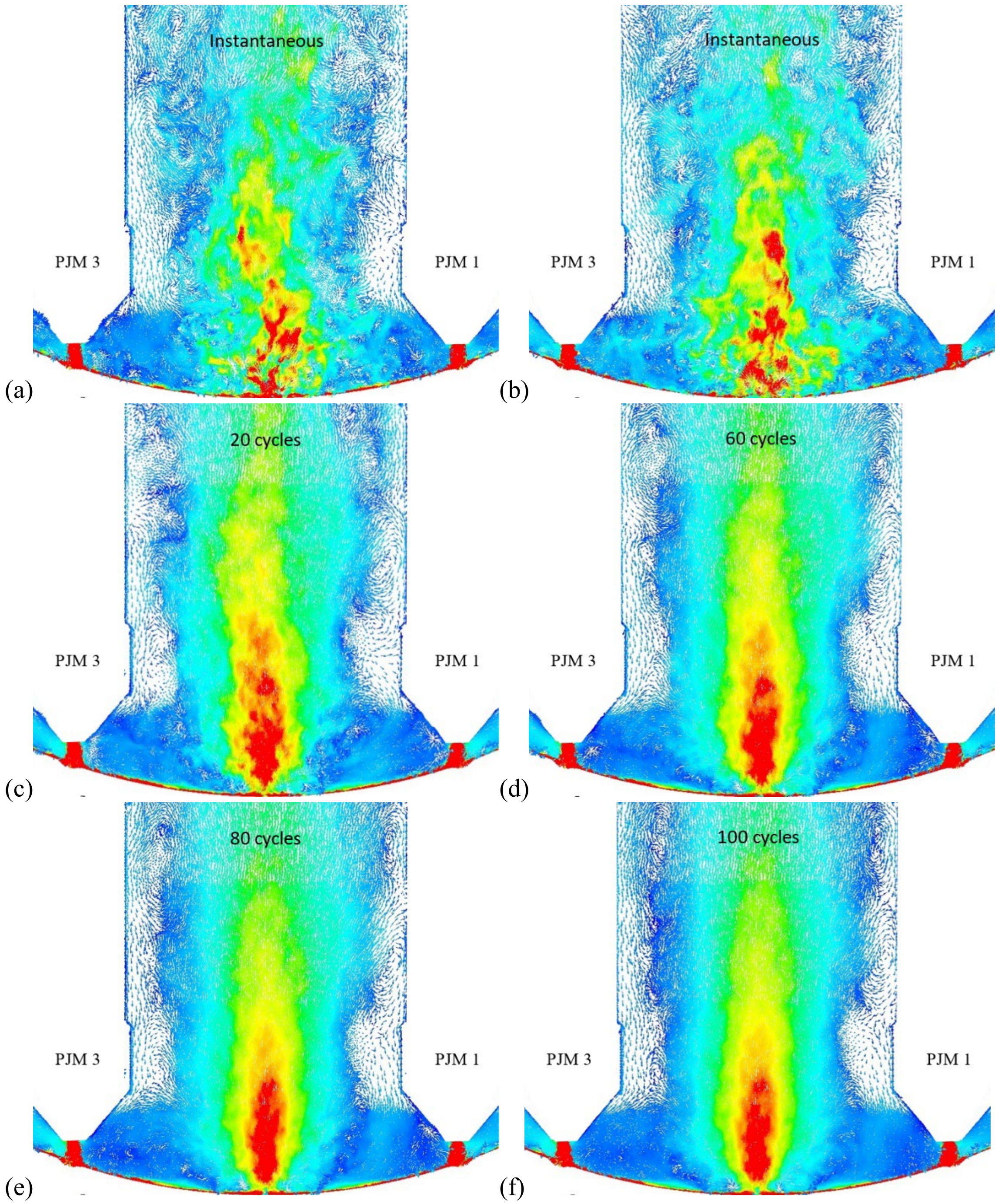

Figure 31. Flow vector field plots on a vertical cross-sectional plane at the end of the drive phase. Top two figures (a and b) show instantaneous flow fields at 10th and 20th cycles. Bottom four (c through f) are time averaged flow fields of varying sample size: 20, 60, 80 and 100 cycles. Scenario 1, UPP.

4.2.2. Mesh Independence

The LES mesh was systematically refined to produce 6 levels with cell counts ranging from 2.0 to 20 million, and the results were compared to identify a level that establishes mesh independence. Because of the reasons discussed in Section 2.2.2, LES requires a considerably more refined mesh than RANS. The SGS turbulence ratio (M) is monitored to ensure that the mesh is sufficiently refined. M is defined as follows:

$$M = {}^{TKE_{SGS}}\!\big/_{(TKE_{SGS} + TKE_{Res})} \qquad (31)$$

where TKE_{Res} is turbulence kinetic energy resolved by the mesh and TKE_{SGS} is that predicted by the SGS or sub-grid scale model. M = 0 therefore denotes no SGS turbulence (all turbulent scales resolved), whereas M = 1 denotes a region with zero resolved turbulence. The mesh for the LES model is refined to have a M value equal to or less than 0.2 in the entire fluid region, indicating adequate resolution to capture the key eddies [25].

Figure 32 compares nozzle velocities averaged in the cross section at the end of a drive phase for four different mesh levels (2.0, 4.5, 12, and 16 million cells). The error bars represent 95% confidence intervals. The nozzle velocity data from 12 to 16 million cells look nearly identical, indicating convergence. The mesh resolution in the nozzle area is determined to be sufficient and is not further refined because the average difference in nozzle velocities between the two mesh levels during the drive phase is only 1.4%. Figure 33 depicts velocity magnitude plots for meshes of 12 and 16 million cells. The plots clearly show that increasing the resolution has little effect on the fluid flows in the region.

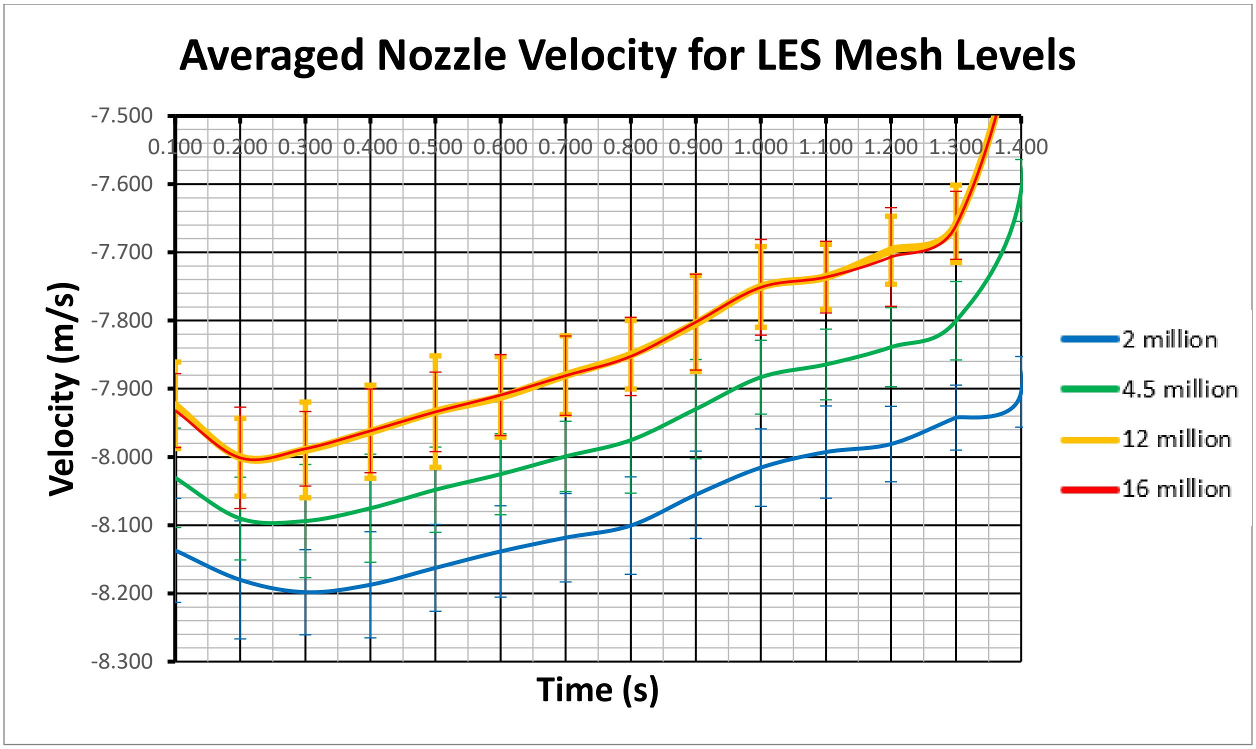

Figure 32. Nozzle velocity for various LES mesh levels with 2.3 (blue), 4.5 (green), 12 (yellow), and 16 (red) million cells. The vertical velocity is negative because the nozzle jet is pointing downward, in the negative z direction. Scenario 1, UPP.

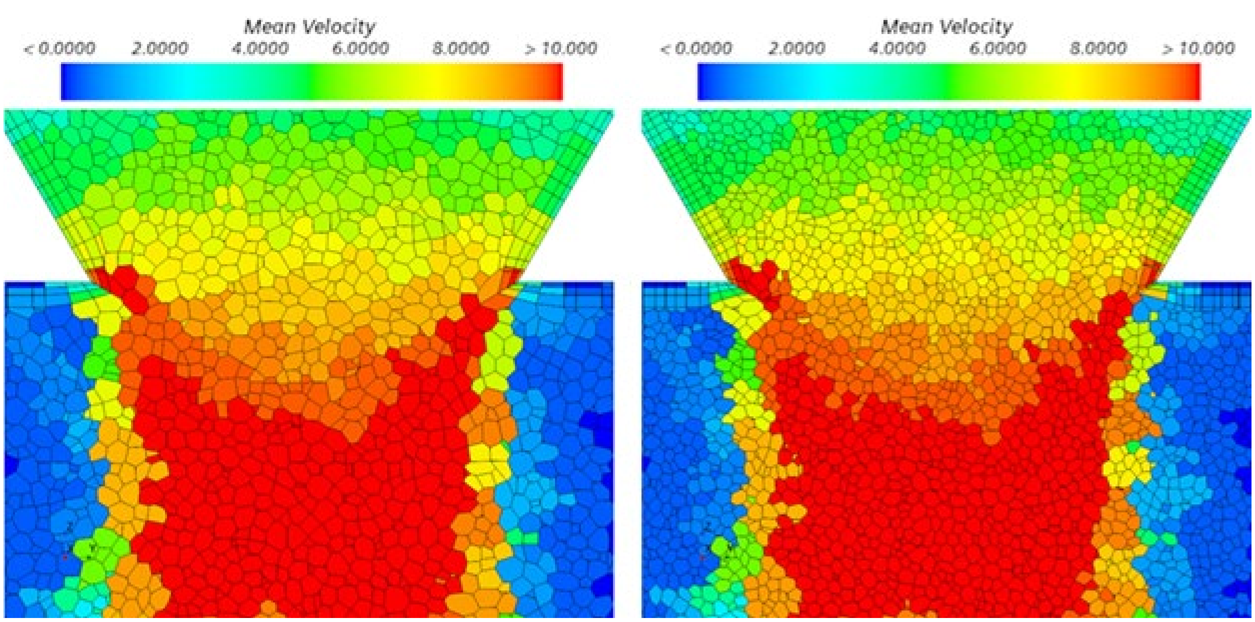

Figure 33. Velocity magnitude scalar plot displaying nozzle flows for LES mesh levels with 12 (left) and 16 (right) million cells. Colors represent velocity magnitude varying from 0 to 10 m/s, according to the bar provided at the top. Scenario 1, UPP.

Velocity data are collected along the vessel's vertical center line (shown in Figure 21) at the end of a drive phase and displayed in Figure 34 to investigate mesh independence in the central plume region. The four curves in the figure represent data from mesh levels of 2.0, 4.5, 12, and 16 million cells. While the levels of 2.0, 4.5, and 12 million cells result in significantly different plume velocity data, the curves of 12 and 16 million cells appear nearly identical and are well within 95% confidence intervals. The average difference between the two mesh levels is small enough (3.2%) to indicate mesh independence.

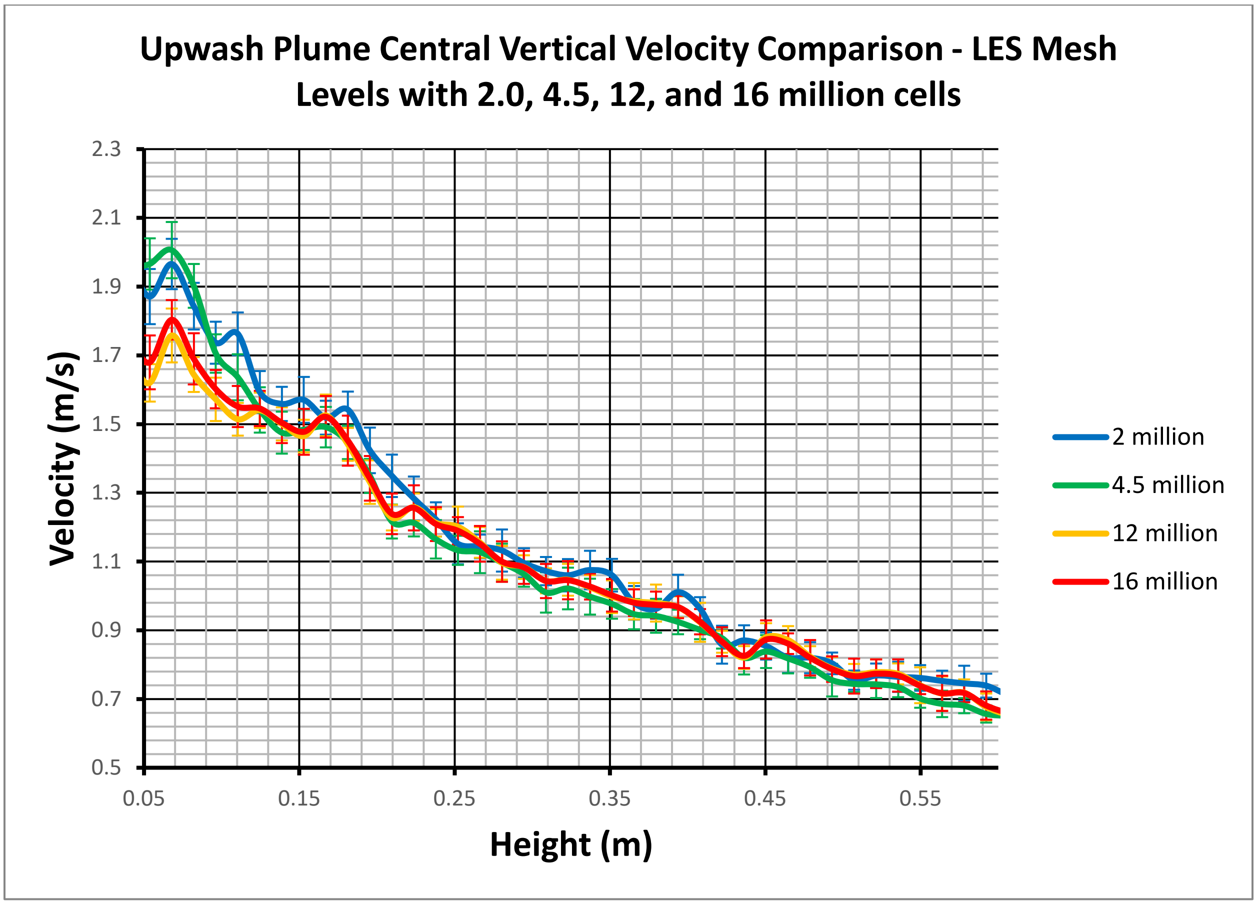

Figure 34. Upwash Plume vertical velocity at the end of a PJM drive phase for LES mesh levels with 2.0, 4.5, 12, and 16 million cells. The bars indicate 95% confidence intervals. Scenario 1, UPP, at the end of drive phase (t = 1.6 s).

Mean velocity vector plots of LES mesh levels captured at the end of a drive phase are shown in Figure 35. While all mesh levels capture the overall nozzle jet and plume structures well, only mesh levels with 12 million cells or higher capture local details. For example, the eddies at the edge of the central upwash plume (represented by the black circles in the figure) are significantly smaller for refined models, which are important in shaping the central plume's boundary.

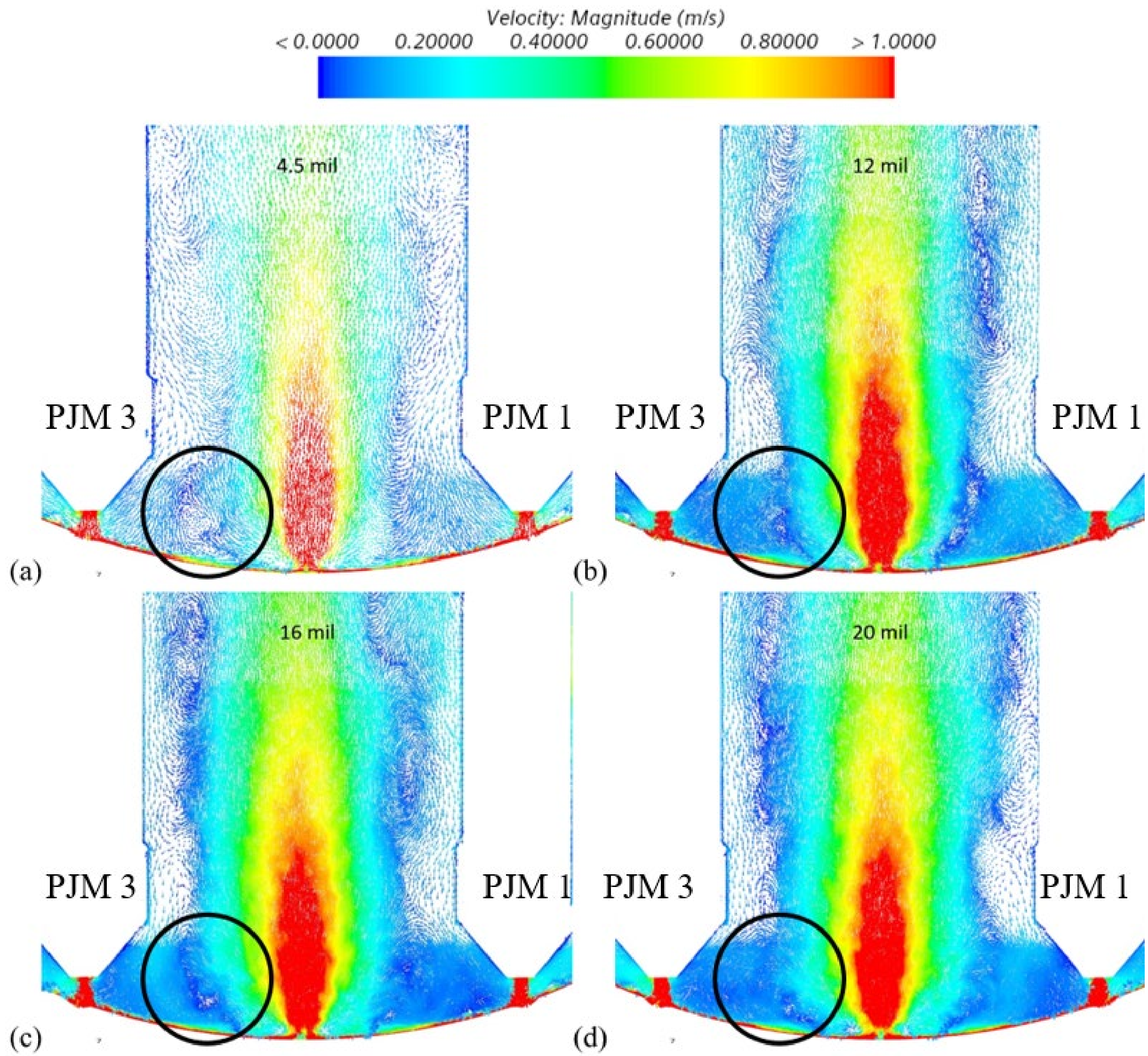

Figure 35. Averaged flow vector field plots on a vertical cross-sectional plane at the end of the drive phase. The four plots (a through d) show the results from varying mesh levels with 4.5, 12, 16, and 20 million cells. Displayed velocities are the ensemble average over 100 cycles for each mesh level. Scenario 1, UPP.

An equivalent comparison based on RMS velocity instead of mean velocity yielded a similar conclusion. The figures and graphs are available in the Appendix (8.4).

Figure 36 shows the simulated velocity prediction at the EM probe locations for the various mesh levels plotted against time to continue the comparison quantitatively. In the figure, the yellow, red, and purple curves (12, 16, and 20 million cell mesh levels) show convergence and are mostly within confidence intervals of each other.

To provide a clearer indication of mesh independence at the 12 million cell level, percentage differences in velocity measurements at the bottom probe location are calculated and listed in Table 7. While the difference between 12 and 16 million cells peaks briefly at 10.7%, the average difference is much lower at 3.36%. Furthermore, an additional mesh refinement level of 20 million cells did not reduce the maximum difference, supporting mesh convergence of the 12 million cells model.

The nozzle, vertical plume, and EM probe location velocity convergence behaviors strongly suggest that mesh resolution is not a factor in simulation performance beyond the 12 million cell model. As a result, the 12 million cell mesh is used for LES model validation and exploitation.

Table 7. Maximum and average percentage difference in velocity measurements at the bottom EM probe location of Figure 12. The differences are calculated between subsequent mesh levels to identify convergence.

	Max. Difference (%)	**Average Difference* (%)**
4.5 mil vs 8.5 mil	50.9	13.3
8.5 mil vs. 12 mil	33.7	14.1
12 mil vs. 16 mil	10.7	3.36
16 mil vs. 20 mil	11.0	3.19

*averaged over the drive phase

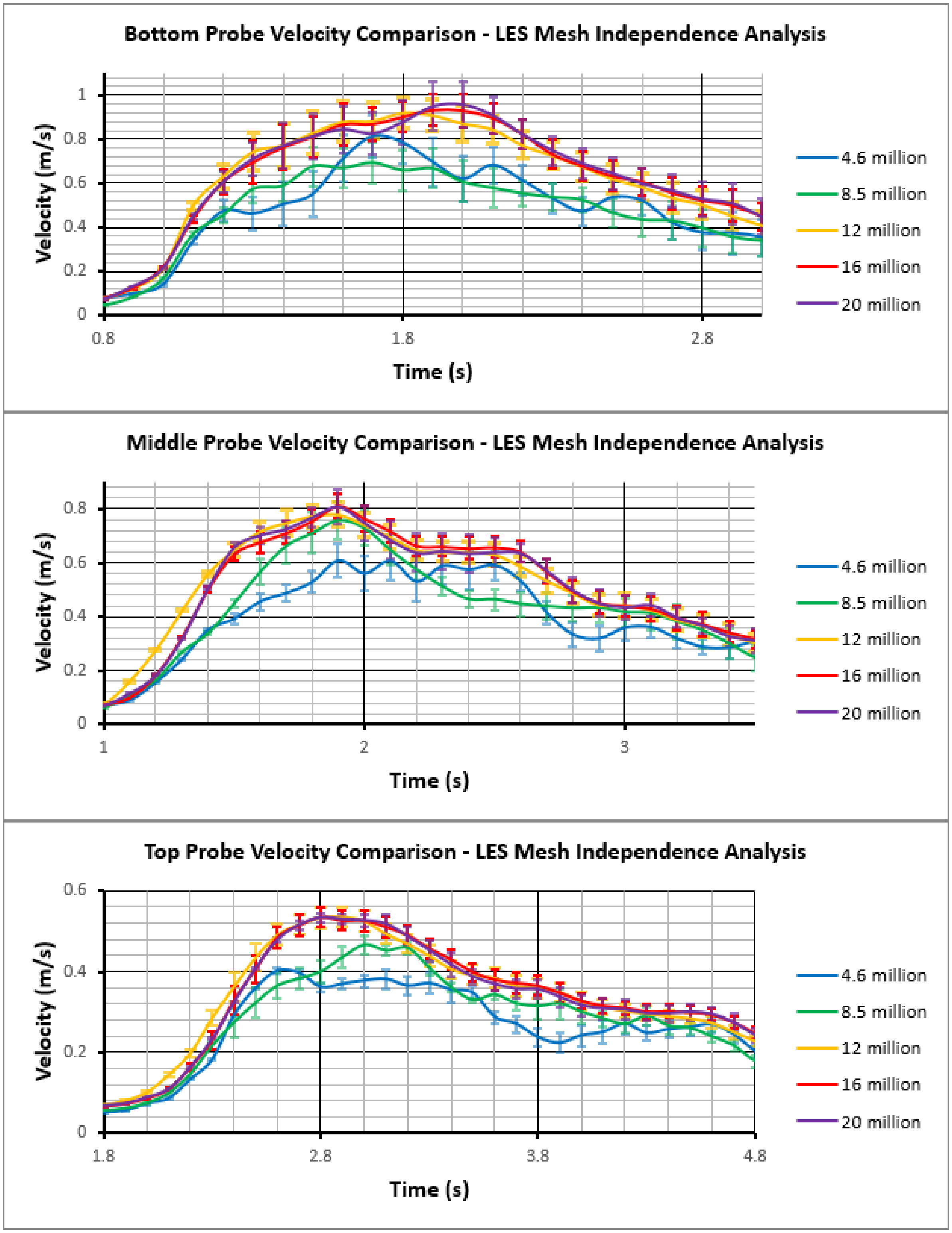

Figure 36. Ensemble Averaged Vertical velocity predictions vs. Time at the three (bottom, middle, and top) EM probe locations of Figure 12. Five curves represent data for mesh levels of 4.6, 8.5, 12, 16, and 20 million cells. Convergence behavior is identified at the 12 million cells level.

4.3. Lattice Boltzmann Model (LBM) Development

4.3.1. Statistical Analysis

The simulation data produced by the LBM model is subjected to the statistical analysis procedure described in Section 4.2.1. The cycle resolved data were processed to produce an average with 95% confidence intervals for each discrete time within the cycle. The PJM cycles were repeatedly simulated while the confidence intervals were tracked. Figure 37 compares the intervals calculated with 40, 60, 80, and 100 cycles. The fluctuations in the curves converge at 80 cycles. Figure 38 depicts 2D velocity data in the vessel's vertical midplane for several number of cycles and shows similar behavior. Because the difference in confidence intervals between 80 and 100 cycles was only 2.89% on average, it was determined that 80 cycles were sufficient to generate statistically reasonable results.

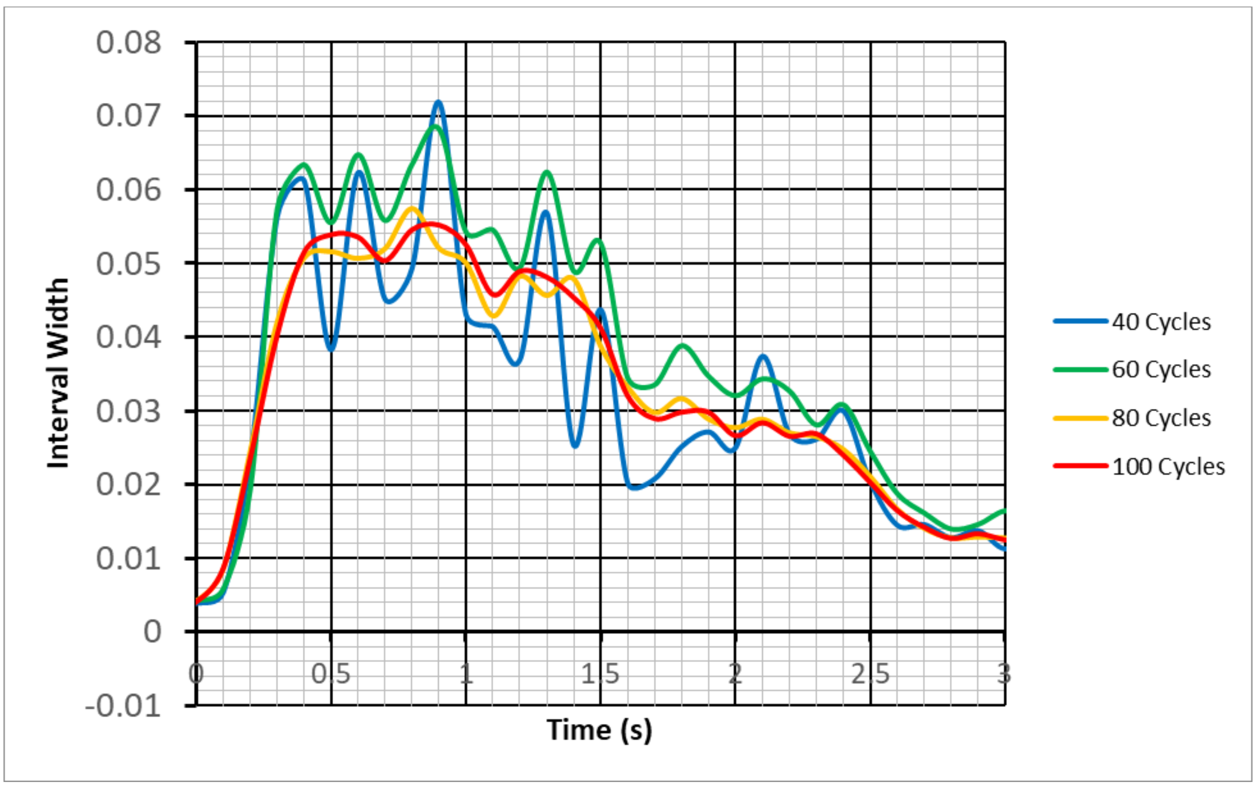

Figure 37. LBM model bottom probe velocity confidence interval comparison among 40, 60, 80, and 100 cycles. The values converge as the sample size grows.

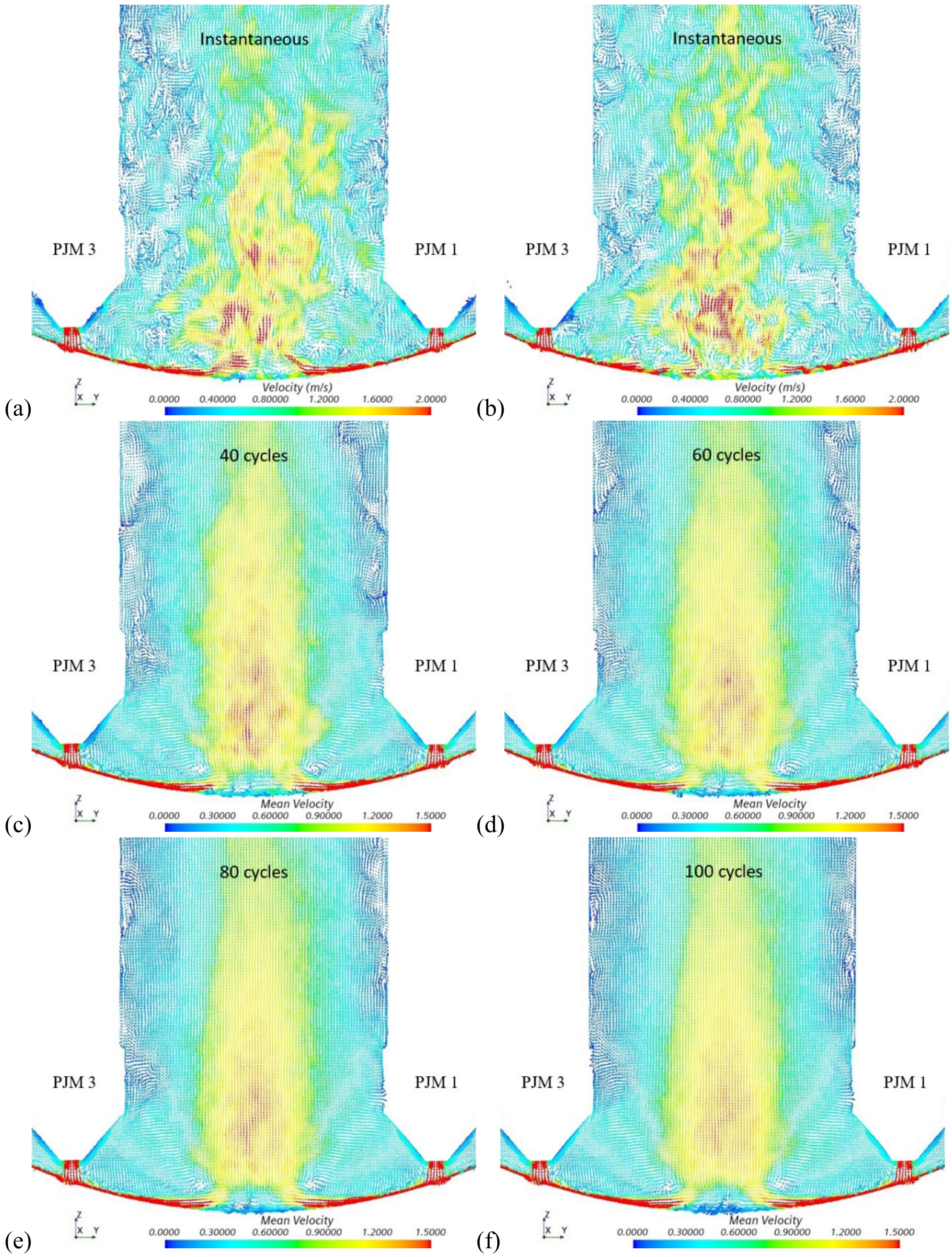

Figure 38. Flow vector field plots on a vertical cross-sectional plane at the end of the drive phase. Top two (a and b) show instantaneous flow fields at 10th and 20th cycles. Bottom four (c through f) are averaged flow fields with varying number of sample size: 40, 60, 80 and 100 cycles. Scenario 1, UPP.

4.3.2. Lattice Structure Independence

LBM is frequently referred to as a mesh-free process because it generates lattice points within fluid domains automatically. The only input required is a length scale that specifies the spacing between adjacent lattice points. In this work, the distance is applied rigidly, resulting in a homogeneous grid in the Cartesian coordinate system. In this configuration, there are no surface tessellations or meshes to represent boundaries. The lattice algorithm simply detects the lack of adjacent lattice points and applies boundary conditions. While this may be advantageous in some geometries and applications, it potentially is a significant shortcoming for a system like the PJM mixed vessel, where both time and length scales vary significantly within the fluid domain. For example, the model required 9 million evenly spaced lattice points throughout the vessel just to recognize and generate flows at the nozzles.

Four grid levels with 9.1, 12, 16, and 20 million lattice points were generated for the LBM model's lattice structure independence study. Figure 39 compares the simulation vertical velocity data at the probe locations collected from the four lattice structures. Table 8 shows the maximum and average velocity differences between successive lattice levels.

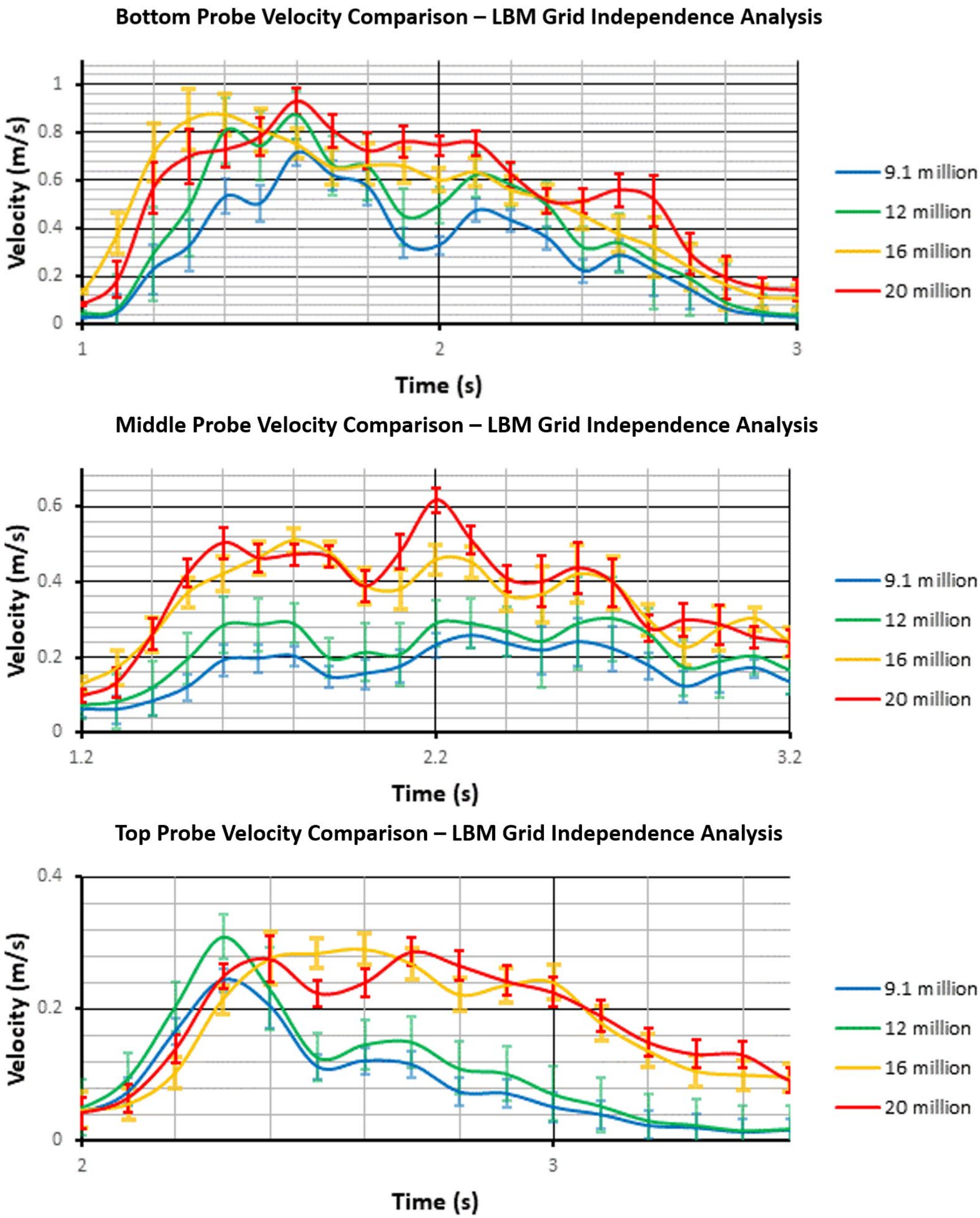

Figure 39. Vertical velocity predictions vs. Time at the three (bottom, middle, and top) EM probe locations (Figure 12). The four curves represent data from models with 9.1,12, 16, and 20 million lattice points. Convergence behavior is not identified. Scenario 1, UPP.

Table 8. Maximum and average percentage difference in vertical velocity measurements at the bottom EM probe locations (Figure 12). The differences are calculated between subsequent mesh levels to identify convergence. Scenario 1, UPP.

	Max. Difference (%)	Average Difference* (%)
9.1 mil vs 12 mil	33.94	23.98
12 mil vs. 16 mil	47.39	16.78
16 mil vs. 20 mil	37.65	16.73

**averaged over the drive phase*

Unfortunately, the LBM did not exhibit convergence behavior at any of the test grid levels. At 20 million lattice points, the average difference in confidence intervals remained significant at 24%, despite requiring 26% more simulation time per cycle than the mesh independent LES model.

The primary motivation for testing LBM for the PJM vessel was its claimed efficiency, especially when compared to LES. As a result, further LBM grid refinement would not be useful unless a zonal approach allowing coarsening of lattice spacing in zones away from the jet nozzle is pursued. While M-STAR provides local grid refinement, the interpolation computation was not optimized for parallelized computing scenarios, resulting in similar simulation time as refining the entire vessel, as shown in Table 18. As such, the final LBM model will use a uniformly spaced 16 million lattice point grid, which will require a runtime similar to the final LES model. The results in this configuration will show how LBM compares to LES when similar computational resources are available.

5. Model Validation Results

In this chapter, the predicted mean velocities at the EM velocity probe locations from the RANS, LES, and LBM simulation models are compared to the NETL experimental measurements. The chapter organization is based on the two PJM drive pressure profiles that were discussed in Section 3.2: the Uniform Pressure Profile (UPP) and the Individual Pressure Profile (IPP).

It is crucial to fully understand the pressure profiles' impact on simulation performance. Internal pressure data acquired by sensors installed near the compressor injectors (Figure 3) showed significant differences among the four PJMs during the NETL experimental tests. Figure 13 showed that the internal pressure of one PJM can be up to 30% greater than that of another PJM during drive phases. The behavior is consistently observed during all three operating scenarios. IPP accurately reflects each of the four PJM's measured pressure profile in the simulations, whereas UPP assumes the pressure difference is negligible and applies an averaged pressure profile (dashed line in Figure 13) to all four PJMs.

The UPP assumption has the potential to significantly improve model performance by reducing computational expense. The PJM vessel has two vertical planes of symmetry, resulting in four identical vessel quarters. In UPP, the boundary conditions in the four quadrants are identical, allowing 100 sets of data to be extracted from 25 cycles of LES or LBM computation. Because the symmetry conditions are not met in the IPP cases, all 100 cycles have to be completed. The mesh for the IPP cases also needs to be adjusted to account for the asymmetric central plume structures, according to the details provided in Section 5.2.1.

The UPP assumption must be validated for its potential cost reduction to be meaningful. To accomplish this, the UPP model is compared to and validated against the IPP model in Section 6.1.

Table 9. Simulation Cycles Performed for Each Case

	Scenario 1	**Scenario 2**	**Scenario 3**
RANS UPP	10 cycles	10 cycles	10 cycles
LES UPP	25 cycles	25 cycles	25 cycles
LBM UPP	25 cycles	X	X
RANS IPP	10 cycles	X	X
LES IPP	100 cycles	X	X
LBM IPP	100 cycles	X	X

As the study involves various simulation models and operating Scenarios, Table 9 summarizes the number of simulation cycles performed for each case. RANS cases were repeated 10 times to produce the final results because they required 8 cycles to eliminate the initial effects. UPP cases of LES and LBM were repeated 25 times to produce 100 sets of data, utilizing the four symmetric quadrants. IPP cases of LES and LBM were repeated 100 times because the symmetry conditions are not met (Section 3.2).

While all three PJM operating scenarios (listed in Table 2) are performed in the UPP cases of RANS and LES, only Scenario 1 is considered for LBM and for all IPP cases. This is due to the following two reasons:

Statistical analyses for LES and LBM (Sections 4.2.1 and 4.3.1) demonstrated accumulation of 100 cycles of data are required for each model. For the reasons stated above, the process would have necessitated significant computational resources for the additional IPP cases.

The following Sections (5.1.1 and 5.1.2) will show that the RANS and LES UPP case results differ only slightly among the three scenarios. Therefore, conclusions derived from one scenario are applicable more generally to all three.

Based on these observations, it was determined that running enough cycles for Scenario 1 is preferable to attempting all three scenarios and possibly ending up with insufficient cycled data.

5.1. Uniform Pressure Profile (UPP)

5.1.1. Unsteady RANS Simulations

Figure 40 compares the probe vertical velocity predicted from the unsteady RANS simulations (solid lines) to the NETL experimental data (dashed lines). The error bars represent the 95% confidence intervals for the experimental measurements.

In all three scenarios, the RANS data are significantly lower than the NETL measurements at the bottom probe and significantly higher at the middle and top probes. To quantify the comparison, the simulation velocity data are collected at the same frequency as the NETL measurements (10 hz) and percentage difference is calculated at every measurement point. Data with extremely low magnitude (less than 0.05 m/s) were marked as outliers to prevent data skewing. Finally, the maximum and average values were collected and listed in Table 10. The top and middle probes reported the highest and lowest differences, respectively.

*Table 10**.** Scenario 1 Maximum and average differences between the RANS UPP simulation predictions and NETL measurements at the three EM probe locations.*

	Bottom	**Middle**	**Top**
Max. Difference (%)	27.77	17.95	30.11
Average Difference (%)	18.62	12.60	27.73

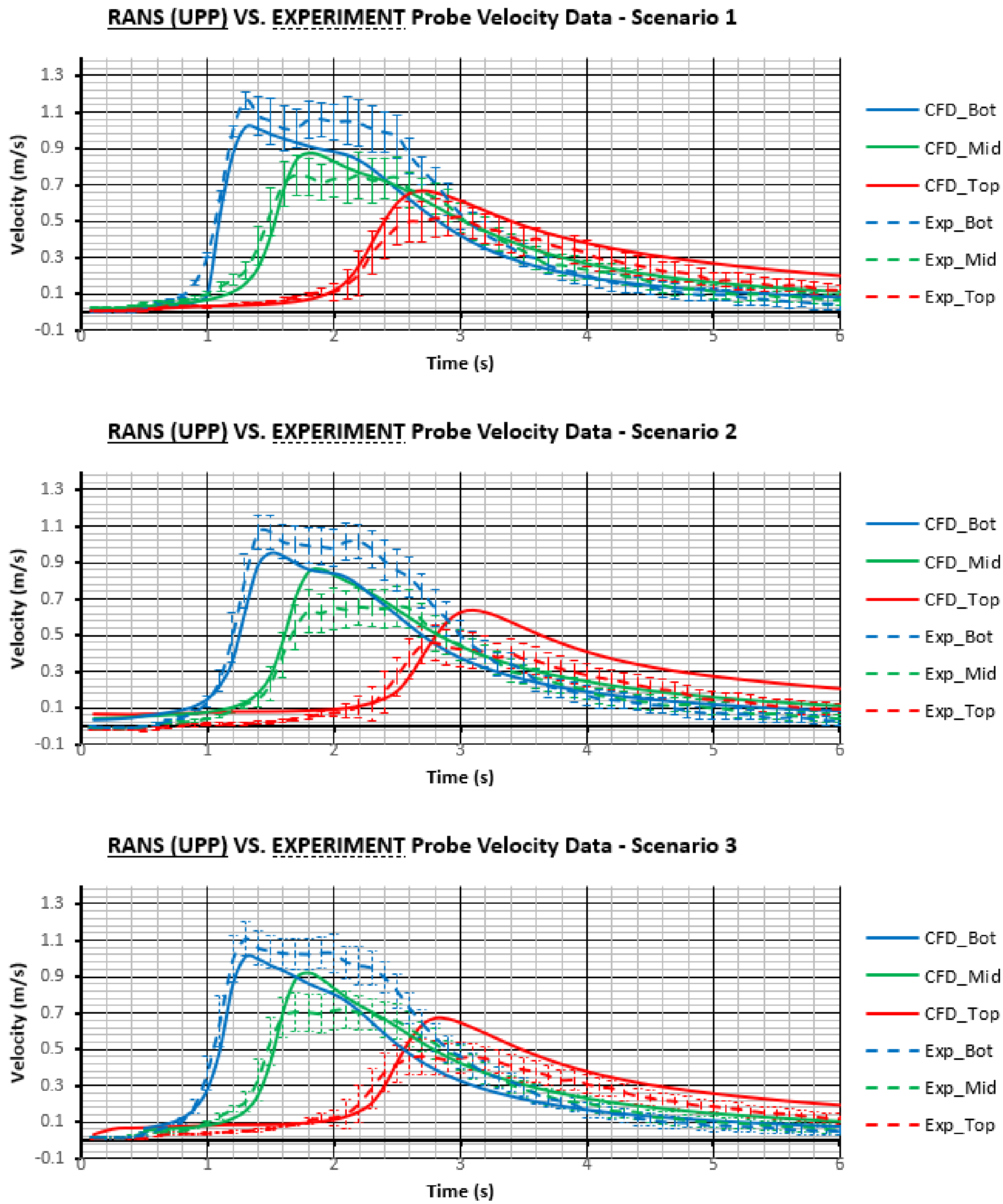

Figure 40. Probe vertical velocity predicted from RANS simulations (solid lines) and measured in NETL experiments (dashed lines). Error bars represent 95% confidence intervals. In all three scenarios, the simulation underestimates the velocity at the bottom probe while overestimating the velocity at the middle and top probes.

5.1.2. LES Simulations

Figure 41 compares the probe velocity data between LES simulations (solid lines) and NETL experiments (dashed lines). Because both curves in the figure are averaged values, they are accompanied by error bars indicating 95% confidence intervals.

In all three scenarios, the LES velocity predictions at the middle and top probes are mostly within the confidence intervals of the NETL measurements. Averaged over the entire cycle, the percentage errors at the middle and top probes were 8.7 % and 3.8 %, respectively.

The only challenge of the model is at the bottom probe. The model significantly underpredicts the probe velocity, reporting averaged percentage error of 23%. In all three scenarios, the simulation predictions are mostly outside the confidence interval from the NETL data, especially during the drive phase. The maximum and average differences between the LES and NETL velocity data at the three probes are listed in Table 11.

Table 11. Scenario 1 Maximum and average differences between the LES IPP simulation predictions and NETL measurements at the three EM probe locations.

	Bottom	**Middle**	**Top**
Max. Difference (%)	40.36	11.95	5.264
Average Difference (%)	23.23	8.716	3.839

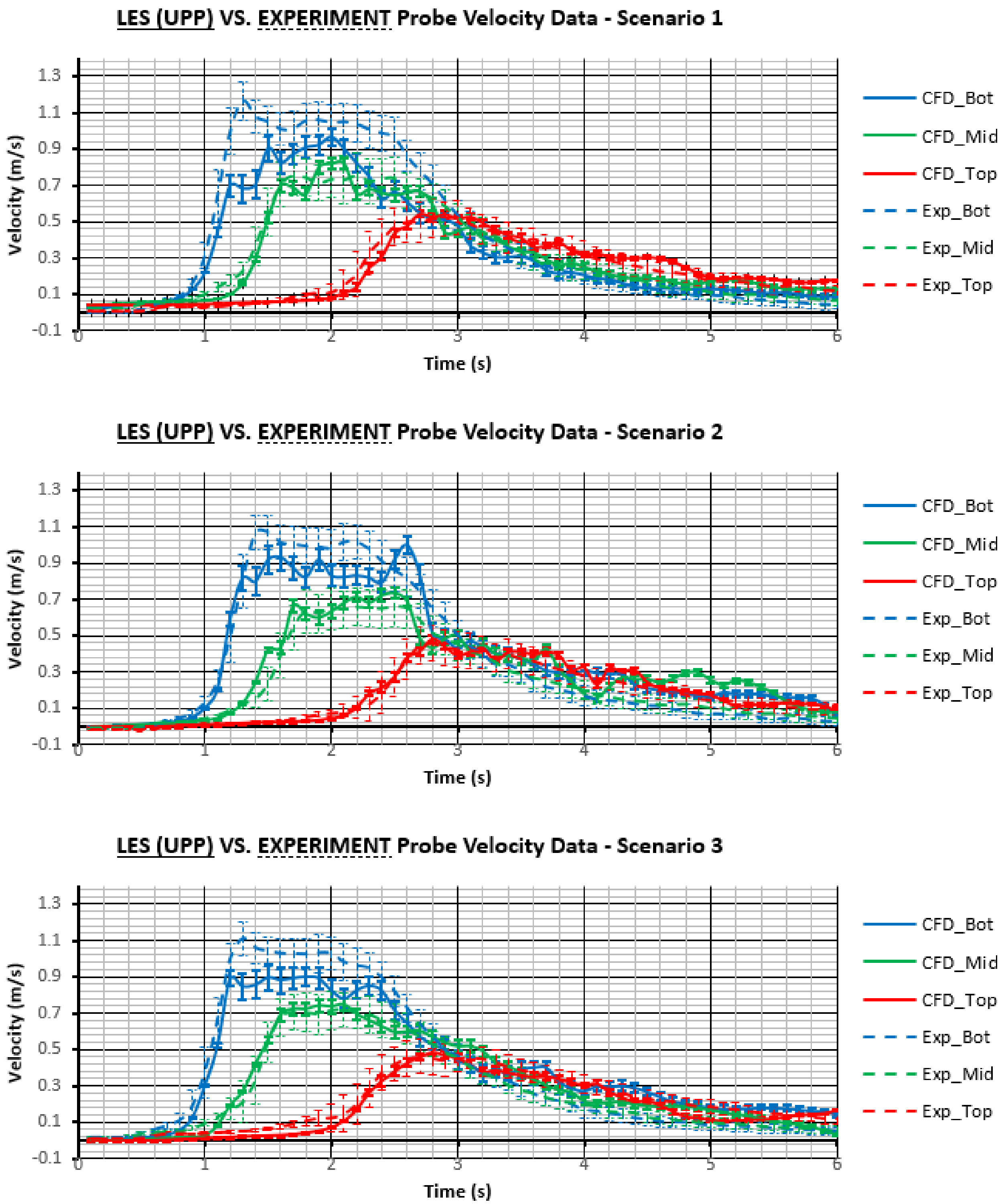

Figure 41. Probe vertical velocity predicted from LES simulations (solid lines) and measured in NETL experiments (dashed lines). Error bars represent 95% confidence intervals. The simulation accurately predicted the middle and top probe velocities in all three scenarios but failed to capture the bottom probe predictions within the experimental confidence intervals.

5.1.3. LBM Simulations

Figure 42 shows the probe velocity data from the LBM simulation (solid lines) and NETL experiments (dashed lines). The error bars represent the 95% confidence interval. Table 12 lists the maximum and average percent differences between the simulation measurements and experimental predictions.

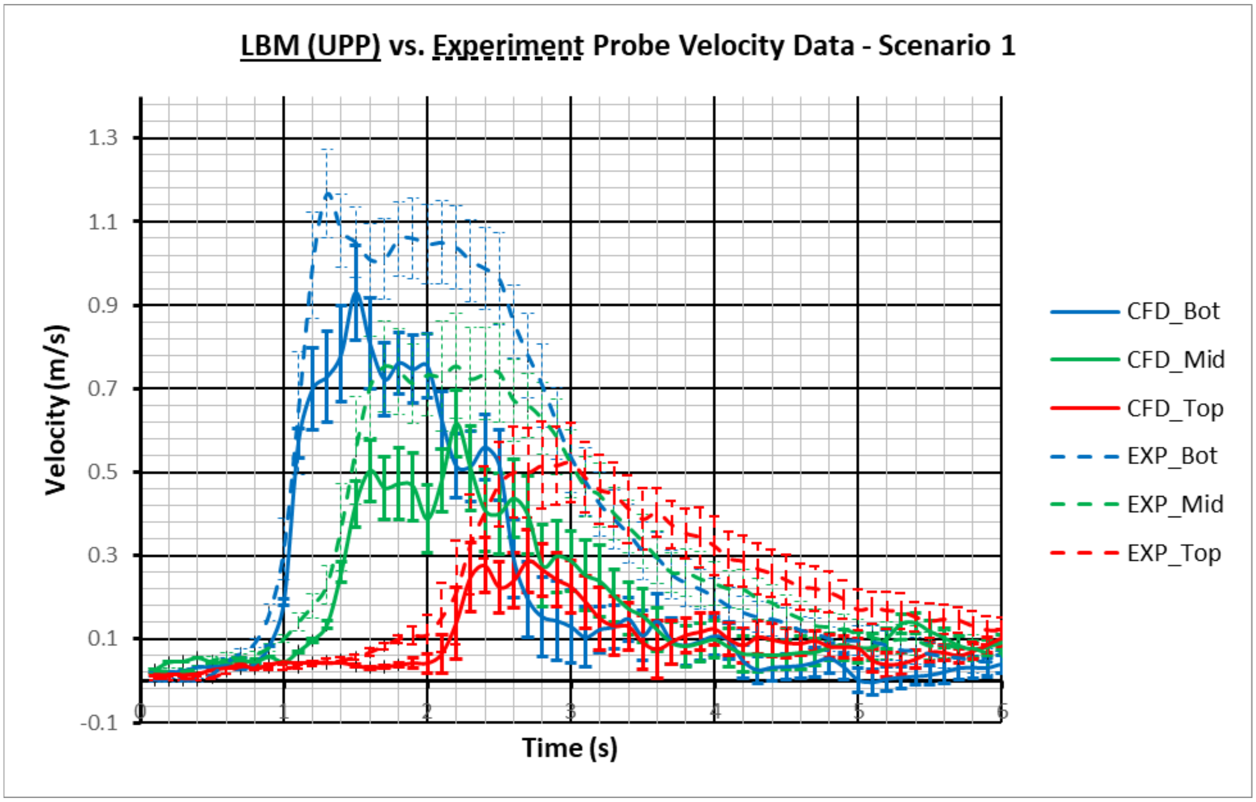

Figure 42. Probe vertical velocity predicted from LBM simulations (solid lines) and NETL experiments (dashed lines). Error bars represent 95% confidence intervals. The simulation model failed to predict probe velocities within the experimental confidence intervals at all three locations.

Table 12. Maximum and average differences between the LBM UPP simulation predictions and NETL measurements at the three EM probe locations.

	Bottom	Middle	Top
Max. Difference (%)	40.04	38.23	56.98
Average Difference (%)	33.14	37.53	51.03

The velocity predictions at all three probes are significantly lower than the NETL data. The poor comparison indicates a flaw in the simulation model, such as the spatial resolution, which did not achieve grid independence (Section 4.3.2). In-depth investigations of the model and analyses will be provided in Section 6.3.

5.2. Individual Pressure Profile (IPP)

5.2.1. Mesh Adjustment

With the differences in internal pressure (Figure 13) accurately reflected in the IPP simulations, the nozzle jet velocities of the four PJMs were significantly different from each other, altering the central plume structure. Figure 43 shows an example in which the PJM on the left has 30% lower internal pressure during drive than the one on the right (PJM 1 and 2 in Figure 13). Due to the significant tilt in the plume, the finely meshed zones developed for UPP needed to be spatially adjusted to ensure that the refined mesh regions track and capture the upwash plume. The red lines in the figure illustrates the mesh refinement zones for the UPP (left) and IPP (right) cases. The shift in mesh location made insignificant impact on the cell counts and mesh independence is again achieved with 12 million cells.

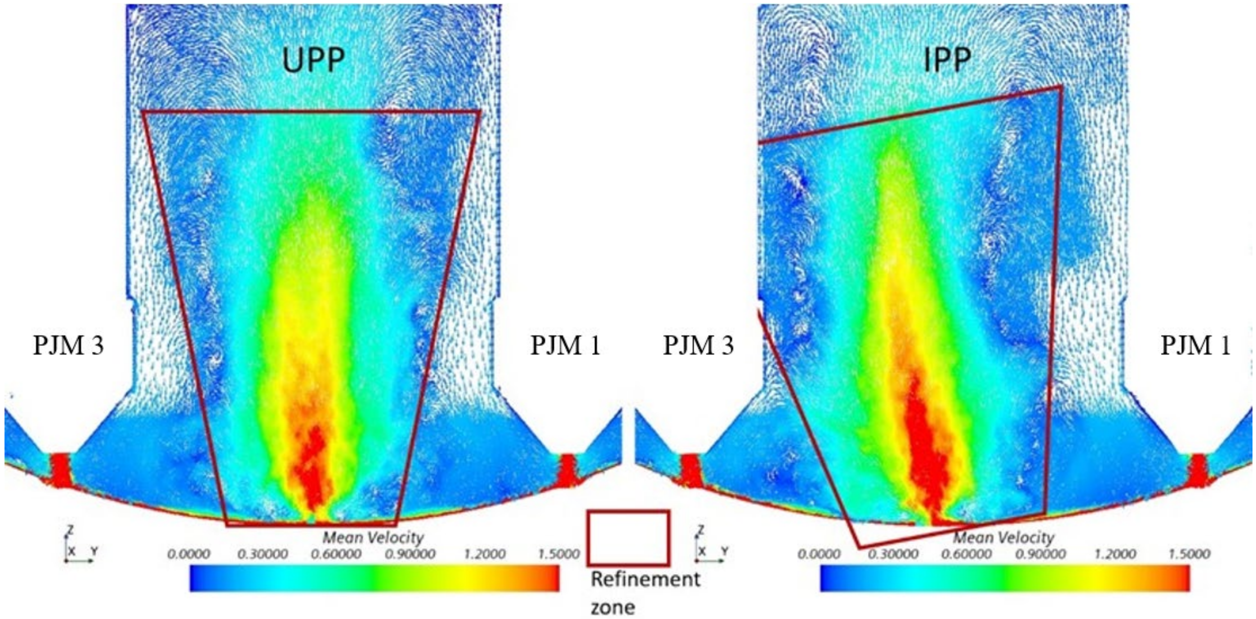

Figure 43. Mesh refinement zones are indicated by red lines in the UPP (left) and IPP (right) simulation cases. In the IPP case, the difference in PJM internal pressures caused the central plume to shift and tilt towards the PJM with lower nozzle velocity. Scenario 1, t = 2 (end of drive phase).

5.2.2. RANS

Figure 44 compares the probe velocity data from the RANS IPP case and NETL experimental data. The solid and dashed lines are CFD predictions and NETL data, respectively. The error bars indicate the 95% confidence intervals. Table 14 lists the maximum and average percentage differences at the three probe locations.

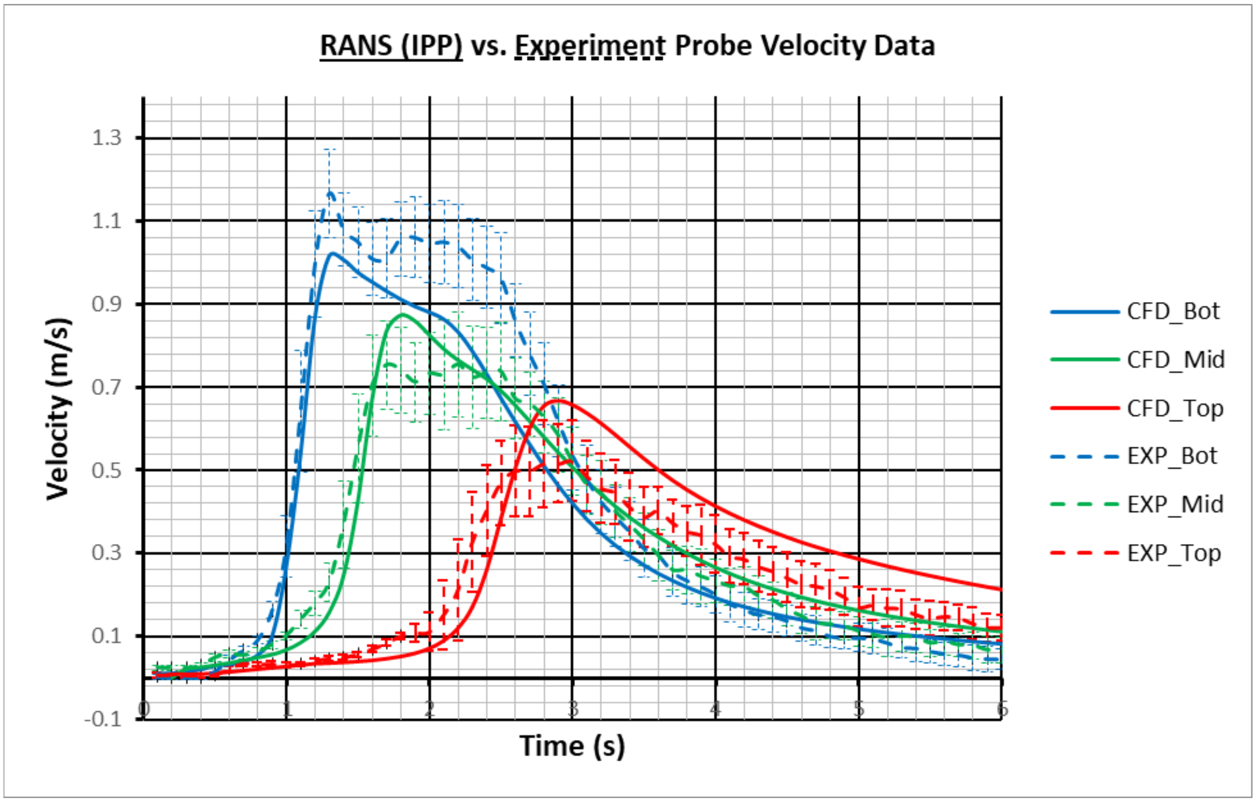

Figure 44. Probe vertical velocity predicted by RANS IPP simulations (solid lines) and measured by NETL experiments (dashed lines). The error bars are 95% confidence intervals. The bottom probe velocity is underestimated, while the middle and top probe velocities are overestimated.

Table 13. Maximum and average differences between the RANS IPP simulation predictions and NETL measurements at the three EM probe locations

	Bottom	Middle	Top
Max. Difference (%)	25.52	14.24	25.66
Average Difference (%)	16.02	11.77	24.19

While the IPP somewhat reduced the gap between RANS predictions and NETL measurements, the issues observed in the UPP case remain; the bottom probe velocity is under predicted, while the middle and top probe velocities are over predicted. The source of the significant error appears to be more fundamental than related to pressure profiles. Additional investigation and analyses are provided in Section 6.2.

5.2.3. LES Simulations

Figure 45 shows the probe velocity data predicted by the LES IPP simulation and measured by NETL experiments. The error bars indicate the 95% confidence interval. The comparison is quantified in Table 14, which lists the maximum and average percentage differences between the simulation and experimental data.

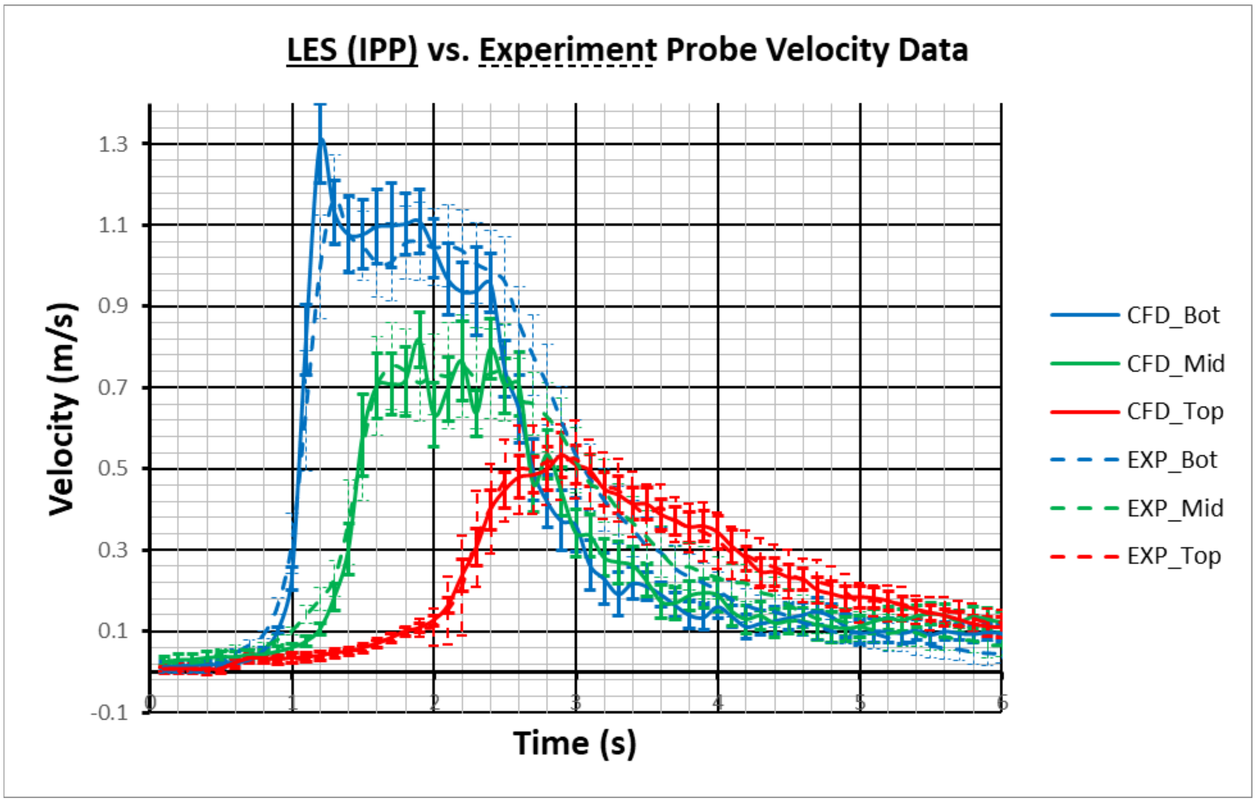

Figure 45. Probe vertical velocity predicted by LES IPP simulations (solid lines) and measured by NETL experiments (dashed lines). The error bars are 95% confidence intervals. Data from the three velocity probes are predicted within the experimental confidence intervals. Scenario 1.

Table 14. Maximum and average differences between the LES IPP simulation predictions and NETL measurements at the three EM probe locations. Scenario 1.

	Bottom	Middle	Top
Max. Difference (%)	9.731	11.77	4.931
Average Difference (%)	8.097	9.082	2.903

Using the IPP improved the LES bottom probe velocity prediction significantly. According to Table 14, its maximum and average percentage differences from NETL data are 9.1% and 8.1%, respectively. The predictions for the middle and top probes are similar to those for the UPP case.

With the improvement in bottom probe predictions, the LES IPP model successfully predicts at all three probe velocities within the experimental measurements' 95% confidence intervals. Section 6.1 includes analyses that show how adopting IPP only has a significant impact on the bottom probe.

5.2.4. LBM Simulations

Figure 46 compares the probe velocity data from the LBM IPP simulation (solid lines) and the NETL experimental measurements (dashed lines). The error bars indicate 95% confidence intervals. The data are compared and maximum and average percentage differences at the three probe locations are listed in Table 15.

Table 15. Maximum and average differences between the LBM IPP simulation predictions and NETL measurements at the three EM probe locations. Scenario 1.

	Bottom	Middle	Top
Maximum Difference (%)	53.66	65.05	57.96
Average Difference (%)	28.80	35.34	54.78

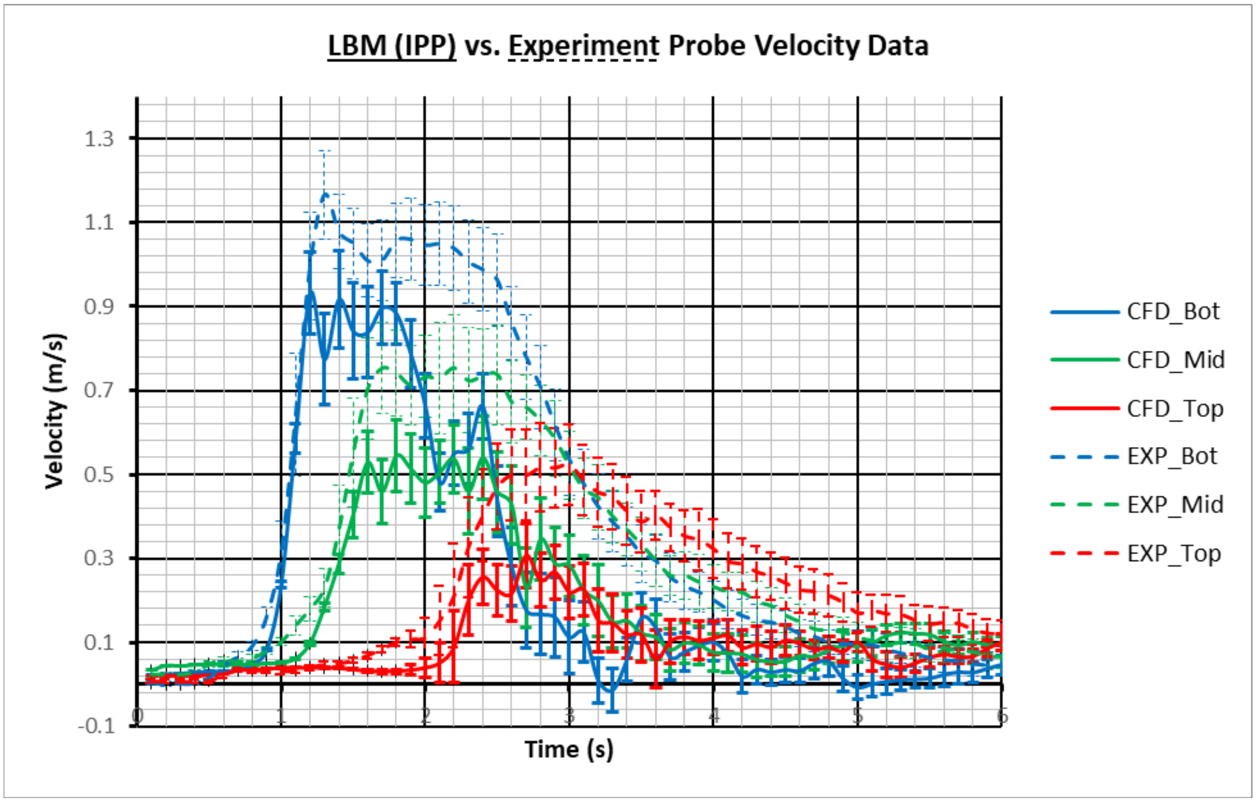

Figure 46. Probe vertical velocity predicted by LBM IPP simulations (solid lines) and measured by NETL experiments (dashed lines). The error bars are 95% confidence intervals. The simulation model fails to predict probe velocities within the experimental confidence intervals at all three locations. Scenario 1.

The LBM model's IPP case produced similar velocity data to the UPP case; however, the predictions are significantly lower than the experimental measurements at all three probe locations. The maximum differences at all three probes exceeding 50% indicates a fundamental problem with the model set up, which will be investigated in Section 6.3.

5.3. Simulation Time

Computation time is often one of the most important factors in practical simulation projects. This section compares various factors that affect the computational costs of the RANS, LES, and LBM simulation models. Table 16 shows the simulation time and contributing factors for each model.

Table 16. Simulation Performance Comparison – LES, RANS, and LBM

	LES	**RANS**	**LBM**
Cell Count	12 mil	1.8 mil	16 mil
Drive Phase Timestep Size	1.0 ms	5.0 ms	0.27 ms
Min. Cell Size	0.14 mm	0.34 mm	3.8 mm
Max. Cell Size	12 mm	37 mm	3.8 mm
CPU Time per Cycle*	~ 220 hr	~ 36 hr	~ 230 hr
Normalized CPU Time	6.1	1	6.9

*per node, Xeon(R) Gold 6248 with 40 cores

The RANS model achieved mesh independence with only 1.8 million cells and operated stably with larger time step sizes. As a result, the model achieved the highest efficiency with the shortest simulation time per cycle, although it failed to match the NETL experimental data.

The LES model successfully matched the NETL data at a cost. To resolve the majority of the key eddies and achieve a low M value, significantly smaller cells and time step sizes were required (eq. (31). As a result, the model required 6.1 times more calculation time per cycle when compared to the RANS model.

As discussed in 4.3.2, the LBM model did not achieve grid independence at 20 million lattice points, and further refinement was not pursued due to its significant computational cost and/or a need to develop a zonal model for lattice point spacing. The lattice structure with 16 million points was chosen as the final model as it produced equivalent calculation time to the final LES model. Despite having a higher cell (lattice point) count than the LES model, the LBM model has a 27 times larger minimum grid size due to its homogeneous grid structure.

From a numerical standpoint, the results partially demonstrate LBM's claimed efficiency; compared to LES, LBM achieved similar simulation runtime (4.5% longer) with a higher (32%) cell count and significantly smaller (73%) time step size. While the simulations in this study are run on CPU nodes, simulation methods that use CPU and/or GPU clusters are being actively developed and are currently in use. Because LBM is well optimized for parallelization, there is potential that the model will outperform RANS and LES in the future.

5.4. Summary of Findings

Using IPP instead of UPP made a significant difference for the LES model. LES IPP is the only simulation case that successfully matched the NETL measurements within the 95% confidence interval at all three velocity probe locations.

Pressure profiles did not make significant changes to the RANS results. In both pressure profile cases, the velocity data were underpredicted at the bottom probe location and overpredicted at the middle and top probe locations.

The pressure profiles did not make significant differences on LBM model's results. The model significantly underpredicted velocities at all three probes compared to the NETL measurements.

While RANS shows significant accuracy issues, there may be usage for RANS as it has significant performance advantage. LBM, on the other hand, may not be recommended as the model requires slightly more computation resources than the LES model. This will be covered in greater detail in Chapter 6, along with additional fluid flow and turbulence comparison analyses of the LES, RANS, and LBM models.

6. Simulation Model Analysis and Utilization

The simulation results were compared to the NETL velocity probe measurements in Chapter 5. Because the laboratory experiment evaluated the PJM vessel's performance using vertical velocities at three point locations, only equivalent predictions from the simulation models were used for validation. The flow field predictions at the EM probe locations are only a small part of the models' fully transient and 3D simulation results. In this chapter, the flow fields and turbulence metrics (turbulent kinetic energy, turbulence dissipation rate, and turbulence production rate) predicted by the simulation models are analyzed to explain why some of the models perform better in matching the experimental measurements. The simulation models are then utilized to demonstrate the PJM vessel’s main flow field characteristics, which can be challenging to achieve with experimental data alone.

In Section 6.1, the 2D velocity vector fields for the Uniform Pressure Profile (UPP) and Individual Pressure Profile (IPP) cases are examined to explain how the two pressure profiles cause significant differences in the probe location velocities (shown in Figure 43).

In Sections 6.2 and 6.3, the velocity fields and turbulence metrics data from the RANS, LES, and LBM simulation models are compared to explain the differences in their velocity probe predictions. Turbulent kinetic energy, predicted by the simulation models, is displayed and analyzed in various regions with close-up and overall views. Equivalent plots showing turbulence dissipation rate and turbulence production rate are provided in the Appendix and will be referred to, as discussed. Because the LES model performed the best in simulating the probe velocities from the NETL data, it was used as a benchmark to identify factors that potentially introduced errors in the other two simulation models.

Section 6.4 describes the flow features and phenomena illustrated by animations in the PowerPoint file provided with this manuscript. The animations show the critical flow patterns from a variety of viewpoints, including close-ups of the nozzle, dish-bottom, upwash-plume, and an overall view that includes the top and peripheral regions.

As was explained in Table 9, only Scenario 1 is utilized for IPP simulations. As such, all simulation results shown in this Chapter are from Scenario 1.

6.1. Uniform Pressure Profile (UPP) vs. Individual Pressure Profile (IPP) for the LES Model

As discussed in Sections 5.2.2, and 5.2.3, the choice of pressure profiles (introduced in 3.2 with Figure 13) did not make significant differences in the simulation predictions for the RANS and LBM models. Therefore, the section will focus on how the pressure profiles may influence the LES model's predictions. Figure 47 shows velocity vectors from the LES UPP (left) and IPP (right) cases. The plots are displayed on a vertical plane (introduced in Figure 28), which spans the vessel and passes through the centerline of the vessel and two opposing PJMs. The vector fields are generated by averaging the instantaneous velocity predictions from 100 cycles at the end of the drive phase. The term "ensemble averaged" or "cycle resolved" mean velocity will be used to refer to data averaged in this manner. The red dots indicate the locations of the bottom, mid and top EM velocity probes.

The plots show that, as was mentioned in Section 5.2.1, the difference in PJM internal pressures and resulting nozzle velocities shifted the orientation of the central upwash plume to no longer coincide with the vessel axis. While the overall structure of the plume is maintained, the shift alters the velocity probe's relative positions. In the UPP case, none of the three probes measures the maximum velocity along the plume centerline due to their off-center positions. In the IPP case, the tilted plume allows the bottom probe to measure higher velocity at the central region of the plume, while placing the middle probe on the other side of the central region. At the top probe location, the plume structure is diffused, and the velocity gradient across the horizontal plane is not as steep.

Scenario 1, LES, UPP vs. IPP, Ensemble Average, End of drive phase (t = 1.6 seconds)

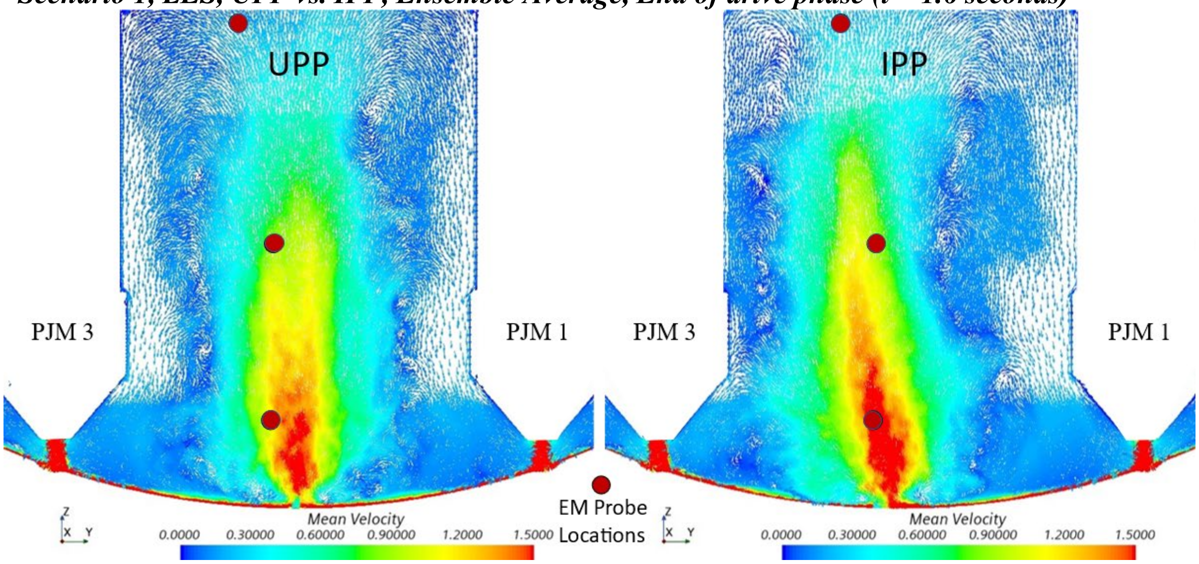

Figure 47. Velocity fields (ensemble average) at the end of a drive phase of LES UPP (left) and LES IPP (right) cases. Red dots indicate EM velocity probe locations. The shifted structure of the upwash plume alters the positions of the EM velocity probes, relative to the upwash plume centerline.

The analysis explains how the pressure profiles significantly alter the predicted velocity at the bottom probe while making minimal impacts on velocities at the middle and top probe locations. It also demonstrates the importance of accurately controlling internal pressures of each PJM, as the measurements at the probe locations can be significantly impacted by a slight shift in the plume orientation. Knowing the shape of the upwash plume is central to evaluating the device's overall mixing performance [4]. If synchronization of the PJMs' internal pressure is not possible, experimentation should not be limited to velocity readings at a few points. It is recommended to monitor 2D velocity fields using methods such as Particle Image Velocimetry (PIV) to understand plume shapes, orientations, and velocities, which will depict the full impact of any pressure imbalances and provide far more accurate description of mixing phenomena occurring within the vessel.

6.2. Comparison Analysis between LES and RANS Models

In the IPP results presented in Sections 5.2.2 (RANS) and 5.2.3 (LES), an observation was made which prevented the RANS model from accurately predicting velocities at the three EM probe locations: the velocity data were underpredicted at the bottom probe location, and overpredicted at the middle and top probe locations.

To analyze and contrast the behavior of the RANS and LES models, velocity data and turbulence metrics are presented on 2D plots for comparison. The key findings, which will be demonstrated below, are as follows:

- When compared to LES, RANS exaggerated the size and intensity of vortices in the bottom region near the PJM nozzles, overestimating turbulence production, kinetic energy, and dissipation rate in the bottom region.
- When compared to LES, RANS failed to capture numerous vortices in the middle and top regions, underestimating turbulence production, kinetic energy, and dissipation rate in the area.
- RANS did not capture any of the vortices present in the LES results during the PJM suction phase. As a result, turbulence production, kinetic energy, and dissipation rate are all underestimated in the entire region for RANS when compared to LES.

These points will be discussed in detail to explain why the RANS model struggles to match the NETL probe measurements and to contrast predicted turbulence quantities. The velocity field and predicted vortex structures are discussed in Section 6.2.1 and turbulence metrics are examined in Section 6.2.2.

As one of the objectives is to understand why the models perform differently predicting the NETL experimental data, the analysis is carried out on the IPP cases that showed the best match (Section 5.2.3). As stated in Chapter 5, the IPP cases were only run for Scenario 1 (details of three PJM Operating Scenarios are provided in Table 9). Therefore, all of the results in this section are for the IPP case of Scenario 1. The IPP pressure profiles are shown in Figure 13.

6.2.1. Flow Characteristic Comparisons Focusing on Vortices

Figure 48 shows cycle resolved velocity vector plots on a vertical cross-sectional plane for the LES (left) and RANS (right) IPP cases at the end of the drive phase (t = 1.6 seconds). Cycle resolved velocity data displayed on the LES plot are ensemble averaged over 100 cycles.

In the RANS plot, only two large vortices are visible next to the plume near the dish bottom (marked by black circles). The vortices are significant in size, spanning from the central plume to the nozzle locations. In LES, on the other hand, distinct smaller vortices are visible. The exaggerated vortices in RANS have a significant impact on the central plume. They produce strong flows returning from the plume toward the nozzles. In both the LES and RANS results, the area is denoted by black ovals. The flows in RANS drain energy from the plume and weaken vertical flow in the bottom region, which contributes to the lower velocity predicted at the bottom probe location shown in Section 5.2.2.

Scenario 1, LES vs. RANS, IPP, Ensemble Average, End of drive phase (t = 1.6 seconds)

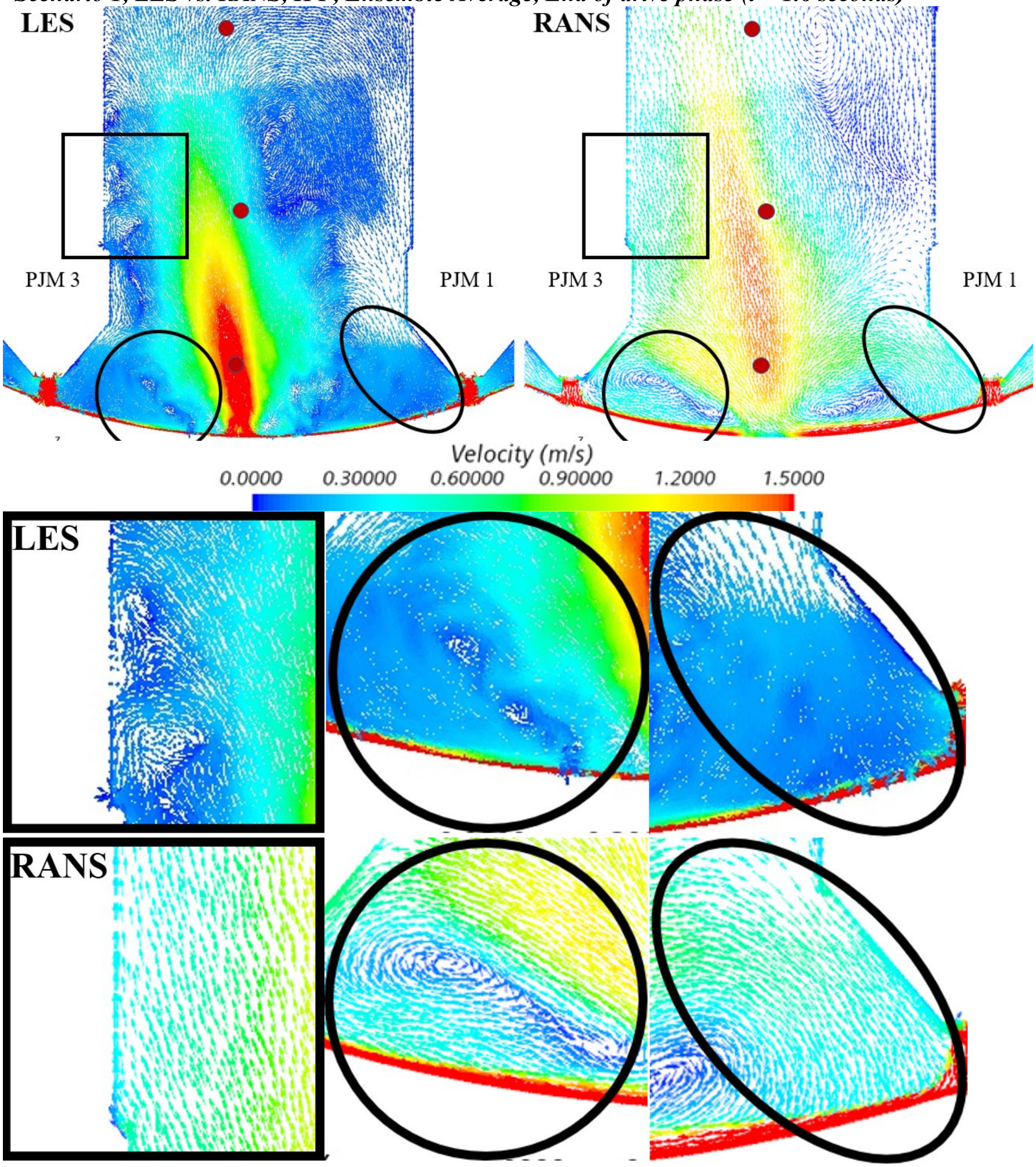

Figure 48. Velocity fields of LES IPP (left) and RANS IPP (right) simulations at the end of a drive phase. Vortices are identified by black rectangles (left), circles (middle), and ovals (right). The squared and circled regions show vortices of various size that the RANS model fails to capture. The region marked by ovals show recirculation flows only predicted by the RANS model.

RANS exaggerated the size of vortices in the bottom region but did not capture any in the middle or top regions. LES, on the other hand, predicts numerous vortices, upon ensemble averaging, along the entire height of the plume (marked by black squares). Due to the lack of vortices, the central plume in RANS experiences artificially low resistance, and carries stronger flow to the middle and top regions. This explains why the RANS model overestimates velocity data at the middle and top probe locations, as shown in Figure 44.

The differences between the LES and RANS models may appear to be due to mesh resolutions, but mesh independence studies (Sections 4.1.1 and 4.2.2) have ruled this out; additional refinements on the mesh of the RANS and LES models did not make improvements.

The difference therefore appears to originate from the formulations of the models. Unsteady RANS, as discussed in Section 2.2.1, only predicts time averaged quantities and uses mean strain rates to model turbulence. While this is effective in many applications, it has several known limitations in predicting highly transient and rotational flows with steep velocity gradients [26], [11], [10]. The RANS model produces inaccurate results because all of these elements are present in the PJM vessel flow field. Unsteady RANS assumes that the macro time scale of turbulence is small compared to the process time scale. This may not be the case within the discharge jet and upwash plume.

In the following section, the limitations of the RANS model, relative to LES, are investigated further by analyzing its predicted turbulence metrics in comparison to the LES model.

6.2.2. Turbulence Comparison Analysis

In this section, the turbulent kinetic energy (TKE), turbulence dissipation rate (TDR), and turbulence production rate (TPR) of the LES and RANS results are examined. The RANS model predicts the turbulence values based on the numerical process described in Section 2.2.1. For the LES model, statistical analysis was performed utilizing simulation data accumulated by repeating 100 PJM mixing cycles of Scenario 1 to produce the turbulence metrics. Section 6.2.2.1 examines how the data of the two models differ on various 2D planes at the end of the drive phase, while Section 6.2.2.2 compares how the volumetric average of the turbulence metrics change over time throughout the drive, vent, and suction phases for the two models.

6.2.2.1. *2D Analysis*

***Scenario 1, LES vs. RANS, IPP, End of drive phase (t = 1.6 seconds)**

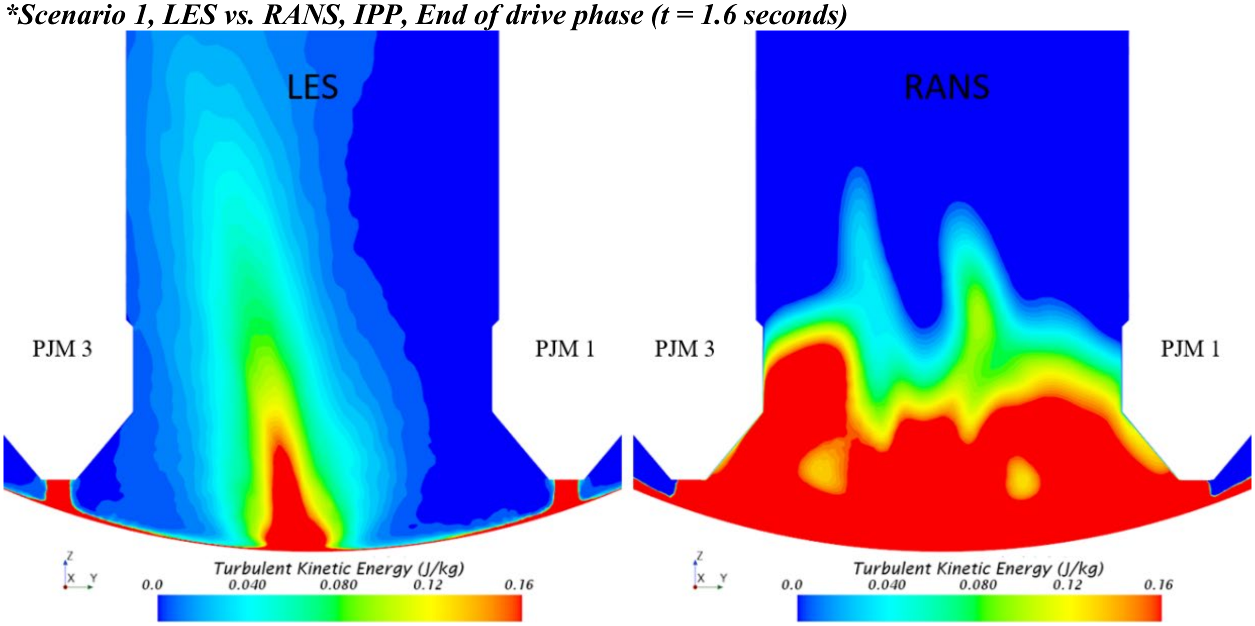

Figure 49. Turbulence Kinetic Energy (TKE) scalar contour plots from LES (left) and RANS (right). LES shows high values around the central upwash plume. RANS shows high values around the bottom vortices.

Figure 49 compares TKE for the LES (left) and RANS (right) cases at the end of a drive phase. The plots are on a vertical plane which spans the vessel and passes through the centerline of the vessel and two opposing PJMs (Figure 8). In the LES result, the shape of the central plume can be seen as the high TKE values are mainly caused by velocity fluctuations due to the plume meandering over time. Meaningful TKE values are also seen around the plume in the middle and top regions which are caused by small vortices that are captured by the LES model (black squares in Figure 48).

The TKE values in the RANS plot are dominated by the two large vortices in the bottom region that were identified in black circles in Figure 48. As was discussed in Section 2.2.1, RANS relies on mean strain rates to model TKE, and it often exaggerates turbulence metrics around the model's predicted vortex locations [27]. On the other hand, the model severely underpredicts TKE in the middle and top regions of the central upwash plume compared to LES. As a result, it is difficult to determine the location of the plume based on the TKE results of the RANS model. As plume meandering is commonly observed and expected in turbulence flows [28], a complete lack of the structure's influence on the turbulence plot does not seem realistic.

The unrealistic TKE results in RANS appears to be related to the model's failure to capture any of the vortices identified by LES in the middle and top regions (black squares in Figure 48). Even though velocities are high in the middle and top plume core regions, RANS predicts low TKE values in the area because the flows are facing the same direction with low velocity gradients.

Figure 49 demonstrated significant differences in TKE between the LES and RANS models at the bottom, middle, and top regions. A negative correlation can be established by observing the velocity predictions at the probe locations and TKE results of LES and RANS simulation models. When compared to LES, RANS predicted higher TKE and lower velocity flows in the bottom region and lower TKE and higher velocity flows in the middle to top regions. The correlation could be attributed to turbulence interacting with mean flows. Exaggerated turbulence in the bottom region, for example, could indicate that energies are artificially drained from the mean flow, contributing to the lower velocity flows predicted at the bottom probe location.

To examine the hypothesis further, three horizontal planes are created, which are illustrated in Figure 50 and described in Table 17. The P1, P2, and P3 planes are positioned upstream (lower in the vessel) of the bottom, middle, and top probes, respectively. The analysis will look for any associations between the turbulence metrics on each plane and the velocity predictions at the downstream probe.

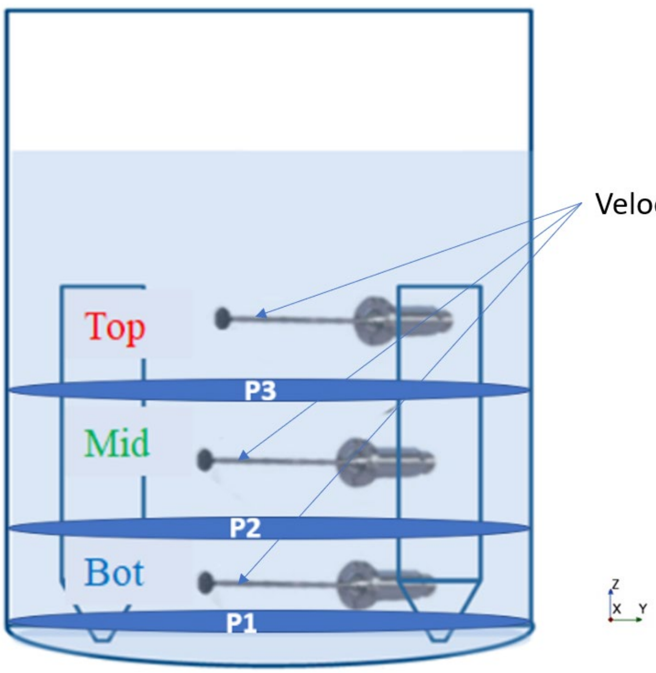

Figure 50. Horizontal planes to display turbulence metrics upstream of the EM Probe locations. P1, P2, and P3 planes are located upstream (lower) of bottom, middle, and top probes, respectively, at positions given in Table 17.

Table 17. Locations of P1, P2, and P3 planes. The planes are designed to display upwash plume prediction upstream of the three EM velocity probes.

	P1	**P2**	**P3**
Location	z = 0.085 m	z = 0.27 m	z = 0.49 m
Description	Halfway between the dead center dish bottom and the bottom probe location.	Halfway between the bottom and middle velocity probe locations.	Halfway between the middle and top velocity probe locations.

Figure 51 and Figure 52 display contour plots of TKE and TDR data, respectively. The results from LES are displayed on the left column and RANS on the right. They are displayed on P1 (top row), P2 (middle row), and P3 (bottom row). As was noted in Figure 49, RANS predicts significantly higher TKE values in the bottom region (on P1). The plume core region of the LES predictions has some high TKE values as well, but the overall values are much lower than the RANS results.

Scenario 1, LES vs. RANS, IPP, End of drive phase (t = 1.6 seconds).

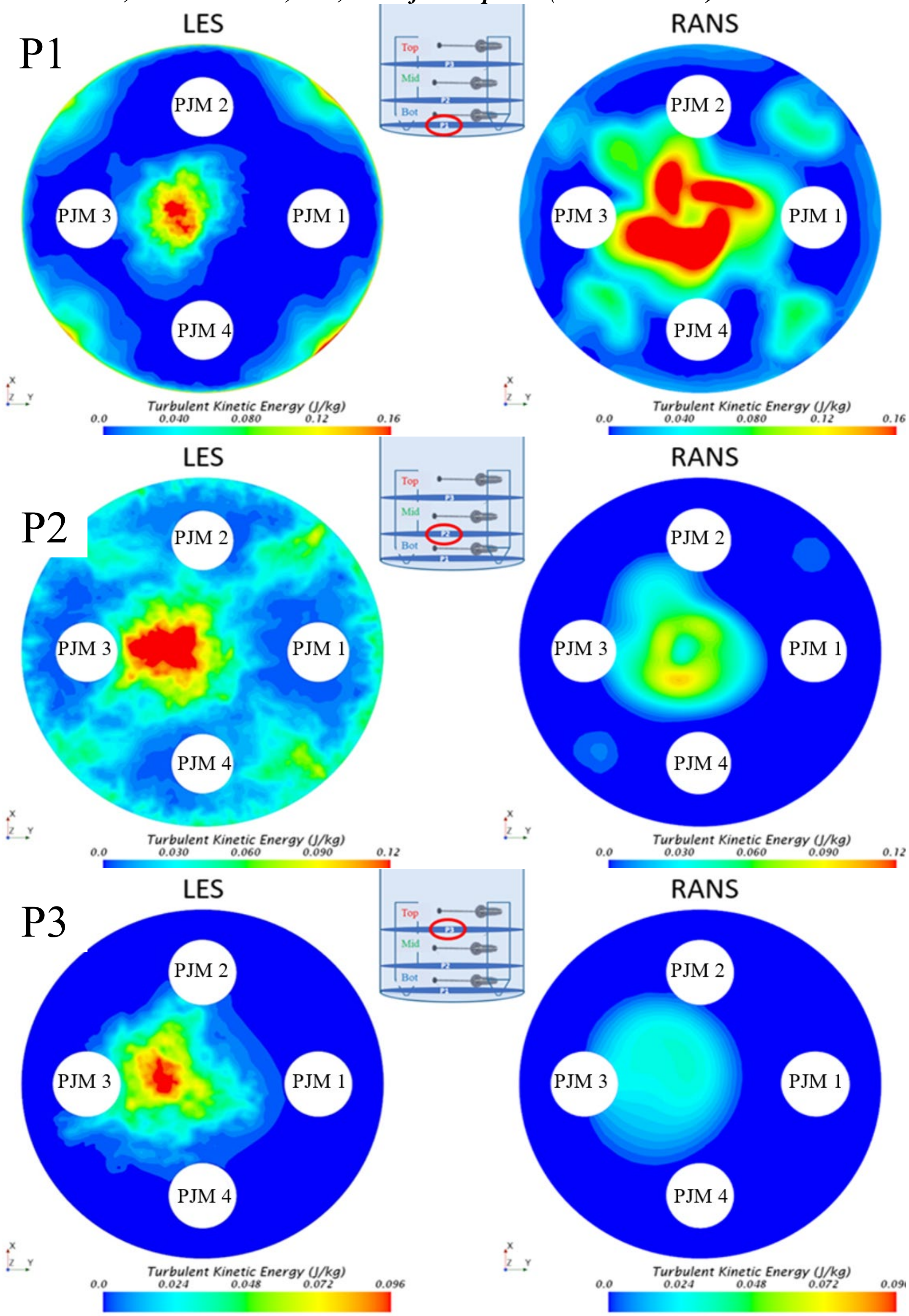

Figure 51. Turbulence Kinetic Energy from LES (left) and RANS (right) IPP cases reported on P1 (top row), P2 (middle row), and P3 (bottom row). In comparison to LES, RANS produces higher TKE on P1 and lower TKE on P2 and P3.

The high TKE values predicted by RANS in the central area correlate with its higher TDR and turbulence production values, as shown on P1 in Figure 52. High turbulence production in RANS is also observed in Figure 82 in the Appendix. Significantly higher turbulence production and dissipation rate in RANS indicate that more energy is taken away from the mean fluid flows, directly upstream of the bottom probe, which can be a contributing factor for the RANS model to predict lower velocity at the bottom probe.

In the middle and upper regions, the comparison reverses. While the LES model continues to have high TKE (Figure 51), TDR (Figure 52) and turbulence production (Figure 82) in the core region on P2 and P3, the RANS model now has significantly lower values. This suggests that energy for the mean fluid flow in RANS is better conserved in the regions upstream of the middle and top probes, allowing the plume in RANS to carry higher velocity flows through the velocity probe locations.

The RANS model's poor performance in predicting turbulence metrics is consistent with other comparison studies between LES and RANS. Van Hooff et al. studied the accuracy of CFD simulations of turbulent cross-ventilation flows [12], Jaworski et al. compared CFD solutions for turbulence kinetic energy and dissipation rates for a liquid-liquid static mixer [29], Rhea et al. studied CFD models of a single-phase, impinging plane jet [30]. In all three studies, LES results matched the experimental data more accurately.

Scenario 1, LES vs. RANS, IPP, End of drive phase (t = 1.6 seconds)

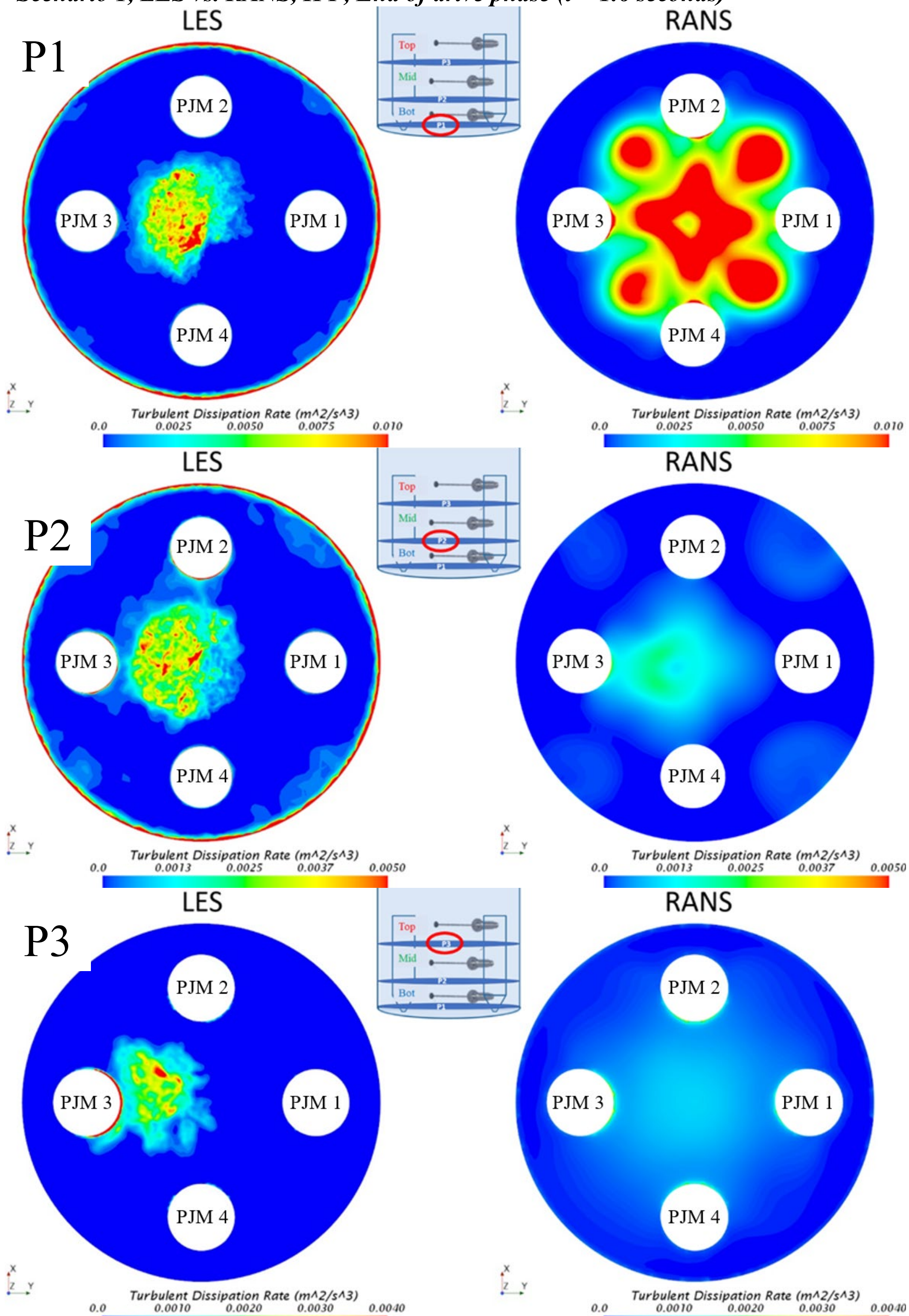

Figure 52. Turbulence Dissipation Rate from LES (left) and RANS (right) IPP cases reported on P1 (top row), P2 (middle row), and P3 (bottom row). In comparison to LES, RANS produces higher TKE on P1 and lower TKE on P2 and P3.

For a quantitative analysis of the turbulence data, a diagonal line from the center to the vessel wall is drawn on P1, P2, and P3 planes, as shown with a red dotted line in Figure 53. Then, the turbulence data are collected along the line and plotted against the radial distance, as shown in Figure 54. The solid and dashed curves represent the LES and RANS predictions, respectively.

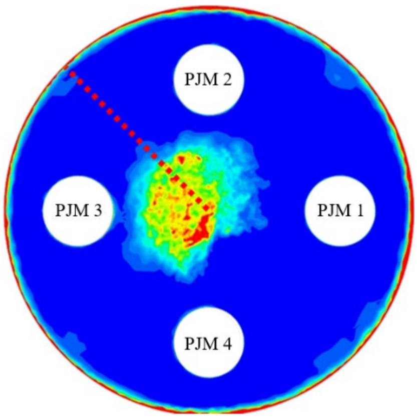

Figure 53. A Line for data collections and plotting is displayed on P1 in red. Identical lines were drawn on P2 and P3 to produce the data shown in Figure 54.

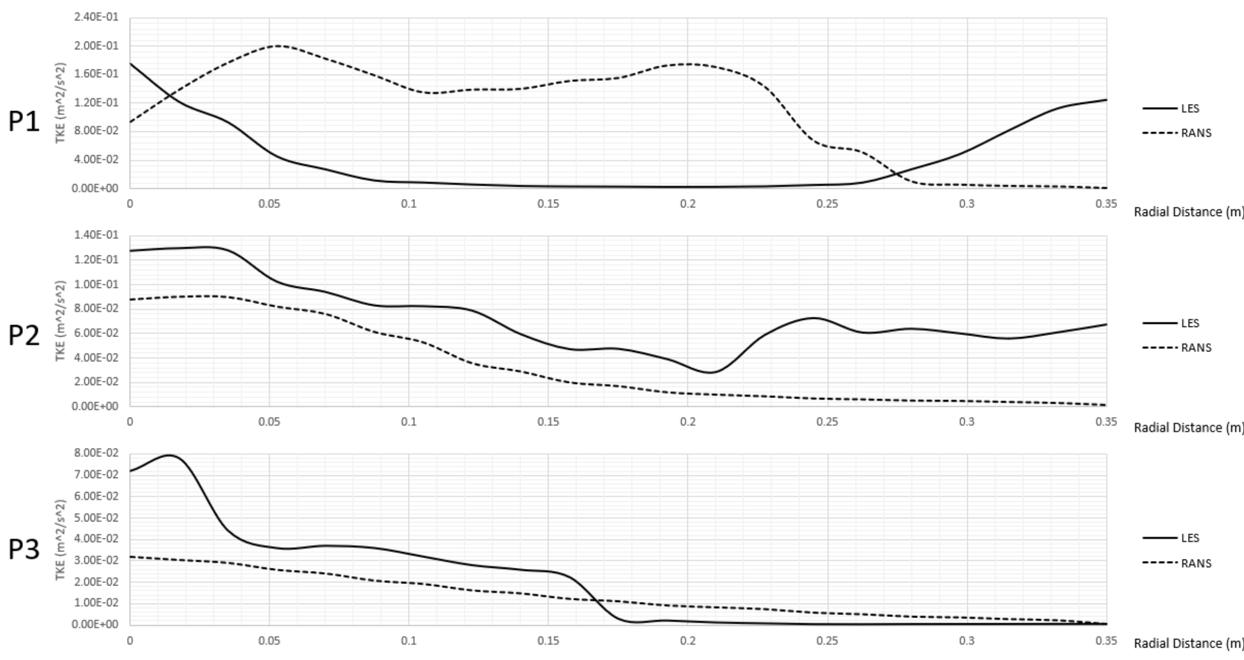

Figure 54. TKE predictions from LES (solid lines) and RANS (dashed lines) plotted against radial distance along the diagonal line (Figure 53). Overall, RANS predicts higher TKE on P1, and LES predicts higher TKE on P2 and P3.

On P1, the difference is most noticeable in radial distance between 0.02 and 0.25 m. In this area, TKE values in RANS stay at a high level, whereas only comparably significant values are observed near the plume (r = 0 m) and vessel wall (r = 0.35 m) in LES. On P2, while both LES and RANS maximum at the upwash plume center, LES produces overall higher TKE. The high value near the radial distance of 0.35 m in LES is caused by velocity fluctuation when flows collide with the vessel wall, which RANS omits. This will be discussed further with visualization of the flow in Section 6.2.3.

LES continues to show higher TKE values in the core region on P3, but the region near the vessel wall no longer has high values. The P3 plane is too high for any strong flows to reach the vessel wall. RANS shows TKE values gradually decreasing radially outward from the maximum value in the center.

6.2.2.2. *Volumetric Analysis*

Figure 55 shows mass weighted averages of turbulence metrics over the entire vessel versus time through the drive, vent, and suction phases. Green, blue, and red lines represent TKE, TDR, and turbulence production, respectively, from LES (top) and RANS (bottom) simulations.

During the drive phase, turbulence production and dissipation in RANS are nearly an order of magnitude greater than in LES. When compared to LES, RANS has 7.2 and 8.3 times higher maximum turbulence production and dissipation rate values, respectively. There also is a significant difference in how the turbulence data in each model reach their maximum values. In RANS, the dissipation and production rates maximum within 0.12 s into the drive phase. In LES, the turbulence metrics increase gradually as the flows speed up in the vessel and Reynolds number increases.

Similar patterns are observed after the drive phase. The turbulence metrics in RANS drop sharply, and turbulence production crosses TDR only 0.02 seconds into the vent phase. This allows TKE to rapidly decrease in RANS. Turbulence production in LES, on the other hand, gradually decreases as the central plume slowly dissipates. As a result, the TKE turning point occurs much later in LES at t = 2.58 s.

**Scenario 1, LES vs. RANS, IPP.*

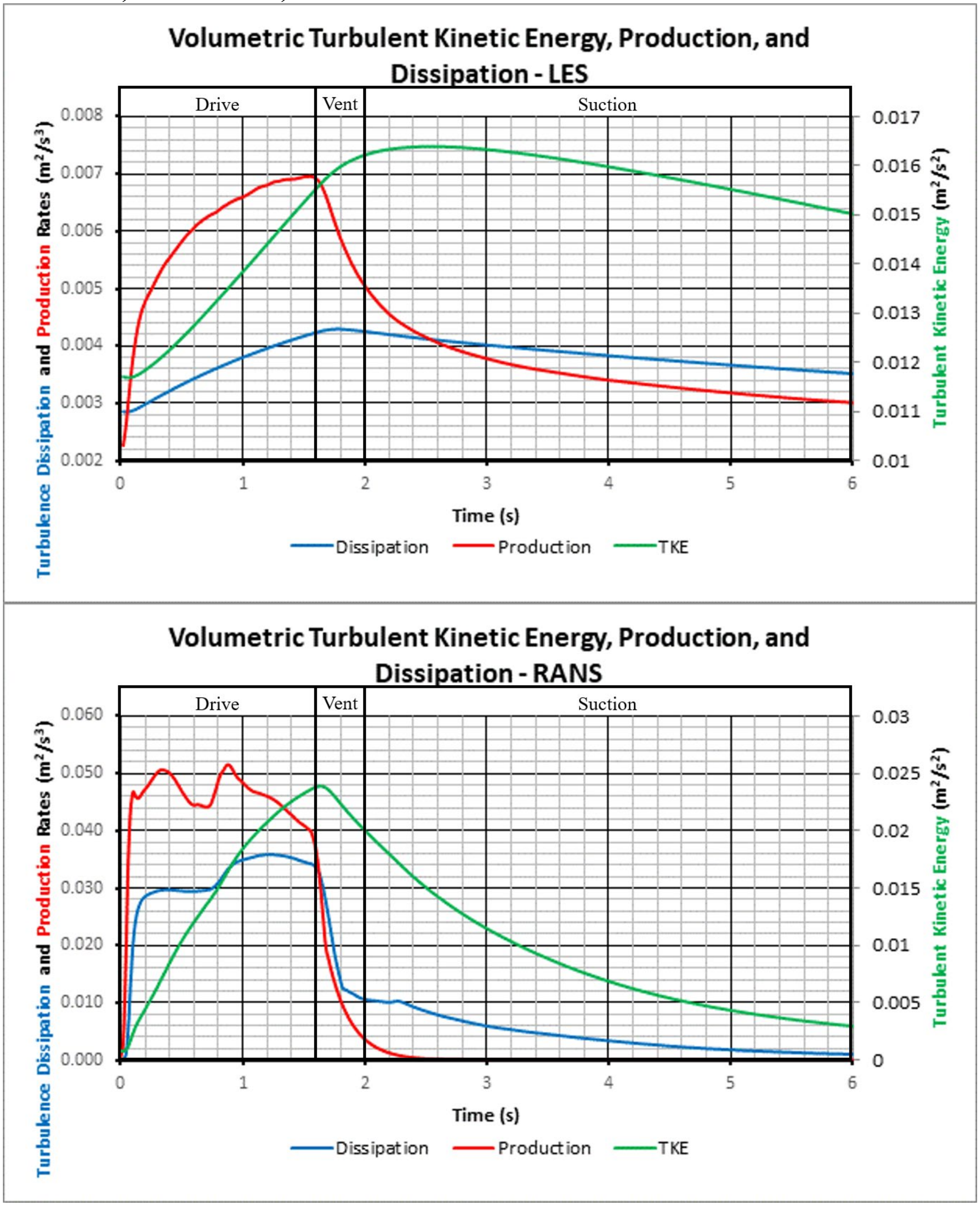

Figure 55. Mass averaged Turbulent Kinetic Energy (TKE), Dissipation (TDR) and Production Rate from LES (top) and RANS (bottom) simulations plotted over cycle time. The vertical axis on the left is for TDR and production, and on the right is for TKE.

Scenario 1, LES (instantaneous) vs. RANS (ensemble average), IPP, Suction phase (t = 12 s)

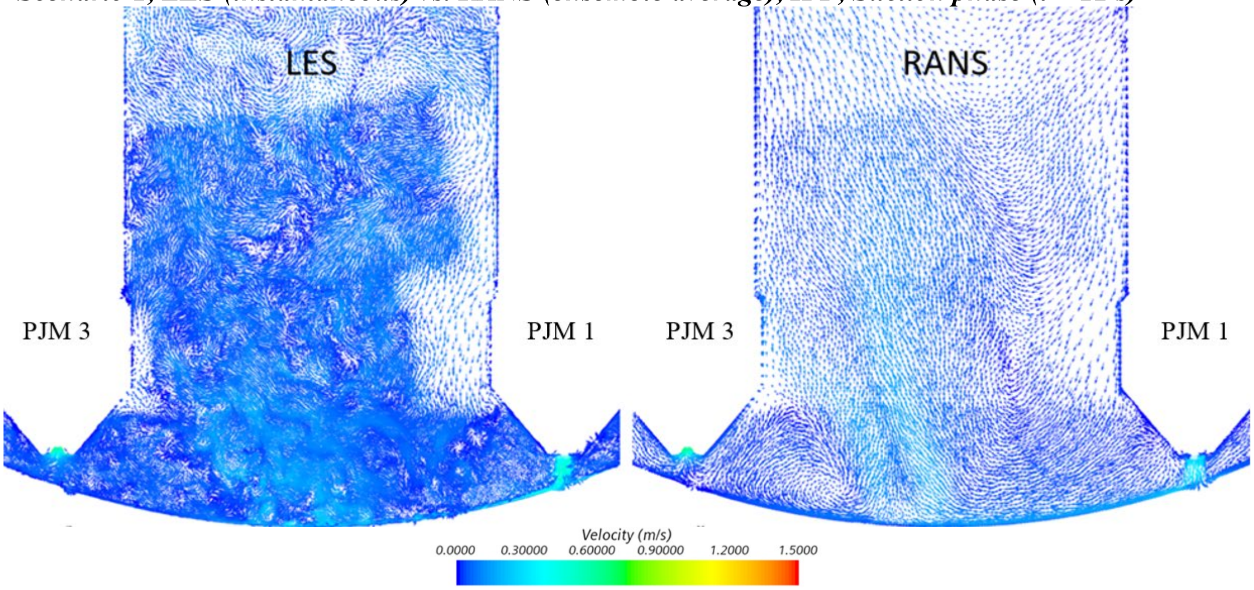

Figure 56. Velocity fields during a suction phase of LES IPP (left) and RANS IPP (right) cases. High turbulence activities are still present in LES with numerous disintegrating eddies.

Figure 56 depicts velocity fields from LES (left) and RANS (right) to show how the differences in turbulence metrics between the two models are caused during the suction phase. The LES data are instantaneous values to emphasize the effects that are lost in RANS. In LES, numerous eddies are dissipating across the entire plane during the suction phase, creating high velocity fluctuations and maintaining high TKE. On the other hand, unsteady RANS captures a few vortices and predicts calm and steady flows for the rest of the vessel. As a result, low mean shear rates are produced, causing RANS to predict low turbulence metrics.

The volumetric analysis allowed for a quantitative comparison of the turbulence metrics of the LES and RANS models. The following points summarize the main observations:

- RANS predicts nearly an order of magnitude higher turbulence metrics during the drive phase than LES.
- In RANS, the maximum values of turbulence metrics are achieved significantly earlier in the drive phase than in LES.

- In RANS, the turbulence metrics drop dramatically at the end of the drive phase. They are retained for much longer into the vent and suction phases in LES.

The second and third points indicate that the vessel bottom region in RANS will experiences disproportionately high turbulence levels; the turbulence production and dissipation are high in the early phase of the PJM cycle (Figure 55) while the plume has only fully formed in the bottom region. In LES, TKE is produced and dissipated more evenly throughout the PJM cycle, allowing the turbulence production and dissipation to take energy away from the mean flows in the middle and top regions as well as the bottom region.

6.2.3. Flow Field Comparison: LES versus RANS

The study's emphasis so far has been on demonstrating how the LES and RANS models match the data from the NETL velocity probe measurements. In this section, the predicted fluid flow quantities will be further compared without reference to the probe positions to analyze the nature of the flow field and the fundamental differences in model performance and capability.

As was discussed in Section 2.2.1, RANS equations are formulated to produce time or ensemble averaged flows. The model can be useful in simulations where only average metrics are required for analysis, but the model provides a highly limited view of instantaneous effects. Although equivalent LES models require significantly more calculation time, data sample collection, and statistical analysis, they are capable of producing more accurate and realistic flow fields and turbulence metrics in various applications [11], [29], [31]. As a result, LES is recommended for applications and analyses closely related to instantaneous flow effects. Several examples with supporting figures will be provided in this section.

Scenario 1, LES (instantaneous) vs. RANS (ensemble average), IPP, End of drive phase (t = 1.6 seconds)

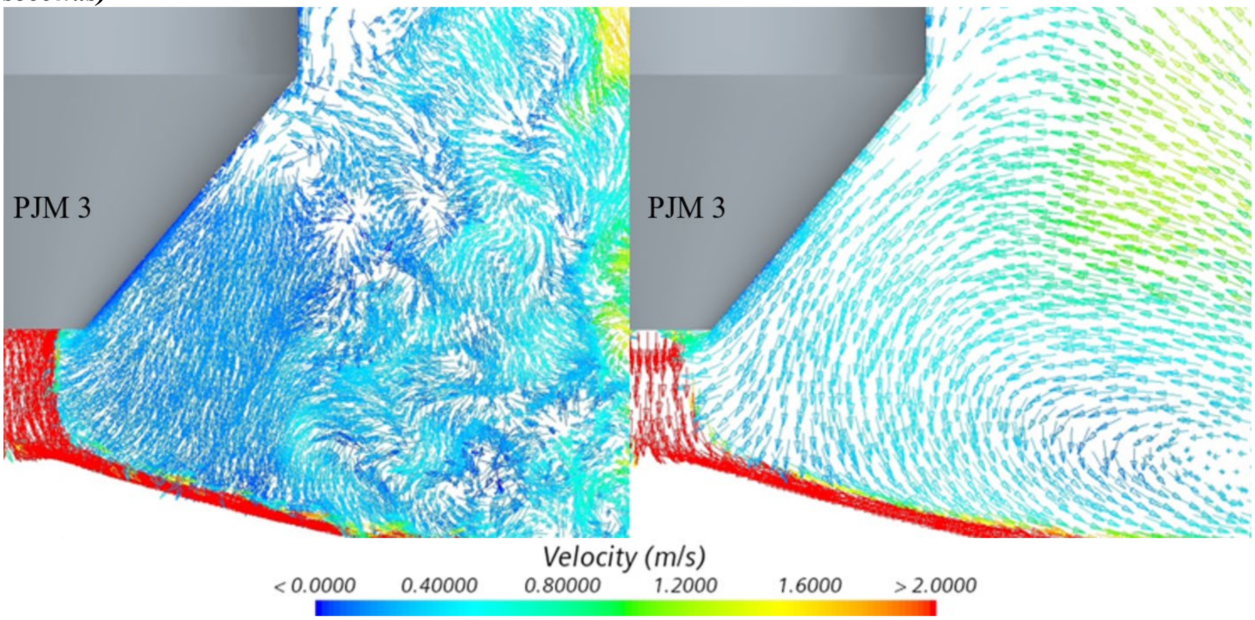

Figure 57. Flows near the dish bottom and a PJM in LES IPP (left) and RANS IPP (right) on a vertical plane. LES shows eddies effectively breaking off the flows, while RANS shows a large vortex.

Figure 57 depicts the flow patterns predicted by LES (left) and RANS (right) models near the dish bottom and a PJM nozzle. The instantaneous LES flows contain numerous smaller eddies, whereas the RANS average flows rotate smoothly around a large vortex structure. While the two models predict similar scales of velocities at the nozzle, dish bottom, and plume core, their dynamics are significantly different. For example, LES flows will be far more effective than RANS flows in demonstrating realistic mixing phenomena. For example, Figure 58, shows 2-D velocity vector plots with fluid tracking points for the LES IPP (left) and RANS IPP (right) cases.

Scenario 1, LES (instantaneous) vs. RANS (ensemble average), IPP.

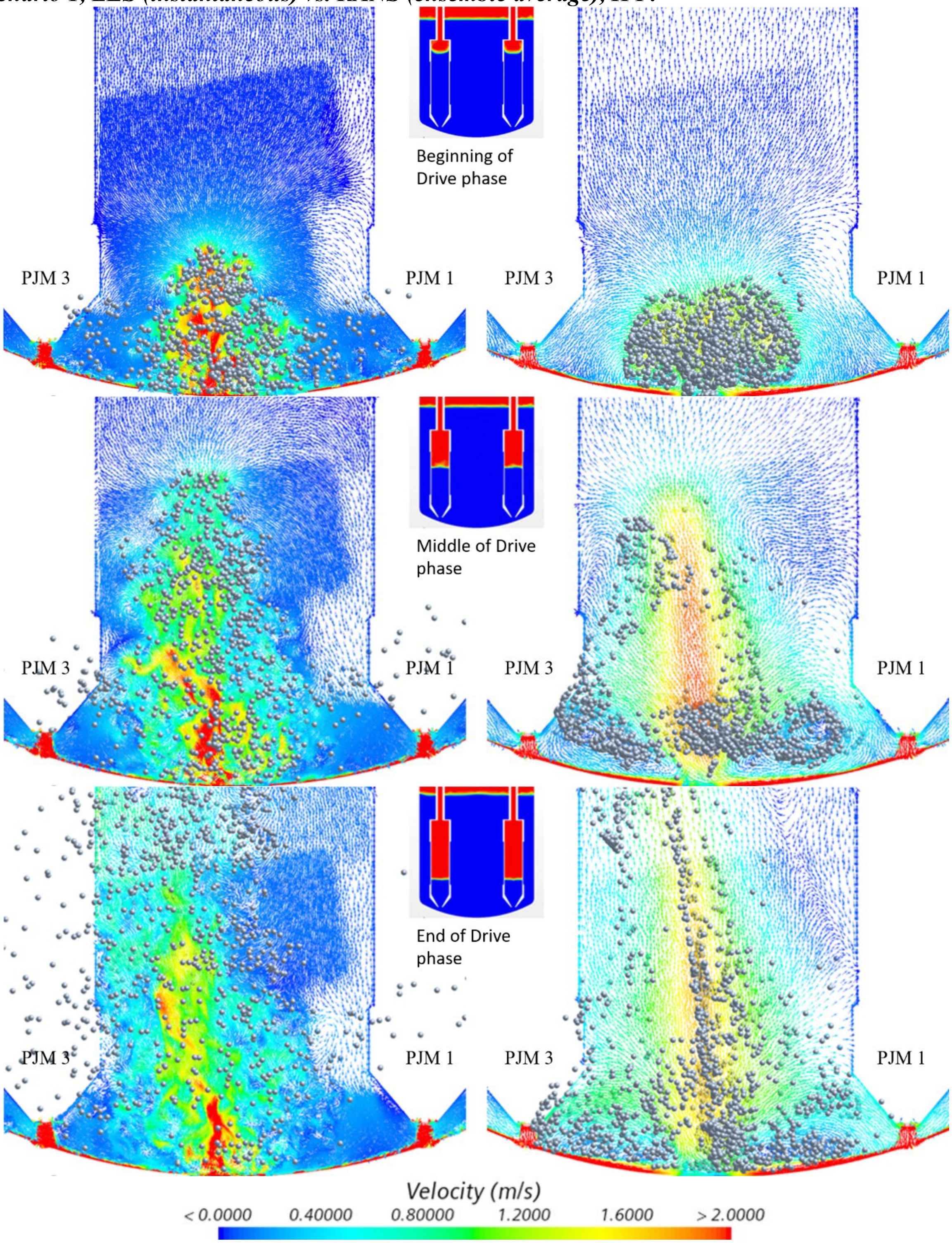

Figure 58. Velocity vector plots with tracking fluid points in LES IPP (left) and RANS IPP (right). While the particles are effectively scattered by eddies in LES, they stay in the vortices and the central plume regions in RANS. The small volume fraction plot displayed in the center is that of air; the blue and red colors represent water and air, respectively.

The snapshots from top to bottom show how the results progress throughout a drive phase. The particles depicted in the figure have no mass – their positions are calculated every timestep based on the 3D fluid velocity. This tracing method is appropriate for the scope of the study as it assumes the solution is a single fluid with a limited particle load (less than 5% in weight) [8]. However, the contrast between the two models shown in the figure will apply to other simulation scenarios with higher particle loads and more sophisticated particle modeling such as Discrete Element Method.

The particle movements in Figure 58 clearly demonstrate why instantaneous flows are necessary to visualize mixing performance of the device. At the end of the drive phase (the bottom row), the majority of the tracing particles are in the bottom vortices or the central plume regions in RANS IPP case (right), in contrast to in LES IPP case (left) where the particles are significantly better scattered by eddies.

The difference in predicted mixing phenomena will have compounding effects as PJM cycles are repeated. In RANS, the flow tracers move together, following the mean flow patterns. They form groups that are either trapped in the vortices or carried to the top region by the central plume. It will take a significant number of PJM cycles to separate the tracers. In LES, the eddies effectively scatter the flow tracers in a few cycles. After 5 cycles, the two simulation models predict significantly different tracer distributions, as shown in Figure 59.

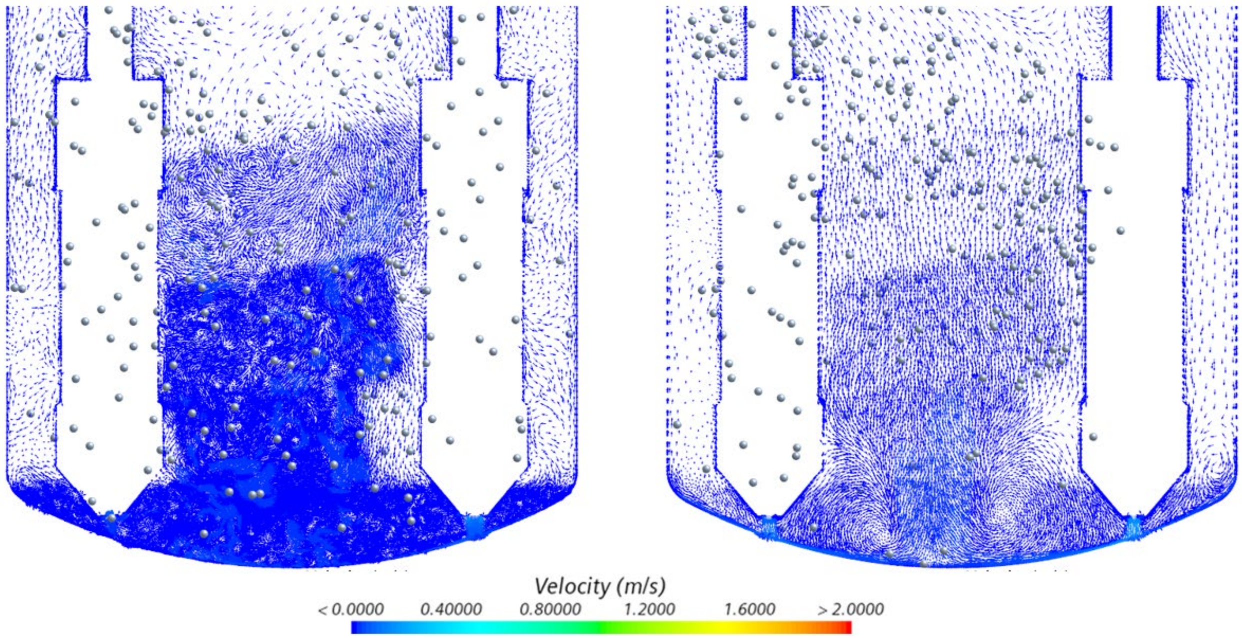

Figure 59. Velocity vector plots with tracking fluid points in LES IPP (left) and RANS IPP (right) after 5 cycles. While the particles are evenly scattered in LES, they stay in the upper left corner in RANS. t = 60 seconds, at the end of cycle 5 suction phase (12 seconds per cycle).

Scenario 1, LES (instantaneous) vs. RANS (ensemble average), IPP, Drive phase.

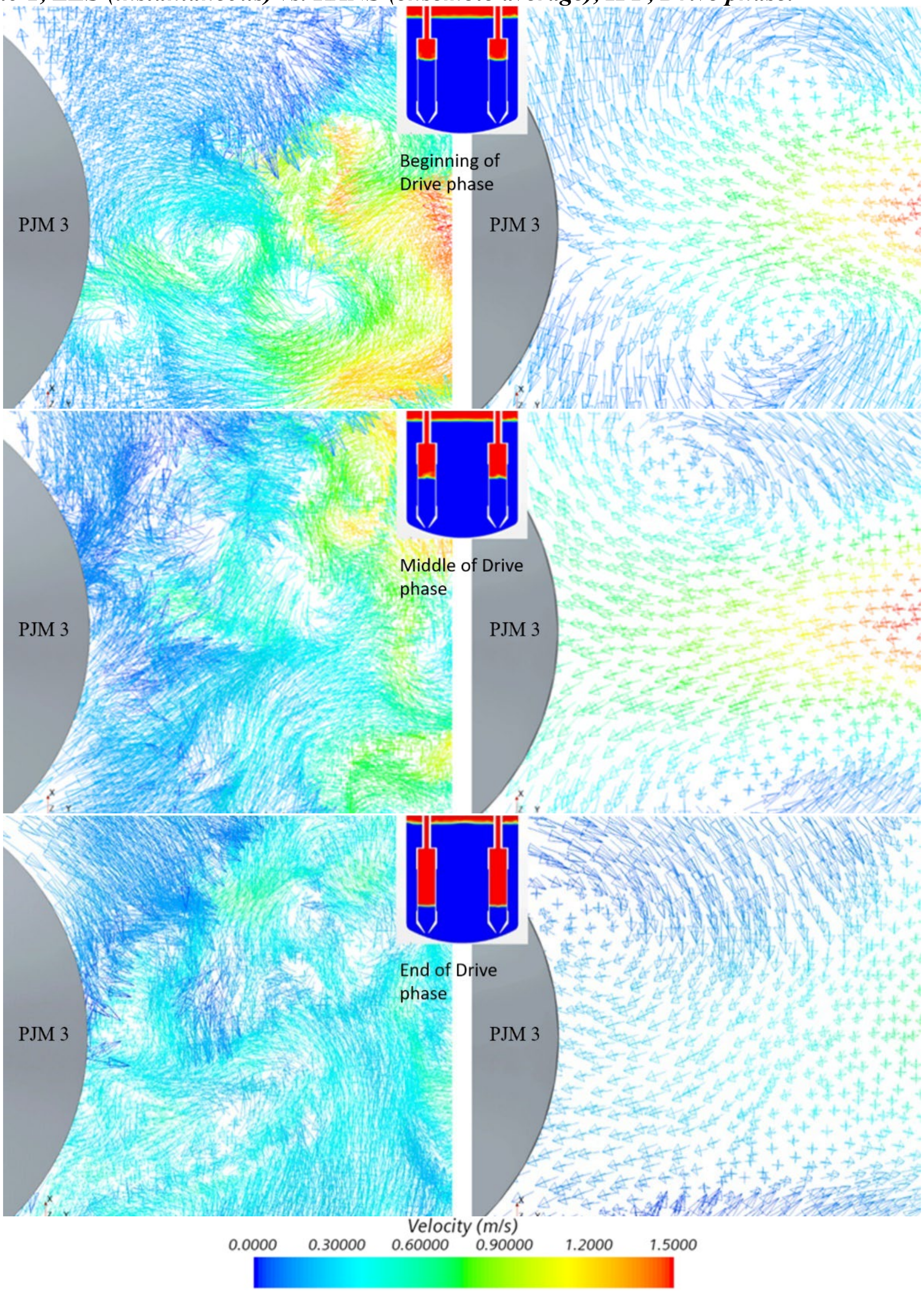

Figure 60. Flows near PJM wall in LES IPP (left) and RANS IPP (right) throughout a drive phase on P1 (Figure 50). In LES, eddies of various sizes collide with the PJM, while in RANS, a constant flow rises and falls in the area. The small volume fraction plot displayed in the center is that of air; the blue and red colors represent water and air, respectively.

Another example that requires instantaneous flow evaluation is in structural analysis of internal vessel parts. Figure 60 shows flow fields on P1 (Figure 50) for the LES IPP (left) and RANS IPP (right) cases. Significant fluctuations in flow velocities observed in the LES results are missing in the RANS results. LES captures the magnitude and frequency of stress at each point on the structure while RANS only provides a time or ensemble averaged result. The frequency and intensity of the fluctuations will be useful information for structural engineers studying the required strength and number of welding joints and braces, examples of which are displayed in Figure 61.

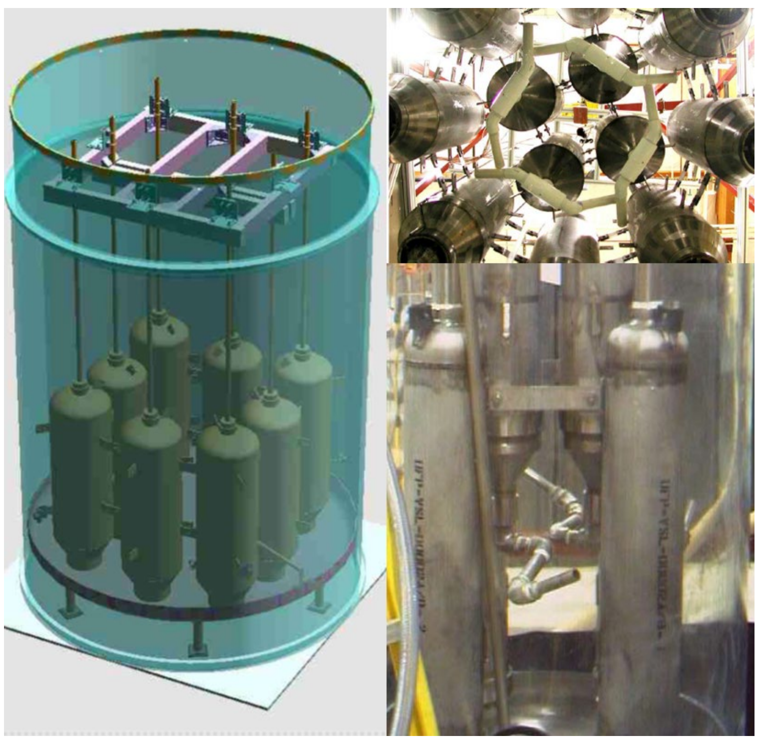

Figure 61. Braces, Welding Points, and Supporting Structures within PJM Vessels, excerpted from [7]

Figure 62 offers another perspective with respect to structural analysis, with particle traces rather than with mean velocity vectors only. In the figure, RANS IPP (right) has significantly more particles colliding at the bottom PJM wall than LES IPP (left). The analyses based on two cases will result in significantly different wear predictions on the PJM wall, especially in the bottom region near the nozzle. Given the permanent inaccessibility of the "black cells" (Figure 2) and the serious consequences of internal parts' failures, the simulation models' ability to aid in structural analysis will be a significant advantage.

Scenario 1, Instantaneous LES vs. RANS, IPP, End of drive phase (t = 1.6 seconds)

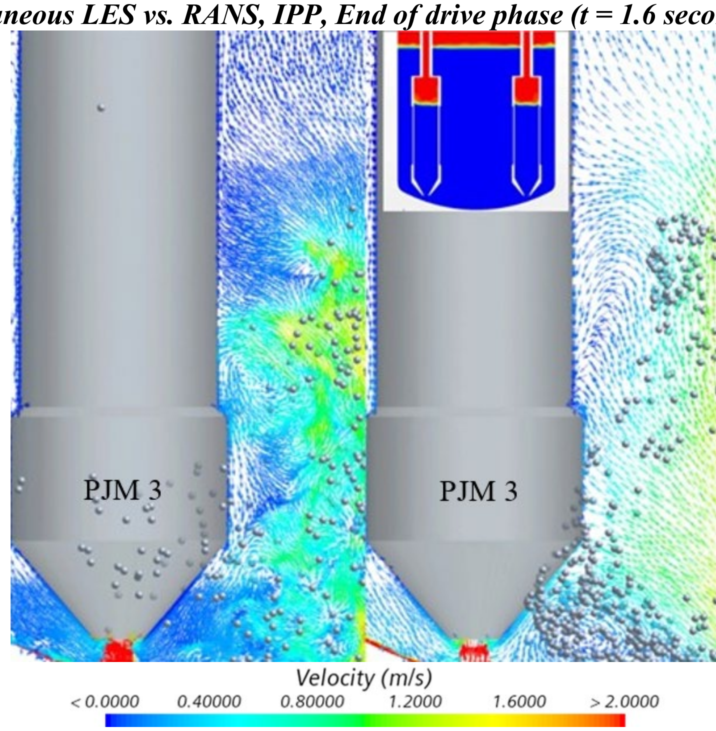

Figure 62. Velocity vector plots with massless particle traces near a PJM. RANS IPP (right) shows significantly more particles colliding at the bottom PJM wall than LES IPP (left).

6.2.4. Summary of Findings

The following is a summary of this LES vs. RANS analysis based on PJM pressure profile Scenario 1:

- Vortex Recirculation near PJM nozzles: only two large vortices are visible near the dish bottom in RANS, whereas small vortices are visible from the bottom to the top regions in LES. Because the vortices are exaggerated in size, the central plume is separated from the dish bottom, and its entire structure is "lifted" in comparison to how it appears in LES. As a result, the plume velocities are generally shifted, resulting in lower velocity readings at the bottom probe and higher velocity readings at the middle and top probes.

- Turbulence Quantities: the turbulence metrics are well correlated with the vortex recirculation comparison of LES and RANS. TKE and TDR are significantly higher in RANS in the bottom region with large vortices and lower in the middle and top regions with no vortices. Exaggerated turbulence metrics in RANS contribute to lower energy for mean flow and velocity readings at the bottom probe location. The absence of vortices and low turbulence metrics in RANS in the upper regions artificially preserve the plume's vertical momentum and allows for higher velocities at the middle and top probe locations.
- Fluid Tracer Comparison: to highlight the limitations of RANS, mixing prediction and structural analysis were performed based on the predicted flows of the two simulation models. RANS may be an efficient tool for predicting averaged flows, but its inability to resolve eddies and simulate instantaneous flows limits the model's applications significantly. The use of massless particles to trace the flows in LES and RANS demonstrated the importance of eddies in mixing phenomena, and plots with eddies colliding on various internal structures of the PJM vessel demonstrated that structural analysis cannot be done solely on averaged flow fields.

6.3. Comparison Analysis between LES and LBM

In Chapter 5, it was shown that LBM underestimated velocities at all three probe locations when compared to the NETL data, whereas LES successfully matched them within 95% confidence intervals. As discussed in Section 4.3.2 with Figure 39, the LBM did not reach mesh independence, which is suspected to be a major contributing factor for its poor validation against the NETL experimental data. In this section, the two simulation models' 2D vector plots and turbulence metrics are compared to determine how the differences impact the models' performances.

6.3.1. Flow Characteristics Comparisons Focusing on Vortices

Figure 63 shows the velocity data ensemble averaged over 100 cycles on a vertical plane for the LES IPP (left) and LBM IPP (right) cases. The overall plumes characteristics differ significantly between the two models, particularly in the regions denoted by black lines in the figure. The plume in LBM is considerably wider at its base, which dilutes the upward momentum and results in lower core velocities than in LES. This is consistent with the findings in Figure 46, which shows that the vertical velocities predicted at the probe locations (red dots in Figure 63) are lower in LBM than in LES.

*Scenario 1, LES vs. LBM, IPP, Ensemble Average, End of drive phase (t = 1.6 seconds).

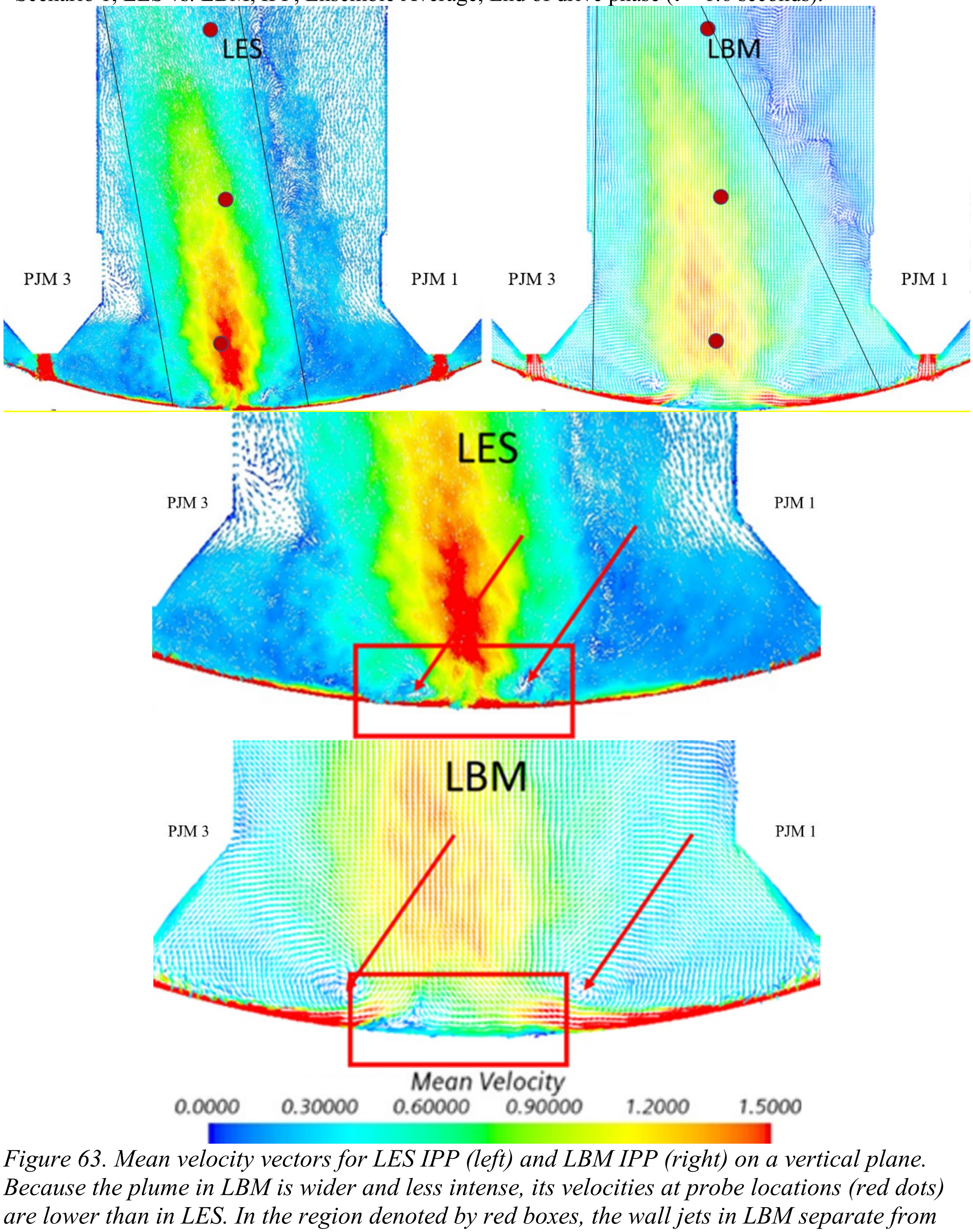

Figure 63. Mean velocity vectors for LES IPP (left) and LBM IPP (right) on a vertical plane. Because the plume in LBM is wider and less intense, its velocities at probe locations (red dots) are lower than in LES. In the region denoted by red boxes, the wall jets in LBM separate from the dish bottom earlier than in LES, resulting in the vortices (indicated by red arrows) being farther apart.

The bottom two images in Figure 63 show a close-up view of flows at the vessel's dish bottom. The two cases have significantly different flows near the bottom center, which is indicated in the figure by red boxes. In LES, wall jets create thin layers of high velocity flows that collide at the center. In LBM, the wall jets separate from the dish bottom as they approach the center, resulting in vortices (marked by red arrows) that are larger and farther apart than those in LES. The RANS model demonstrated a similar behavior in the bottom region – exaggerated vortices take energy away from the plume and lower the velocity predictions. In RANS, this is caused by the model's limitations as the mesh reached independence (Section 4.1.1). In LBM, the resolution seems to play a significant role, as the model did not reach grid independence (Section 4.3.2) and its boundary modeling is not well suited for curved walls.

As discussed in Section 2.5, LBM is often referred to as a "meshless" system because there is no meshing step in simulation pre-processing. Its grid algorithm simply aligns homogeneous lattice points within fluid regions of the simulation domain. As such, there are no surface tessellations or surface mesh to represent boundaries in LBM. The model simply assigns a boundary condition at a side where a lattice point does not detect a neighboring lattice point. While this may be useful in some cases, it can result in inaccurate boundary shapes and artificial effects. An example is shown in Figure 64. The blue line depicts the actual shape of a curved boundary, while the red line depicts how LBM would recognize it with insufficient grid resolution. The phenomenon is often referred to as the "staircase effect" [32], which can produce artificial velocity fluctuations and inflated turbulence metrics near curved boundaries [16], [33].

Numerical models like the Mei-Luo-Shyy (MLS) method [34] were developed in an attempt to overcome the issue for curved boundaries, but they are only applicable to highly specific conditions and can cause adverse effects on scenarios that they are not intended for [18]. For example, applying MSL method to the LBM model in this study significantly increased the simulation time without improving the results. Excessive lattice refinements appear to be the only reliable solution [35], as the red line would get closer to the blue line in Figure 64 with more refined lattice structure. Unfortunately, achieving sufficiently refined grid to negate the LBM boundary effect can be extremely costly due to its homogeneous lattice structure. This is the most significant reason for the model's failure to achieve grid independence, as discussed in detail in Section 4.3. It appears that LBM requires an effective local refinement method and significant performance enhancement to be a competitive simulation solution for systems with various length and velocity scales such as the PJM vessel. Local refinement was attempted in the LBM model using M-Star, but the interpolation cost was unexpectedly high at the interface between the regions of different lattice grid size. The method was not pursued as the simulation time between the locally refined and universally refined models was small. It is expected that the method will be further developed in the future to improve functionality, at which point a test should be performed for re-evaluation.

6.3.2. Turbulence Comparison Analysis

To demonstrate how the “staircase” effect on a curved boundary affects velocity fluctuation and turbulence, Figure 65 marks locations that exceed a TKE value in red. The TKE threshold value is chosen so only small regions directly surrounding the nozzle jet impingements are marked in LES. In LBM, however, almost the entire dish bottom is marked, indicating significantly higher TKE prediction on the curved boundary.

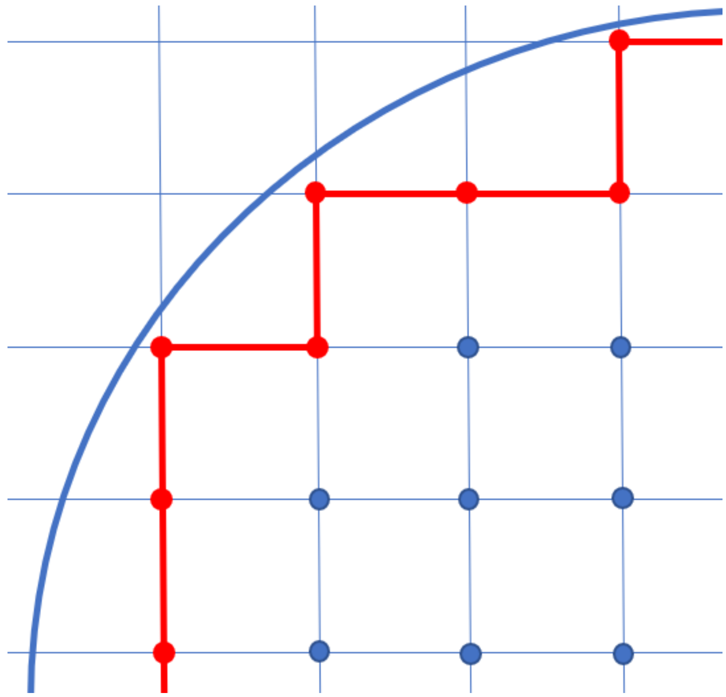

Figure 64. Visualization of staircase approximation in LBM. The blue curve represents the boundary shape, and the red line represents its approximation in LBM.

Scenario 1, LES vs. LBM, IPP, End of drive phase (t = 1.6 seconds).

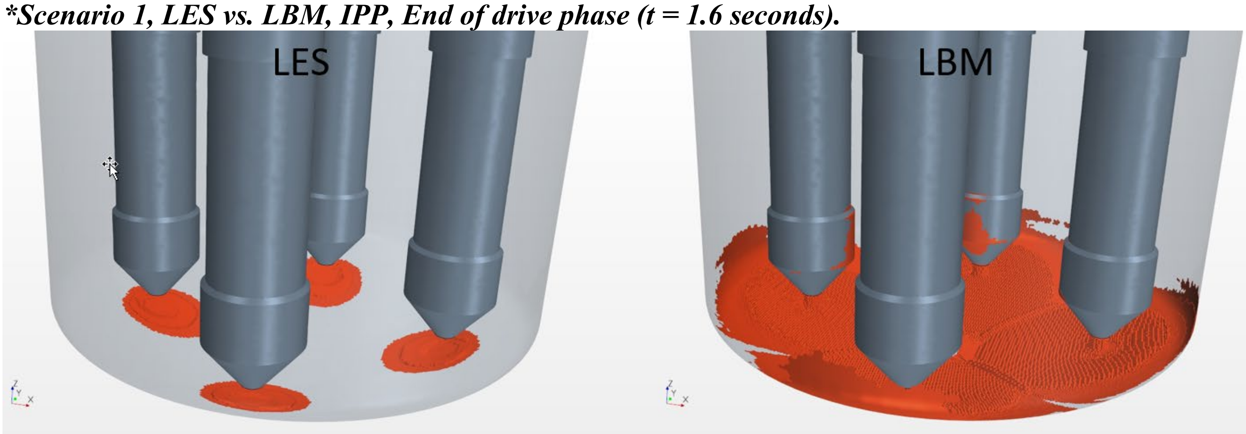

Figure 65. Regions of TKE > 0.52 m^2/s^2 marked in red for LES IPP (left) and LBM IPP (right) cases. While only a small circular region under each PJM is marked in LES, the entire dish bottom is marked in LBM.

Figure 66 shows TKE values on three horizontal planes that are illustrated in Figure 50. The images in the left column depict data for LES IPP case, while the images in the right column depict data for LBM IPP case. TKE values on P1 are significantly higher in LBM due to the plane's proximity to the dish bottom, where the turbulence metrics are inflated by the "staircase" effect. The boundary approximation, as discussed in Section 2.5, can artificially increase velocity fluctuations. TKE values are higher near the vessel wall (peripheral region) on all three horizontal planes for the same reason. On the other hand, in the central region, TKE values on P2 and P3 in LBM are lower because the plume velocity is weaker than LES and the planes are sufficiently spaced from the dish bottom.

Scenario 1, LBM, IPP, End of drive phase (t = 1.6 seconds).

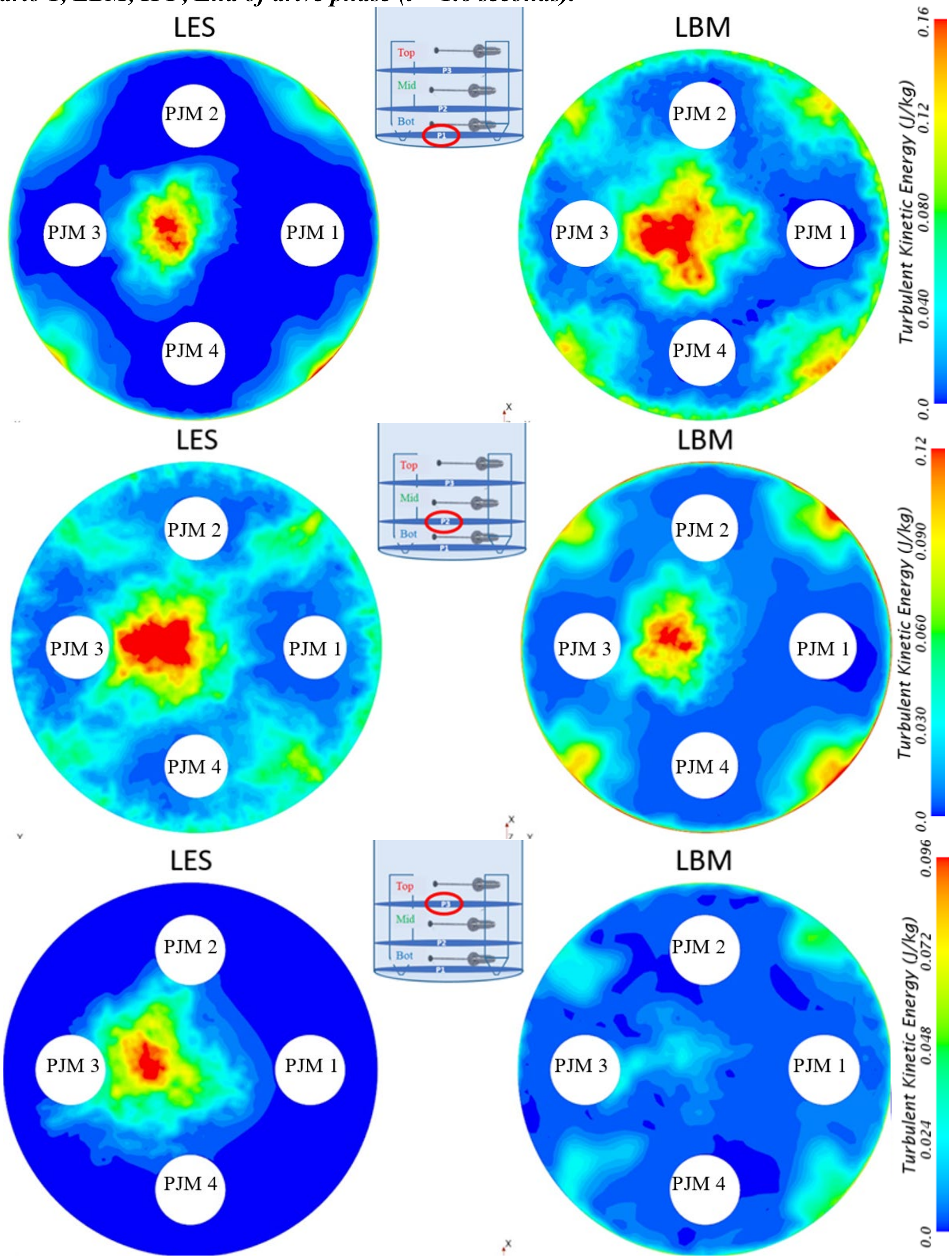

Figure 66. Turbulence Kinetic Energy for LES (left) and LBM (right) IPP cases reported on P1 (top row), P2 (middle row), and P3 (bottom row). In comparison to LES, LBM produces higher TKE on near the curved boundaries (dish bottom and vessel wall).

6.3.3. Summary of Findings

In conclusion, the study identifies a few significant issues with the LBM model. The following list provides a summary:

- Due to the curved bottom of the vessel, the LBM model will likely require extremely high resolution to minimize the effects of the staircase approximation and accurately capture the impingement flows and wall jets.
- The homogeneous lattice structure and lack of effective local refinement in LBM render its grid refinement highly inefficient and expensive. As the simulation method is rapidly evolving, a test should be performed in the future for re-evaluation of the effectiveness of local refinement in LBM.
- As a result, LBM's computational advantage discussed in Section 2.5 is not realized for the simulation of the study. The model is unable to achieve grid independence or apply adequate resolutions for curved boundaries while maintaining a reasonable runtime, reducing the accuracy and reliability of the final results significantly.

6.4. Vessel Flow Field Characteristics

In order to present flow field characteristics throughout the vessel, a series of ten animations were prepared and are contained in a PowerPoint file that accompanies this manuscript.

Animation 1 illustrates the main flow features in the PJM vessel. They are displayed on a vertical plane spanning the vessel and passing through the centerline, as well as PJM 1 and 3 (illustrated in Figure 13). The larger figure on the left shows the velocity vectors for the RANS IPP case. The vector animation depicts how the nozzle flows converge at the bottom of the dish to form the central plume. As previously discussed in Section 6.1, the plume in the IPP case develops with a tilt to the left due to PJM pressure imbalance. The animation also shows the formation and dissipation of vortices between the plume and nozzle areas. The smaller figure on the right depicts a volume fraction scalar plot. The volume fraction displayed is that of air; the blue and red colors represent water and air, respectively. The animation begins at the start of a drive phase, with the PJMs fully charged with water. As the drive phase progresses, air is injected into the PJMs, forcing water out and causing the nozzle flows.

Animations 2–5 compare the instantaneous and ensemble averaged flow fields from the LES IPP and RANS IPP cases, respectively. The purpose of this comparison is to highlight the level of detail that the RANS results omit.

Animation 2 depicts flow field vector animations on P1 (illustrated in Figure 50) in the LES IPP (left) and RANS IPP (right) cases. While RANS results show the general direction and magnitude of the flows, they do not show the frequency and intensity of their variations. The LES velocity fluctuations allow the model to analyze the stress that the structures would experience over time. This will be critical information for structural engineers researching the required strength and number of welding joints and braces, as shown in Figure 61.

Animation 3 offers another perspective for structural analysis, with 3-D fluid tracing points rather than with 2-D velocity vectors only. In the figure, RANS IPP (right) has significantly more tracer particles colliding at the bottom PJM wall than LES IPP (left). The analyses based on two cases will result in significantly different wear predictions on the PJM wall, especially in the bottom region near the nozzle. Given the permanent inaccessibility of the "black cells" (Figure 2) and the serious consequences of internal parts' premature failures, the simulation models' ability to aid in structural analysis will be a significant advantage.

In Animation 4, the tracer particle movements clearly show why instantaneous flows are required to accurately analyze the mixing performance of the device. Throughout the drive phase, the majority of the tracing particles are either trapped in the central plume regions or the bottom vortices in the RANS IPP case (right). In the LES IPP case (shown on the left), on the other hand, the eddies effectively scatter the particles to other parts of the vessel.

To examine the effect in greater detail, the velocity vectors in Animation 5 provide close-up views near the dish bottom at the start of the drive phase. Flows from the nozzles quickly sweep across the dish bottom at the beginning of the animations. Eddies appear in the wake of the wall jet flow in LES IPP (left), lifting and scattering the tracing particles. The turbulent structures are absent in RANS IPP (right), and the majority of particles are pushed towards the center region instead.

Animation 6 continues the comparison between the LES IPP (left) and RANS IPP (right) cases in the top region of the vessel. Flow velocities in this region are significantly lower than in the bottom region. Without strong and distinct fluid flows, the differences between the instantaneous and ensemble average results of the LES and RANS models can be even more pronounced. As the RANS model averages out the small eddies, it predicts that fluid flows in the entire region will disappear along with the central plume when the nozzle flows stop. The LES model, on the other hand, captures eddies that dissipate across the entire upper region long after the central plume has vanished, allowing mixing to take place long after the nozzle flows have stopped. The impact will compound as the mixing cycle for PJM mixing operations is repeated numerous times, and capturing the phenomenon will have a significant impact on accurately predicting the device's performance.

Animation 7 shows fluid flow with tracer particles from LES UPP (left) and LES IPP (right). The comparison shows how the tilted central plume would have an uneven effect on the structural integrity of the PJMs. In the UPP case, the plume flows do not directly hit either of the PJMs in the UPP case, and the particles collide against the two PJMs evenly throughout the drive phase. In the IPP case, the middle to upper portion of the PJM on the left side experiences strong turbulent flows and that carry the particles. The results clearly show that the braces and external walls on the PJM will experience significantly more wear.

Animations 8 and 9 compare the fluid flows from left and right sides of the LES UPP case. While the RANS results may show identical flows from both sides, the instantaneous LES flows show that the timing of eddies colliding against the two PJMs will be asymmetric. Animation 7 focuses on the nozzle area while Animation 8 focuses on the PJM external wall. In both locations, while the flows on the left and right sides are similar in magnitude on average, the eddy structures differ significantly at any point in time.

Finally, Animation 10 shows the instantaneous velocity field generated by M-STAR, which was the solver used to run the LBM simulations. The animation clearly depicts the nozzle flows from the four PJMs, wall-jets, central plume, and water-air interfaces within the PJMs and at the vessel's top. If the challenges outlined in Section 6.3 are overcome, the model has the potential to be a valuable analysis tool.

6.5. Chapter Summary

Chapter 5 demonstrated how the LES, RANS, and LBM models performed in Uniform and Individual Pressure Profiles to match NETL EM probe velocity measurements. In this chapter, the flow fields and turbulence metrics predicted by the simulation models are examined to explain the differences in performance.

Section 6.1 demonstrated how the pressure imbalance in IPP, as well as the resulting shift in plume orientation, changed the relative locations of the probes and affected the velocity measurements. The analysis highlighted the importance of accurately simulating the internal pressures of each PJM, as a slight shift in plume orientation can have a significant impact on the measurements at the probe locations.

Sections 6.2 and 6.3 compared RANS and LBM models' flow fields and turbulence metrics are compared to those of LES. The LES model served as a benchmark as its IPP case predictions matched the NETL laboratory results within the 95% confidence intervals. Compared to LES, both RANS and LBM predict exaggerated vortices near the dish bottom next to the upwash plume which inflated turbulence kinetic energy and dissipation rate in the area, resulting in underestimated velocities at the bottom probe location. At the middle and top regions, RANS' lack of vortices artificially lowered turbulence metrics and resistance for the averaged flows, contributing to the model's overpredicted velocities at the middle and top probes. LBM, on the other hand, continued to underpredict probe velocities in the middle and top regions, due to the overpredicted turbulence metrics near the curved vessel wall. The comparison of RANS and LBM to LES reveals a negative correlation between turbulence metrics and mean velocity predictions; when they overpredict turbulence metrics in a region, they produce underpredicted mean velocities.

This chapter's vortices and turbulence metrics analyses clearly show the simulation model's performance differences. Considerations of their simulation costs will be included in the following Conclusion chapter to make recommendations on how to use these models, as well as future research.

7. Conclusion

In this study, transient simulation models for the NETL laboratory scale PJM mixed vessel were developed using Large Eddy Simulation (LES), unsteady Reynolds-Averaged Navier-Stokes (RANS), and Lattice Boltzmann Method (LBM) techniques. Each simulation model was validated against NETL laboratory measurements of vertical velocity in the central upwash region of the vessel to ensure its accuracy before being used to generate full 3-D flow fields and turbulence metrics that are difficult to measure experimentally.

7.1. Validation of Simulation Models

In the NETL experiments, velocity data were collected at three EM probes, as shown in Figure 12. The probes are located near the vessel's radial center at three height levels, measuring vertical velocity of the up-wash plume. These are the key measurements for the mixer's performance, as the plume drives the vessel's contents upwards from the bottom and dissipates in the upper region. Three test scenarios were carried out at NETL, each with a different water depth, drive phase length, and drive pressure. More than 100 PJM cycles of data were collected for each scenario that were used to construct the cycle resolved average velocity at each probe location.

The simulation models replicated the experiment by predicting vertical velocities at the EM probe locations. The LES and LBM simulation runs were repeated until over 100 ensemble samples were accumulated at each time in the PJM discharge cycle. Statistical analyses for cycle resolved average velocity, 95% confidence intervals, and turbulence metrics (kinetic energy, dissipation rate, and production rate) were then performed. RANS was not subjected to this procedure because the model predicts averaged flow quantities by default. Table 9 lists the number of RANS, LES, and LBM simulation cycles performed for the three operating scenarios.

The NETL data revealed a possible synchronization issue among the internal pressure profiles of the four PJMs used to control the pulsed jet discharge cycle. To investigate, Uniform Pressure Profile (UPP) and Individual Pressure Profile (IPP) scenarios were prepared for each simulation model as described in Section 3.2. When the IPP and UPP simulation results were compared, it was revealed that the imbalance in the PJMs' internal pressure caused a significant shift in the plume structure. While the overall structure of the plume remained unchanged, the shift moved the plume's core region away from the EM probe locations, which had a significant impact on their velocity readings. The phenomenon is best illustrated by contrasting the LES model's IPP and UPP results, which are discussed in detail in Section 6.1. The LES IPP simulation predicted probe velocities from NETL laboratory measurements within the 95% confidence interval, whereas the UPP counterpart reported 11% error on average. Based on the findings, it is recommended that the pressure readings of each PJM be closely monitored and accurately reflected in the simulation.

When the unsteady RANS results are compared to the NETL experimental data, the predicted probe velocities significantly deviate (21% on average) from the NETL measurements for both the UPP and IPP cases. Analysis demonstrated that RANS' reliance on modeled turbulence metrics rather than resolving eddies resulted in incorrectly predicting vortex locations and critical flow patterns in the PJM discharge nozzle and upwash plume regions.

With an average difference of 36%, LBM predictions were also a poor match for the NETL experimental data. It also required the longest simulation time among the three simulation models, as shown in Table 16. The most significant disadvantage of LBM was its rigid grid system, which was inappropriate for the PJM vessel's widely varying length scales, as shown in Table 4. The homogeneous lattice structure and absence of an effective local refinement method forces the model to pick one length scale that is not optimal for any of the three scales shown in the table. As a result, the model was not able to reach mesh independence within the available resource and time constraints.

Being able to effectively resolve instantaneous flows and eddies of various scales, the LES model outperformed other models in terms of accuracy. As previously stated, using IPP instead of UPP significantly improved the LES model's predictions, and the LES IPP case is the only one that successfully matched the NETL measurements at all three EM probes within the 95% confidence intervals. While the LES UPP case outperformed the RANS and LBM models, its 11% averaged error places its predicted results outside the confidence intervals.

7.2. Performance Evaluation of Simulation Models

The superior accuracy of the LES model came at a high computational cost, especially when compared to the RANS model. With its eddy resolution varying with grid scale, the model required significantly more cell numbers to achieve mesh independence, resulting in 6.1 times longer computation time than the RANS model for simulating one PJM operation cycle. LES also requires significantly more data because its instantaneous flow results usually require statistical analyses. The LES IPP case required 100 PJM cycles to achieve statistical convergence in this study, whereas the RANS IPP case required only 10 cycles. The significant difference in simulation time can make the LES model prohibitively expensive, especially in scenarios requiring quick turnaround time. While relatively inaccurate, a rapid succession of RANS simulations with variations in the geometry, fluid properties and process operations can provide useful and timely comparison data.

The detailed comparison of RANS and LES results allows us to determine when each model should be used. RANS is an effective comparison tool for factors that have broad-level impacts on fluid phenomena. For example, the efficiency advantage of the RANS model allowed for gas compressibility (Section 4.1.2) and fluid viscosity (Section 4.1.3) tests to be performed for this study. However, as illustrated by Figure 48 in Section 6.2.1, RANS struggles to accurately capture the details of the PJM operations' highly transient and rotational flows. With the fluid tracking points, Figure 58 in Section 6.2.3 also demonstrated why instantaneous data only available from LES are necessary to have an in-depth understanding of the mixing phenomena caused by the key flows within the PJM vessel.

The comparison analysis between the LBM and LES models further highlighted the limitation of LBM lattice structure for the device. The "staircase approximation" depicted in Figure 64 exacerbated the model’s insufficient resolution at the vessel bottom. As a mesh-less system, LBM often struggles to capture curved boundaries accurately. The bottom of the PJM vessel is dish-shaped, and it serves an important role as an impingement surface for the nozzle flows which drives the central upwash plume. The impact of the staircase approximation is well illustrated in Figure 63 and Figure 65, which show that the wall jet and central plume flows deviate significantly from those predicted by the LES model, and the LBM model's turbulence dissipation rates on the dish bottom are artificially high, respectively.

These issues of LBM can be addressed in the future, necessitating a re-evaluation of the model. Curved boundary models for improved accuracy are being actively investigated [17], as well as local refinement methods [37], [38]. If the developments enable the model to effectively overcome the outlined flaws, LBM may yet prove to be a powerful option for closing the gap between the accuracy of LES and the efficiency of RANS.

Because the LES model produced the most accurate predictions, it is exploited to generate animations and still images on various 2D planes that depict complex flow patterns throughout the vessel with numerous local jets and mixing layer vortices. Analysis of the structures revealed their critical roles in determining the local turbulence quantities and the size and strength of the central upwash plume, ultimately affecting the predictions at the three EM velocity probe locations.

7.3. Future Research

Future research should also include an experimental program to acquire more velocity data throughout the PJM vessel. In this study, the simulation models were validated using vertical velocity measurements at three fixed points within the central upwash plume. This, however, is not a guarantee that the model yields accurate predictions in the entire vessel, especially in regions far from the EM probes. 3D velocity data should be collected at various points on the 2-D vertical and horizontal planes depicted in Figure 28 and Figure 50. While technical constraints may result in insufficient resolutions for refined velocity gradient calculations, the data will allow visualizations of flow patterns, vortex locations, and turbulence kinetic energy, vastly improving the validation method and thus confidence in the simulation models.

The experiment will ideally be carried out with well-synchronized PJMs, which will prevent imbalanced or premature wear on the supporting structures and satisfy the symmetry assumption for the vessel (depicted in Figure 13). This will allow the measurement points to be focused on one quarter rather than the entire vessel. The symmetry will also allow any future simulation models to utilize UPP, realizing its efficiency advantage over IPP that was shown in Table 9.

Appendix

A. PJM Internal Pressure Data

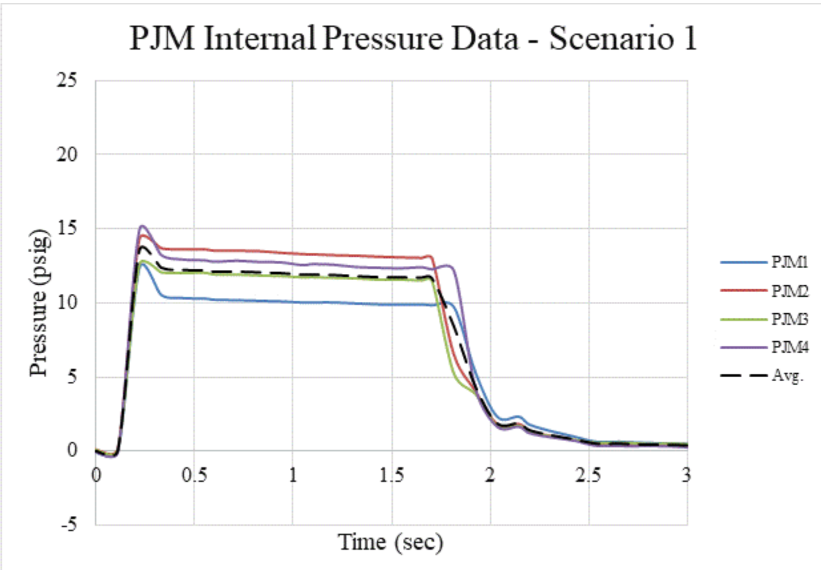

Figure 67.PJM internal pressure during NETL mixing cycle, Scenario 1. The four solid lines represent the internal pressure measurements of the four PJMs. The dashed line represents the average value.

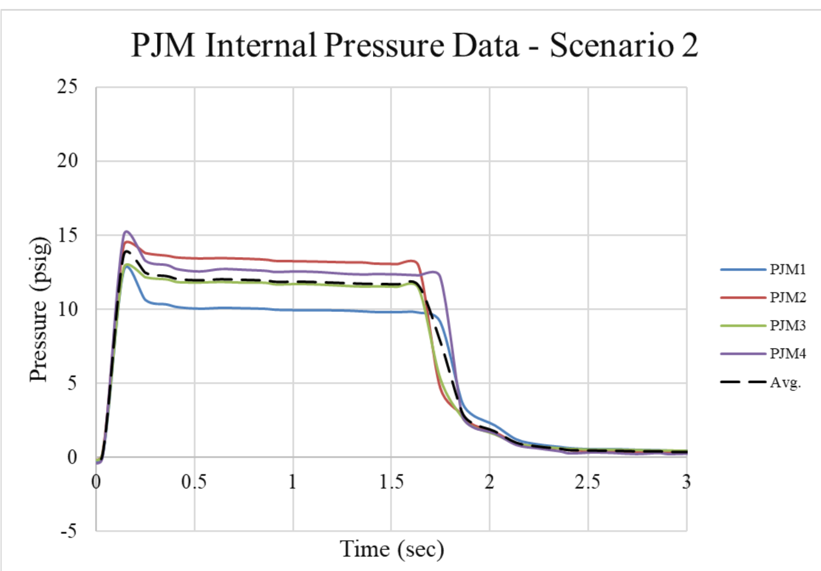

Figure 68. PJM internal pressure during NETL mixing cycle, Scenario 2. The four solid lines represent the internal pressure measurements of the four PJMs. The dashed line represents the average value.

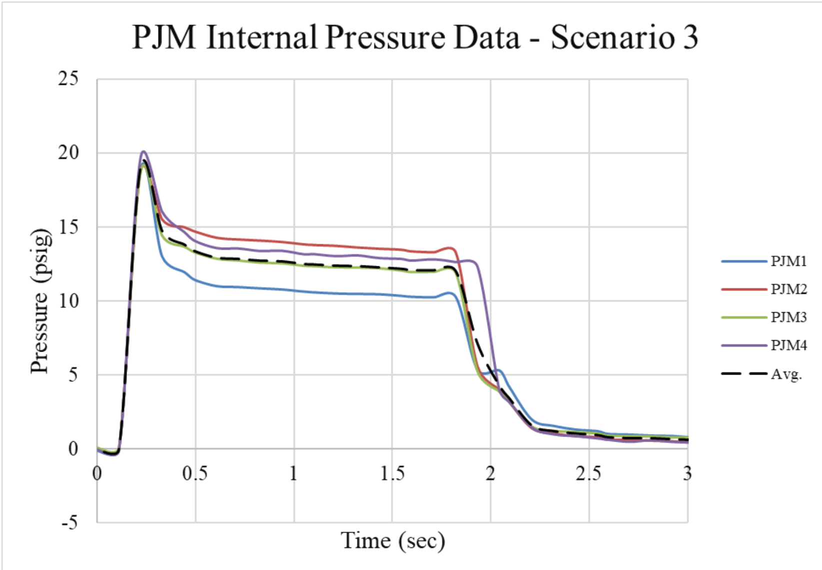

Figure 69. PJM internal pressure during NETL mixing cycle, Scenario 3. The four solid lines represent the internal pressure measurements of the four PJMs. The dashed line represents the average value.

B. RANS Mesh Independence Study – Suction Phase

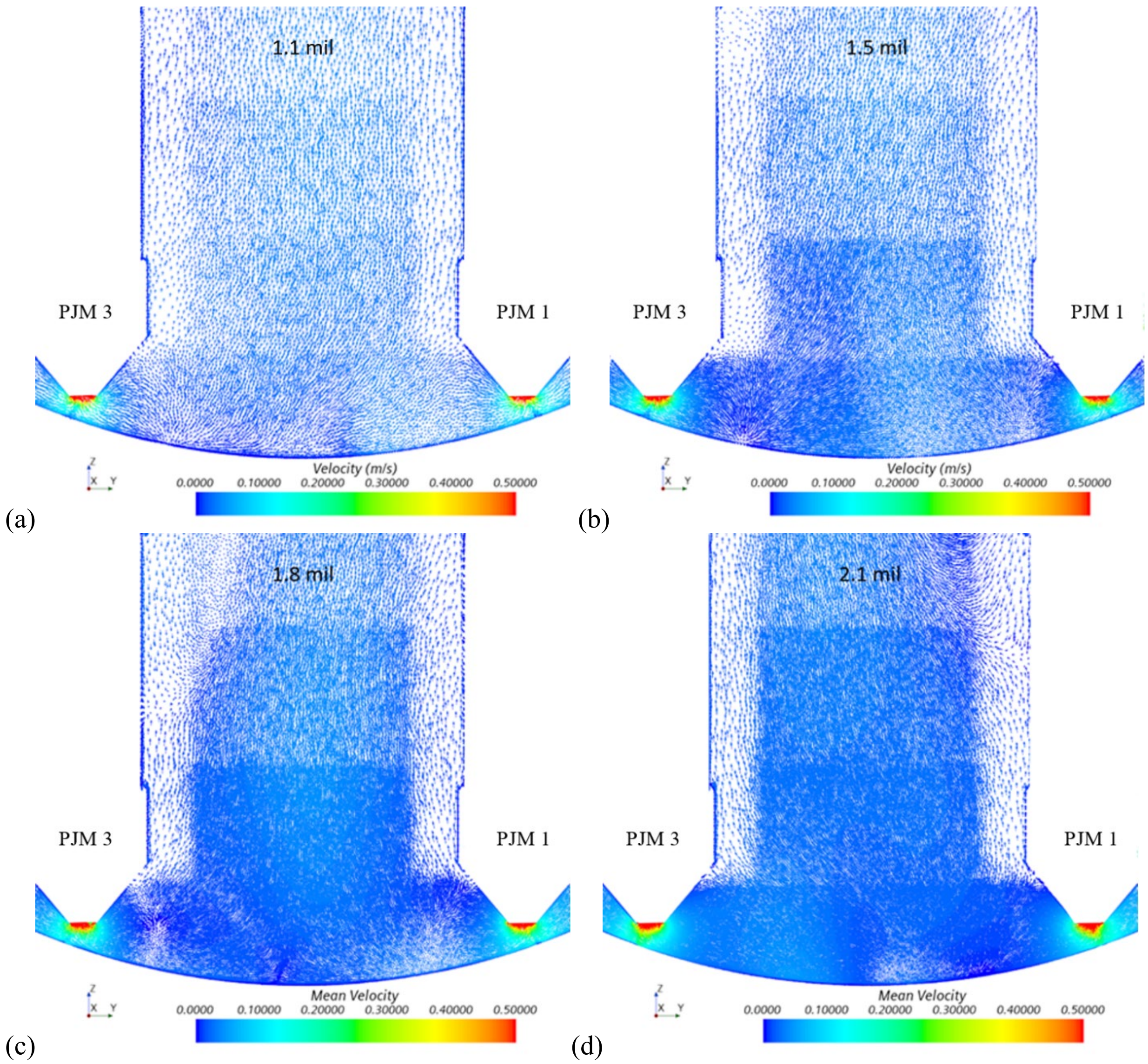

Figure 70. Velocity plots display predictions during a suction phase – (a) 1.1, (b) 1.5, (c) 1.8, and (d) 2.1 million Cells Mesh. RANS, UPP, Scenario 1.

C. LES Mesh Independence Study – Suction Phase

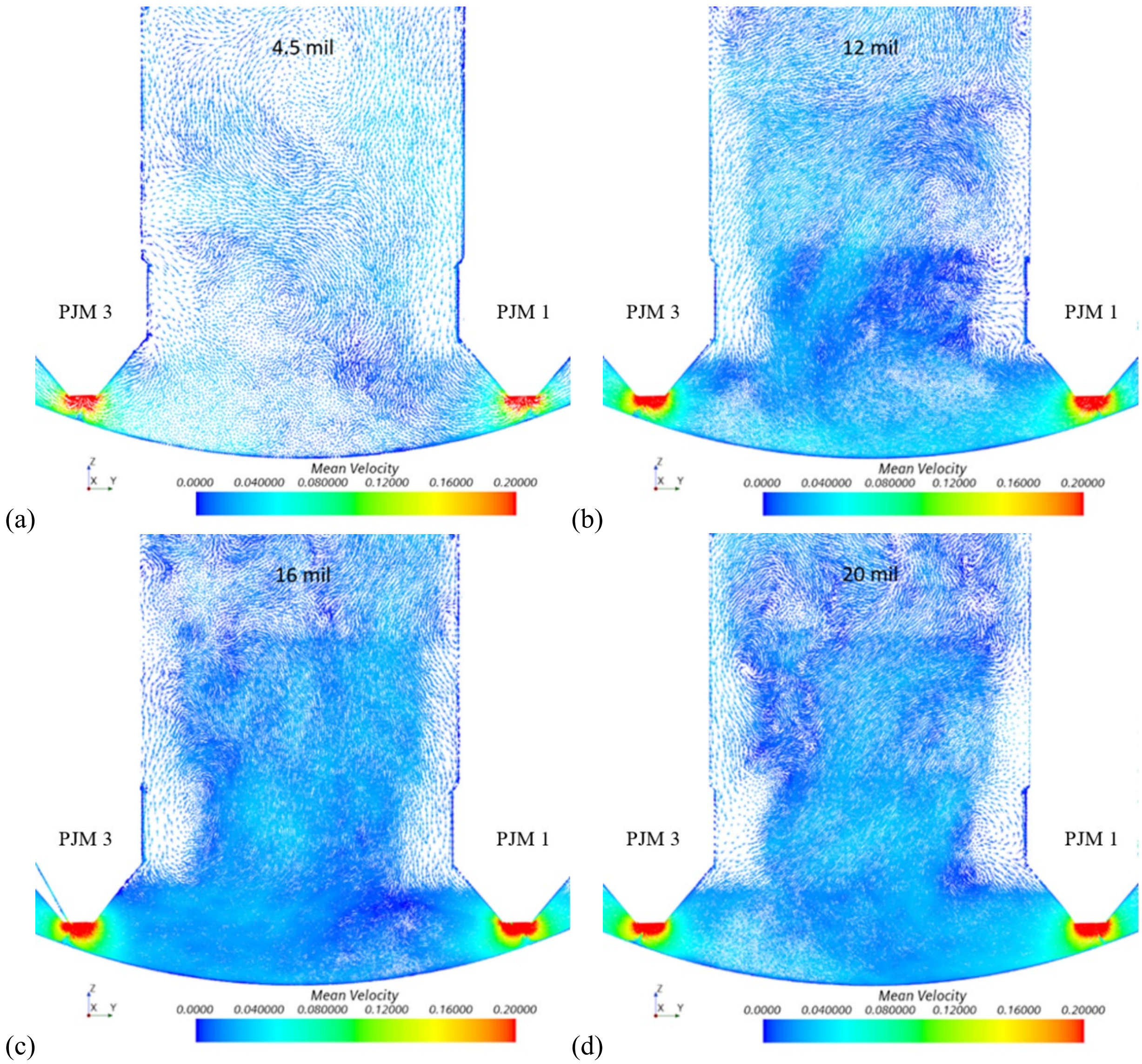

Figure 71. Velocity plots display predictions during a suction phase – (a) 1.1, (b) 1.5, (c) 1.8, and (d) 2.1 million Cells Mesh. LES, UPP, Scenario 1.

D. LBM Local Refinement Computation Time

Table 18. LBM Local Refinement Computation Time Comparison

LBM Grid	Length Scale (m)	Characteristic Velocity (m/s)	Reynolds Number, Re
LBM Grid Type	Uniform	Uniform	Local Refinement
Cell Count	2.1 million	16 million	7.7 million
Min. Cell Size	7.7 mm	3.8 mm	3.8 mm
Max. Cell Size	7.7 mm	3.8 mm	3.8 mm
CPU Time per Cycle*	~ 29 hr	~ 230 hr	~ 190 hr

E. LES RMS Velocity

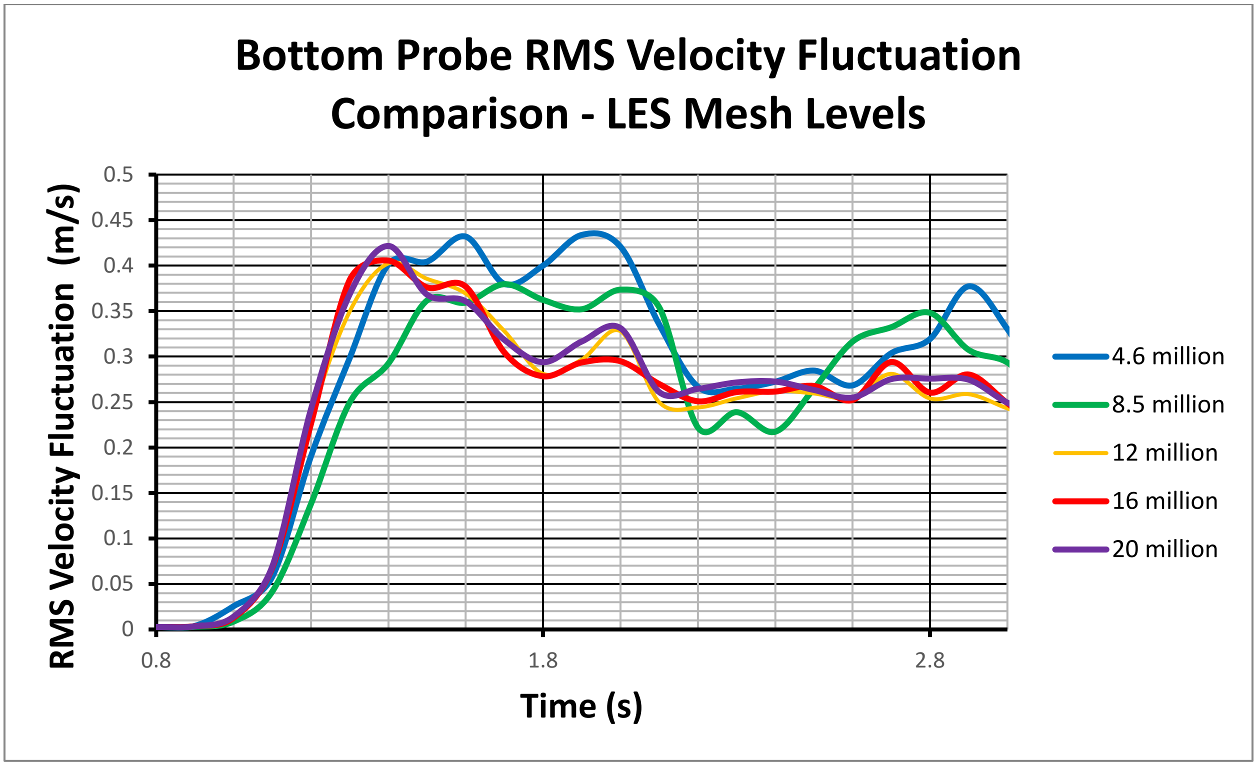

Figure 72. RMS velocity vs. Time at the bottom EM probe locations of Figure 12. Five curves represent data for mesh levels of 4.6, 8.5, 12, 16, and 20 million cells. Convergence behavior is identified at the 12 million cells level.

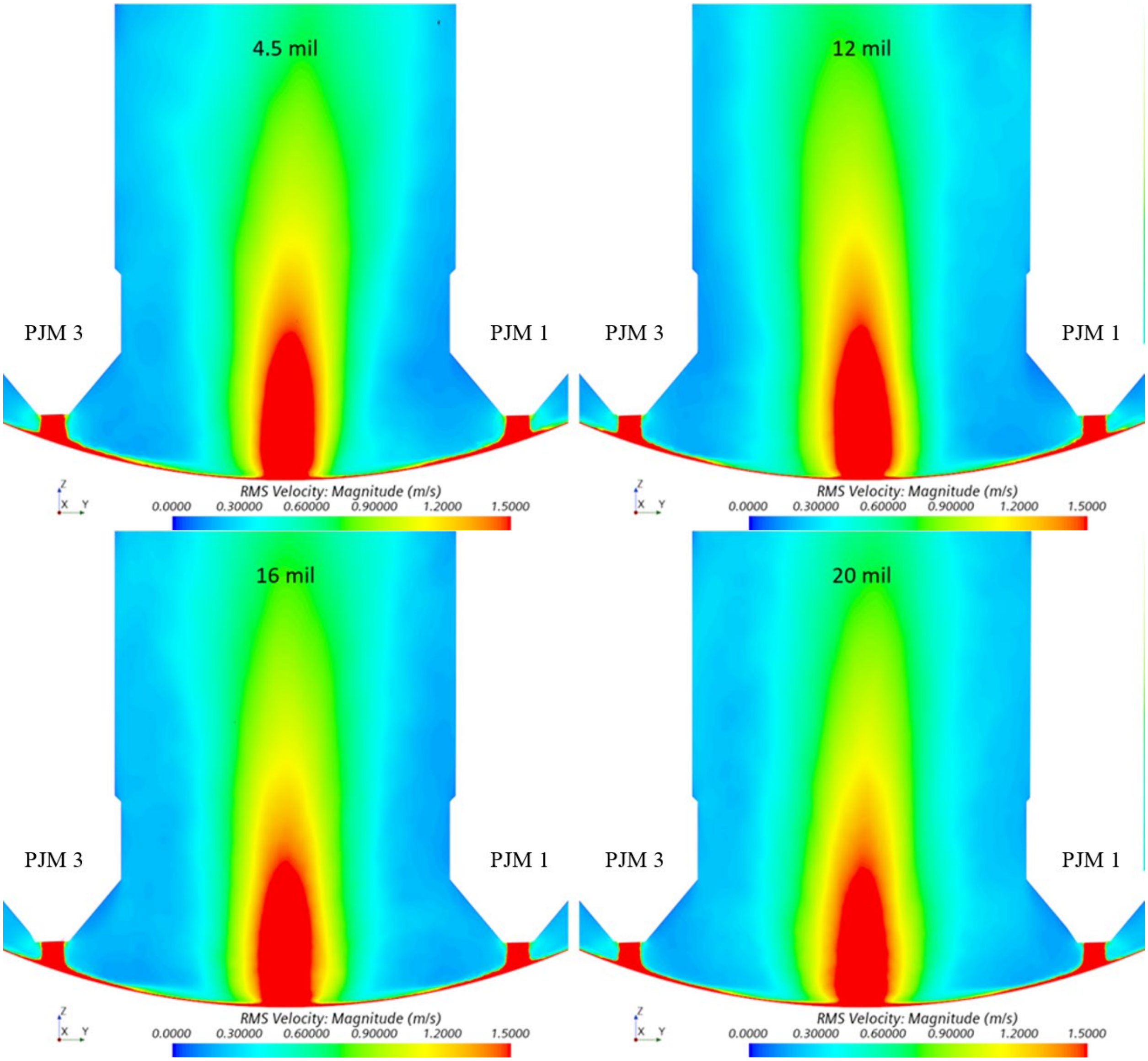

Figure 73. RMS velocity magnitude scalar plots on a vertical cross-sectional plane at the end of the drive phase. The four plots show the results from varying mesh levels with 4.5, 12, 16, and 20 million cells. Displayed velocities are the ensemble average over 100 cycles for each mesh level.

F. LBM RMS Velocity

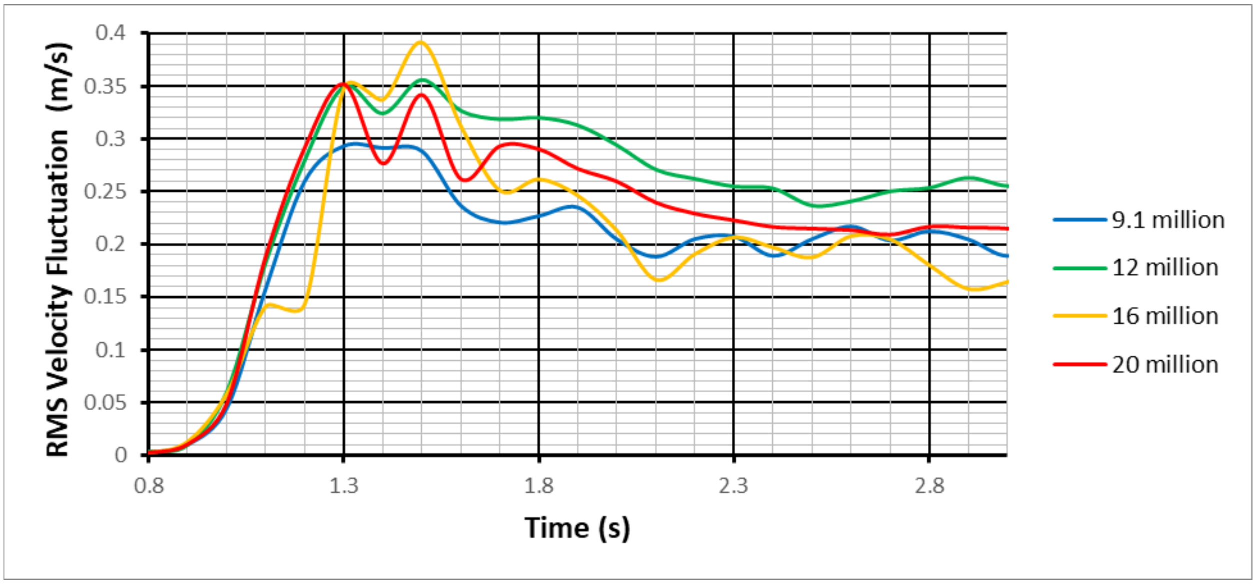

Figure 74. RMS velocity vs. Time at the three (bottom, middle, and top) EM probe locations of Figure 12. Five curves represent data for mesh levels of 4.6, 8.5, 12, 16, and 20 million cells. Convergence behavior is not identified.

G. Turbulence Metrics

i. LES vs. RANS

1. TKE

Scenario 1, LES vs. RANS, IPP, End of drive phase (t = 1.6 seconds).

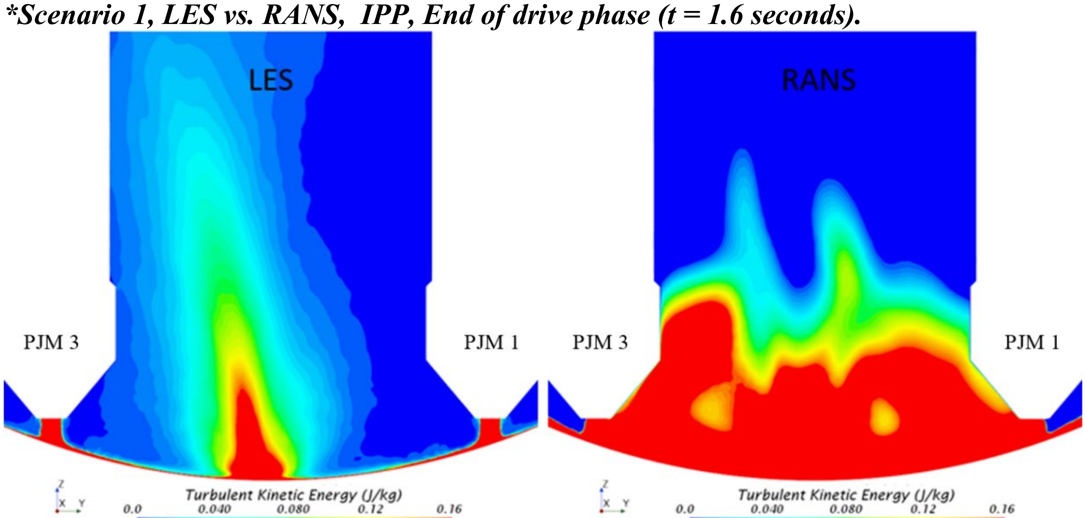

Figure 75. Turbulence Kinetic Energy (TKE) scalar contour plots from LES (left) and RANS (right). LES shows high values around the central plume. RANS shows high values around the bottom vortices.

***Scenario 1, LES vs. RANS, IPP, End of drive phase (t = 1.6 seconds).**

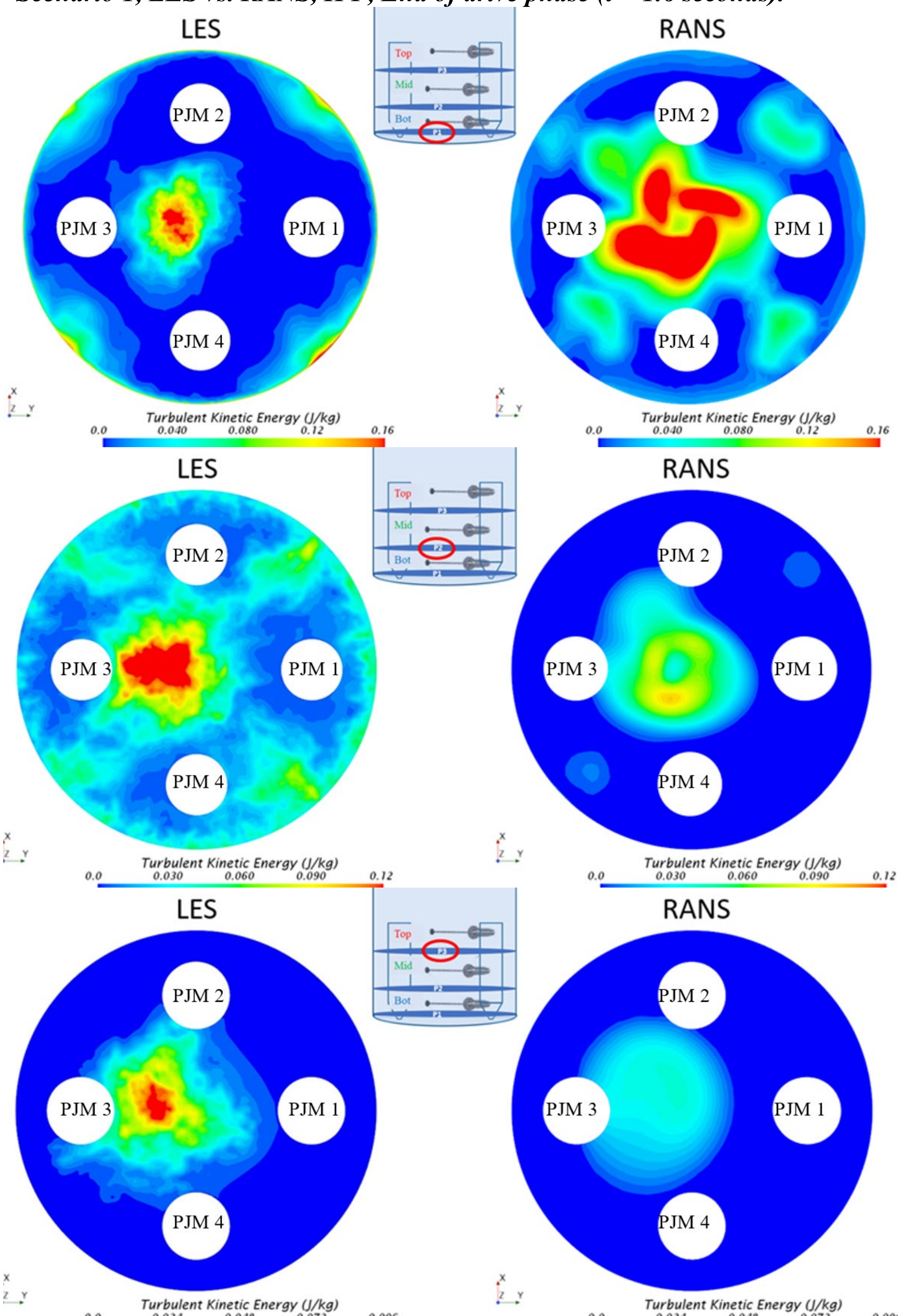

Figure 76. Turbulence Kinetic Energy from LES (left) and RANS (right) IPP cases reported on P1 (top row), P2 (middle row), and P3 (bottom row). In comparison to LES, RANS produces higher TKE on P1 and lower TKE on P2 and P3.

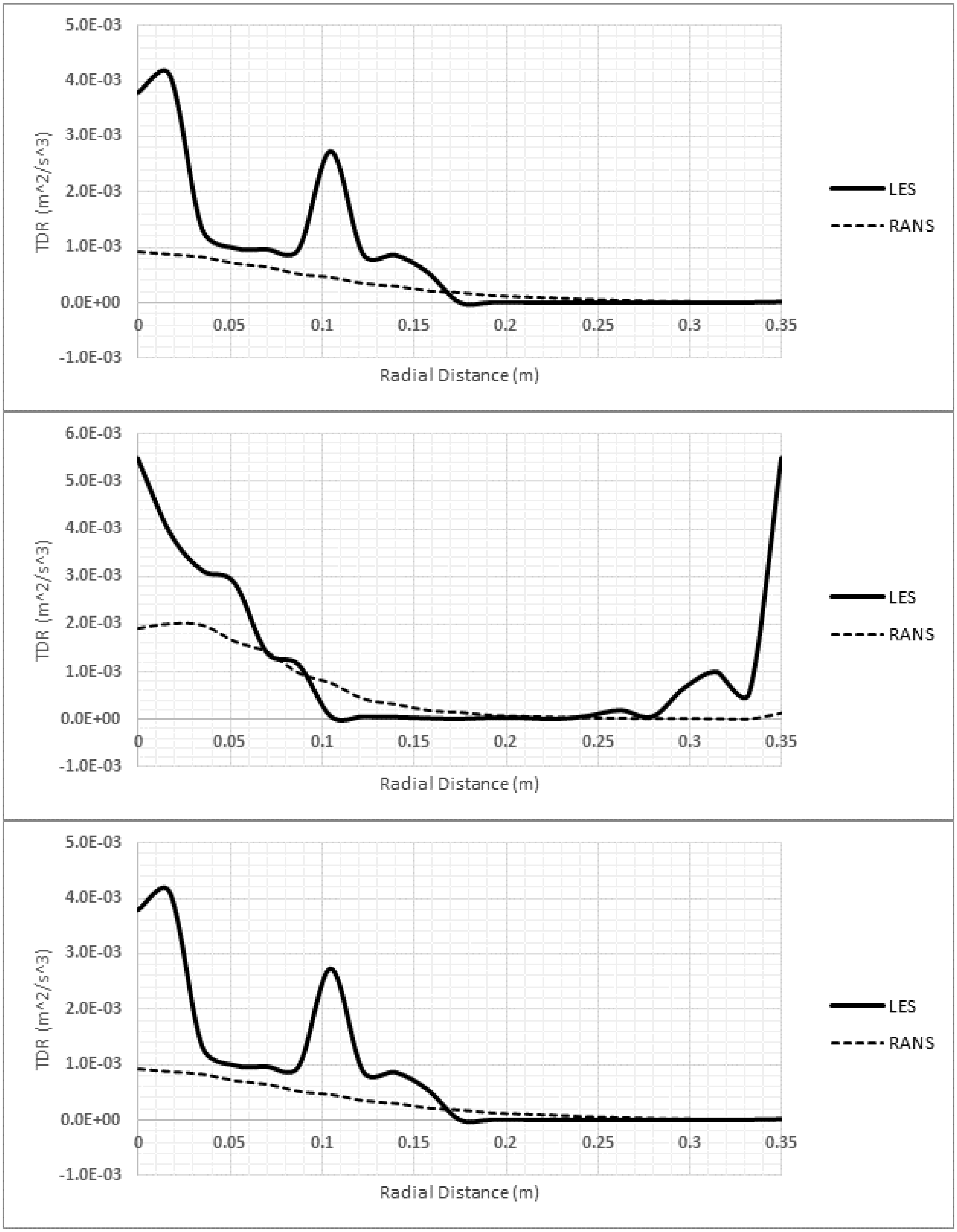

Figure 77. TDR data from LES (solid lines) and RANS (dashed lines) plotted against radial distance along the diagonal line (Figure 53). Overall, RANS produces higher TDR on P1, and LES produces higher TDR on P2 and P3.

2. *Turbulence Dissipation Rate*

Scenario 1, LES vs. RANS, IPP, End of drive phase (t = 1.6 seconds).

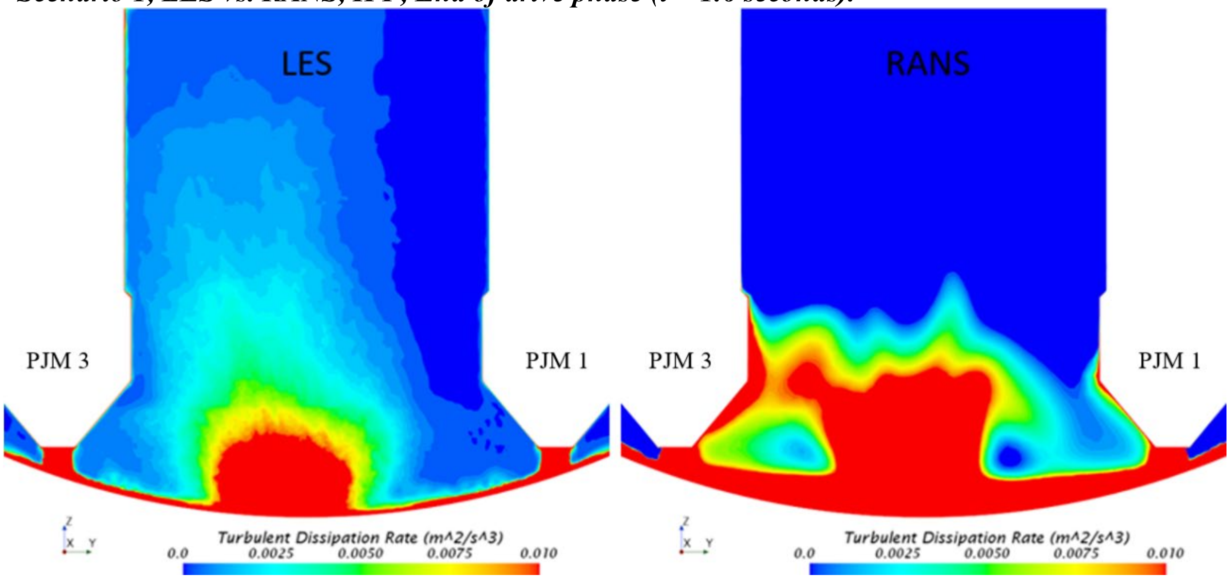

Figure 78. Turbulence Dissipation Rate (TDR) scalar contour plots from LES (left) and RANS (right). LES shows high values around the nozzles, dish bottom, and central plume. Larger areas are covered with high values in RANS especially around the exaggerated vortices captured in RANS (Figure 48).

Scenario 1, LES vs. RANS, IPP, End of drive phase (t = 1.6 seconds).

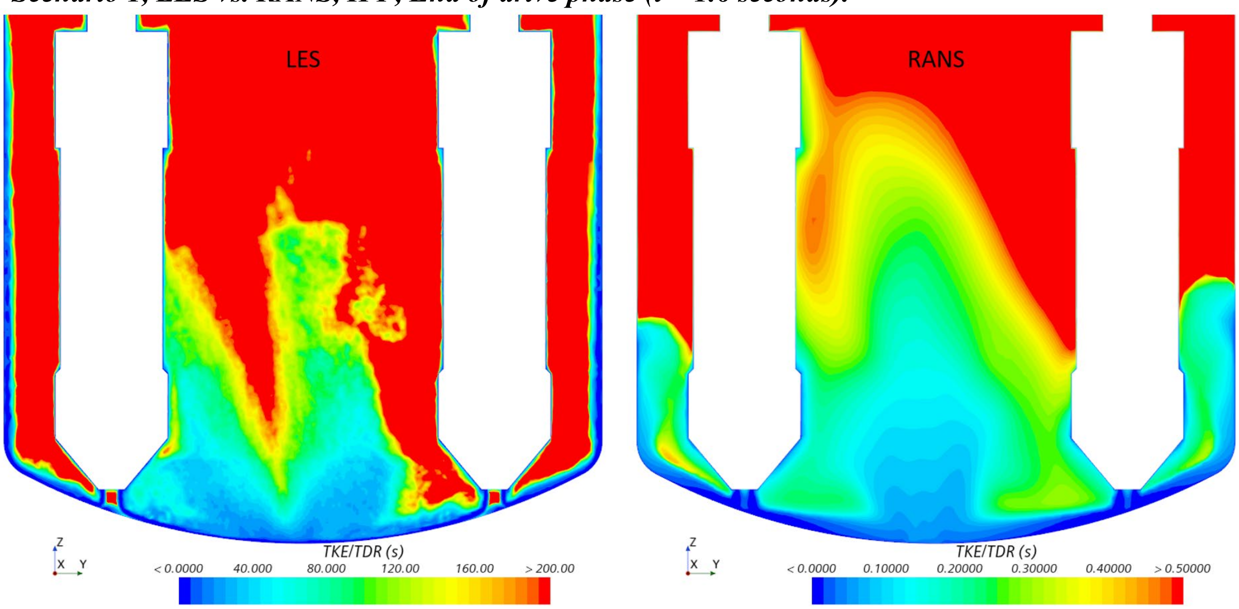

Figure 79. Scalar contour plots of the Turbulence Kinetic Energy over Turbulence Dissipation Rate (TDR) ratio from LES (left) and RANS (right). RANS predicts substantially higher TDR than LES, hence the scale of the ratio is much lower for RANS than for LES.

Scenario 1, LES vs. RANS, IPP, End of drive phase (t = 1.6 seconds).

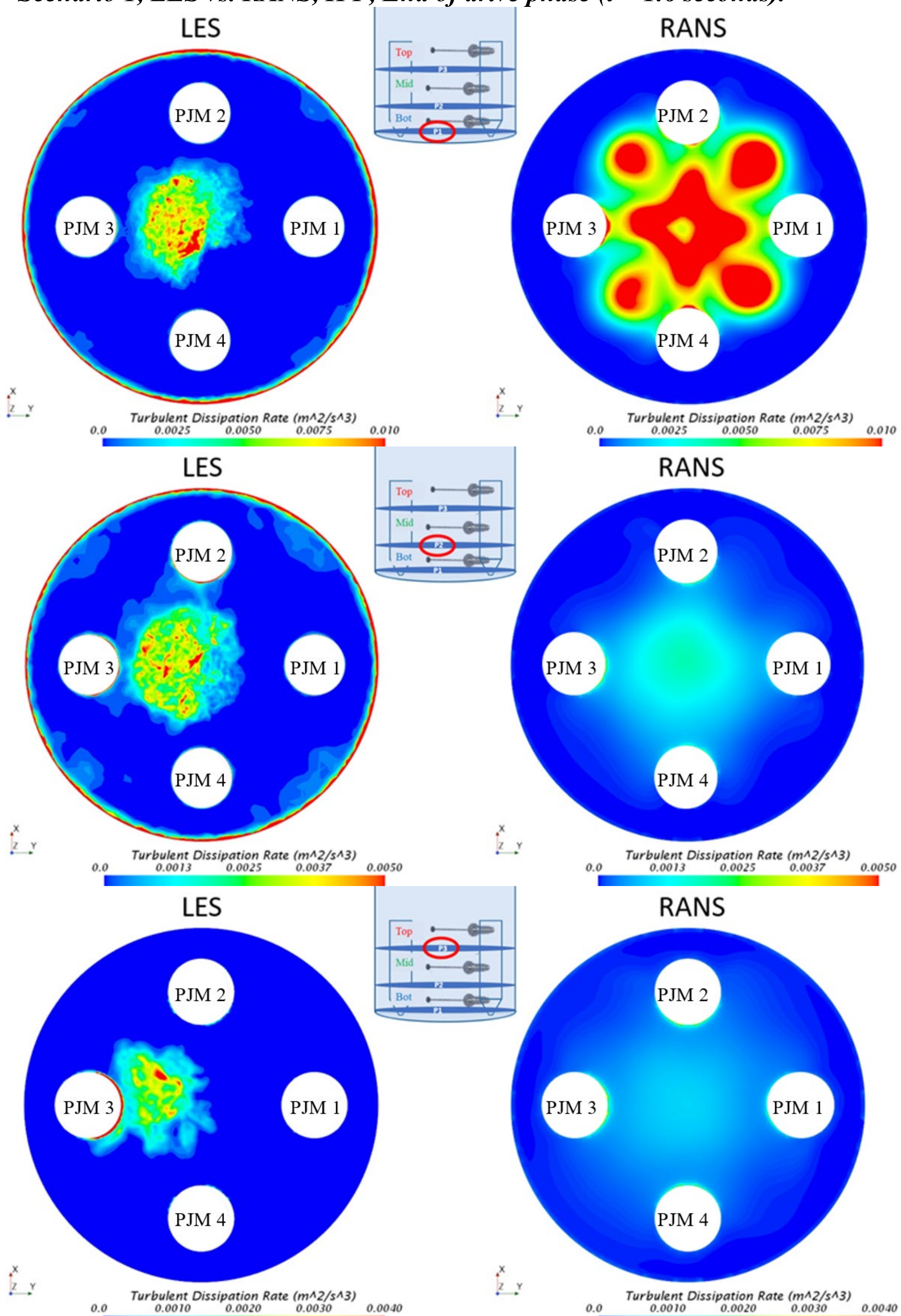

Figure 80. Turbulence Dissipation Rate (TDR) from LES (left) and RANS (right) IPP cases reported on P1 (top row), P2 (middle row), and P3 (bottom row). In comparison to LES, RANS produces higher TDR on P1 and lower TDR on P2 and P3.

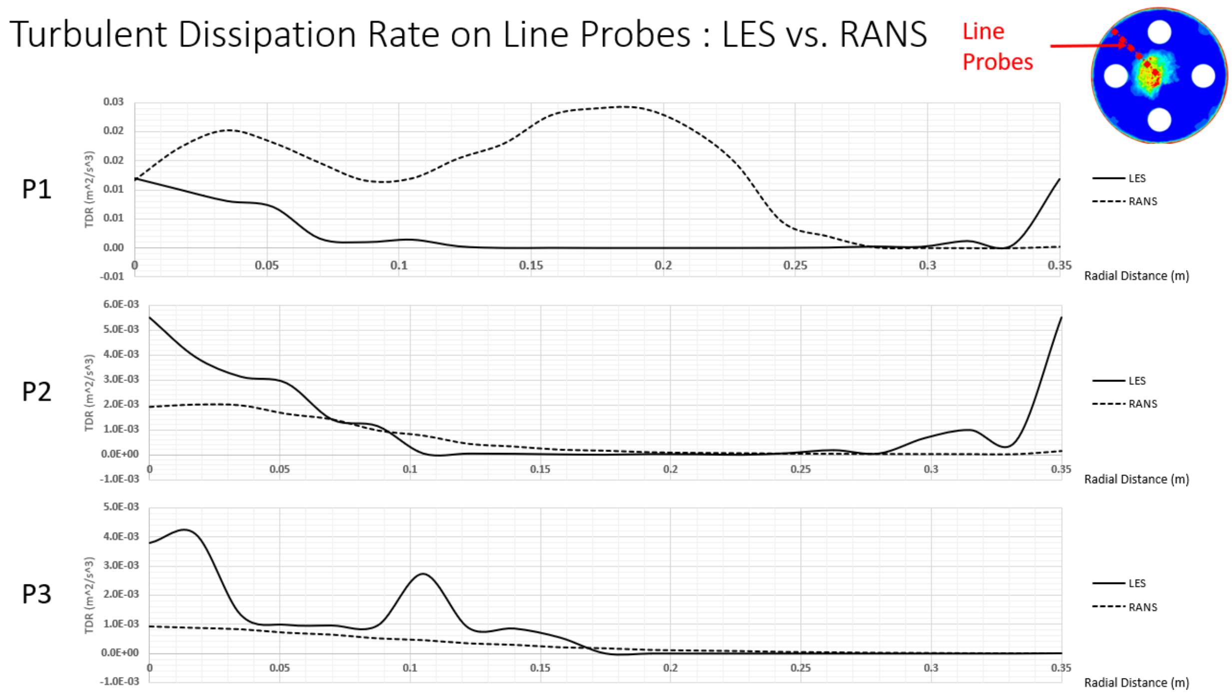

Figure 81. TKE data from LES (solid lines) and RANS (dashed lines) plotted against radial distance along the diagonal line (Figure 53). Overall, RANS produces higher TDR on P1, and LES produces higher TDR on P2 and P3.

3. *Turbulence Production*

Scenario 1, LES vs. RANS, IPP, End of drive phase (t = 1.6 seconds).

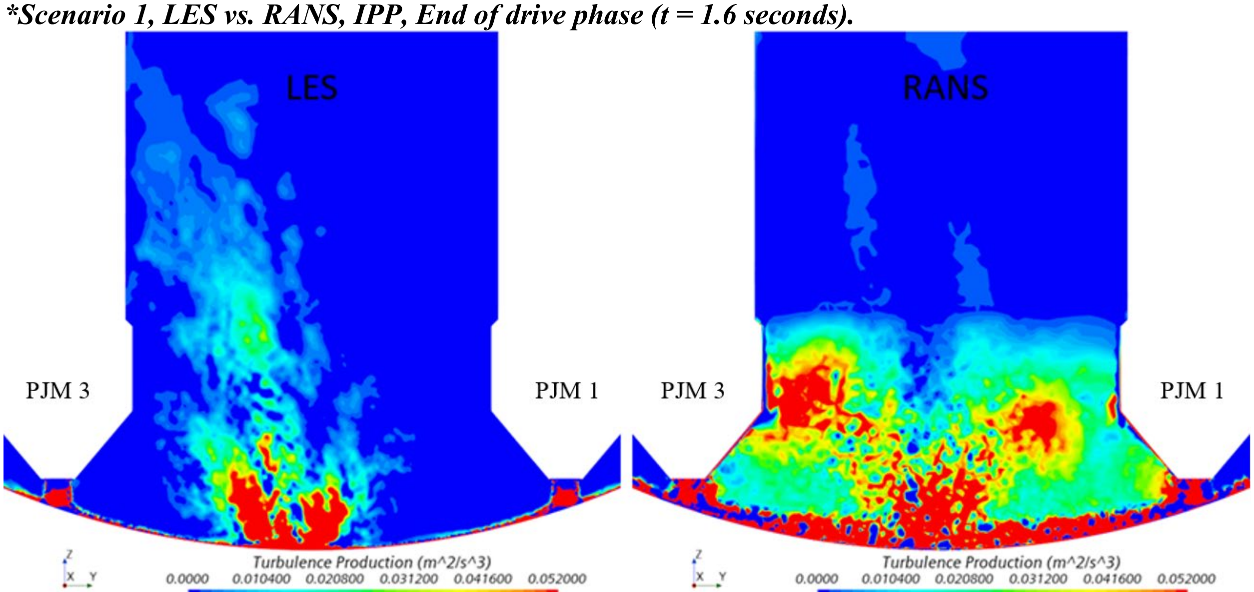

Figure 82. Turbulence production scalar contour plots from LES (left) and RANS (right). In the LES model, high turbulence production is shown in the central plume. In the RANS model, high turbulence production values shown generally in the bottom to middle region, especially near the dish bottom.

Scenario 1, LES vs. RANS, IPP, End of drive phase (t = 1.6 seconds).

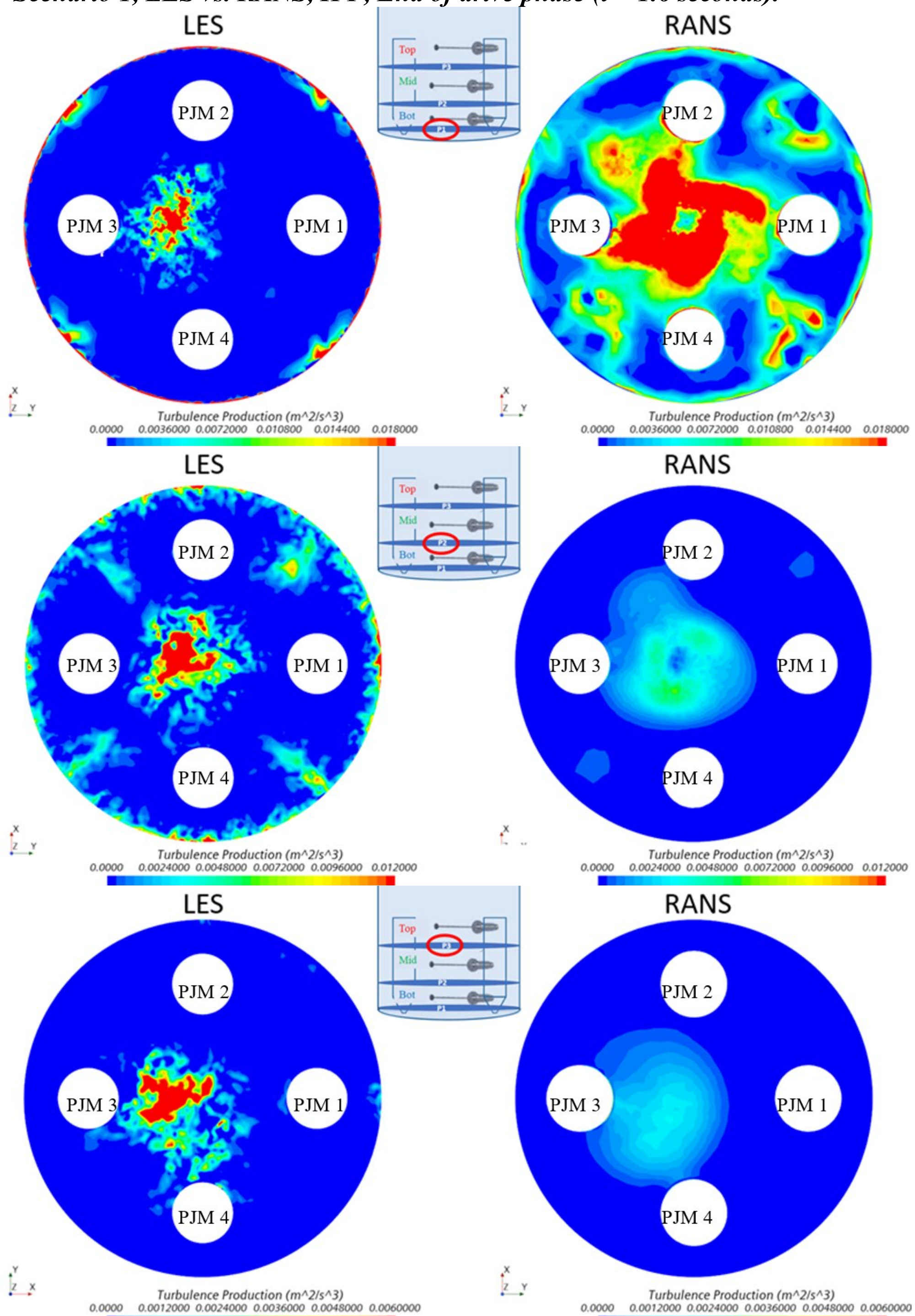

Figure 83. Turbulence production from LES (left) and RANS (right) IPP cases reported on P1 (top row), P2 (middle row), and P3 (bottom row). In comparison to LES, RANS produces higher turbulence production on P1 and lower turbulence production on P2 and P3.

ii. LES vs. LBM

1. TKE

***Scenario 1, LES vs. LBM, IPP, End of drive phase (t = 1.6 seconds).**

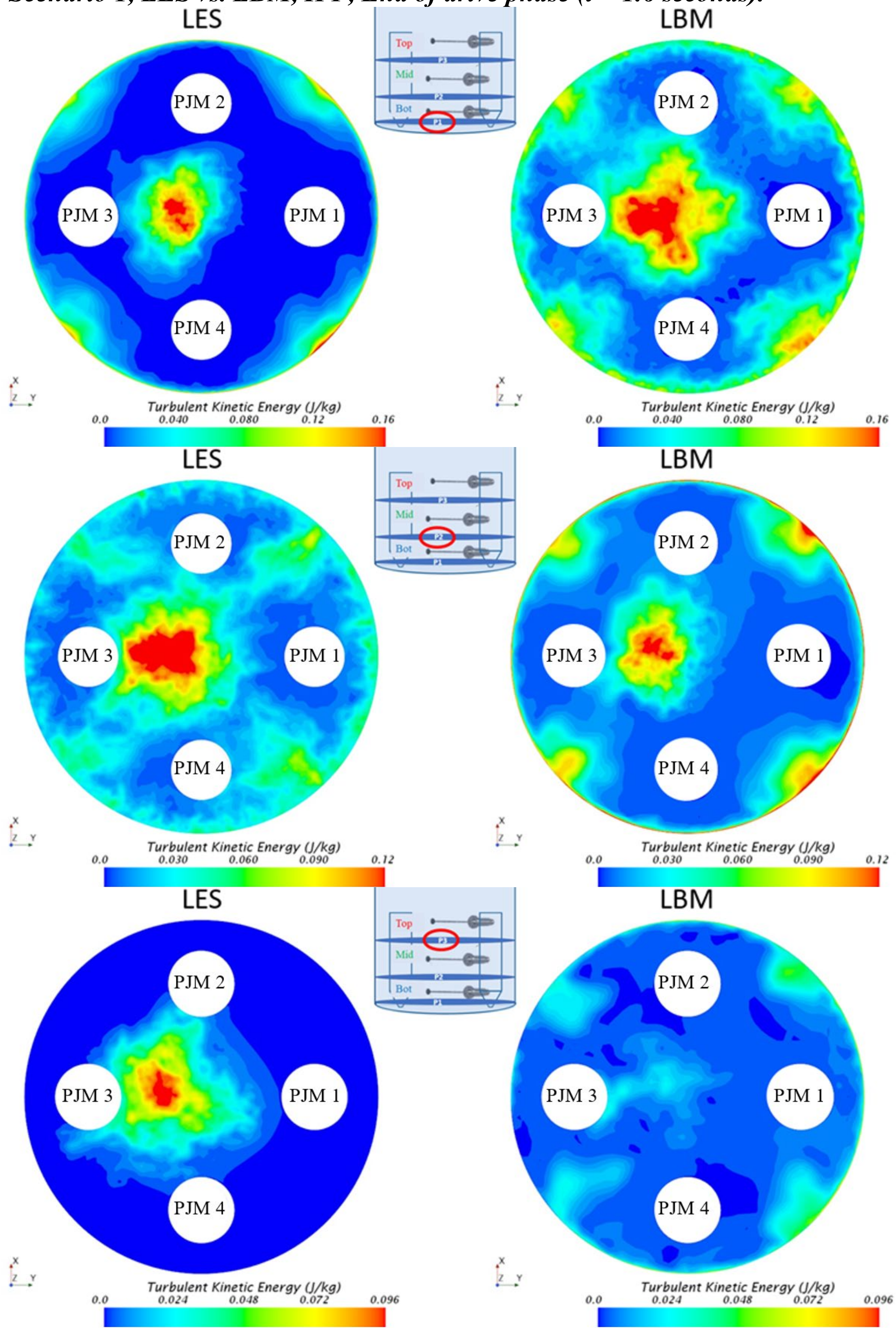

Figure 84. Turbulence Kinetic Energy from LES (left) and LBM (right) IPP cases reported on P1 (top row), P2 (middle row), and P3 (bottom row). In comparison to LES, LBM produces higher TKE near the curved boundaries (dish bottom and vessel wall).

2. *TDR*

Scenario 1, LES vs. LBM, IPP, End of drive phase (t = 1.6 seconds).

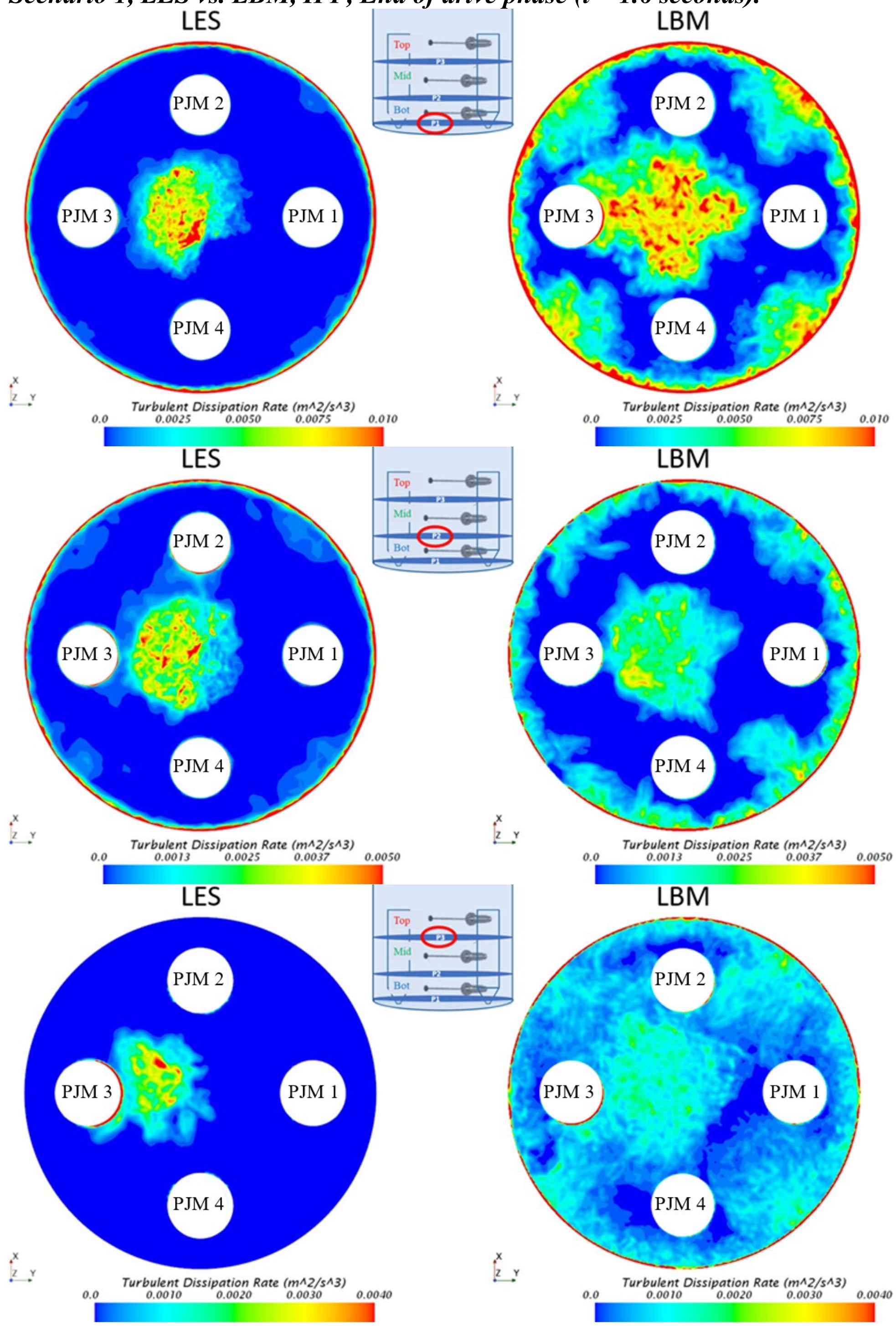

Figure 85. Turbulence Dissipation Rate (TDR) from LES (left) and LBM (right) IPP cases reported on P1 (top row), P2 (middle row), and P3 (bottom row). In comparison to LES, LBM produces higher TDR near the curved boundaries (dish bottom and vessel wall).

Scenario 1, LES vs. LBM, IPP, End of drive phase (t = 1.6 seconds).

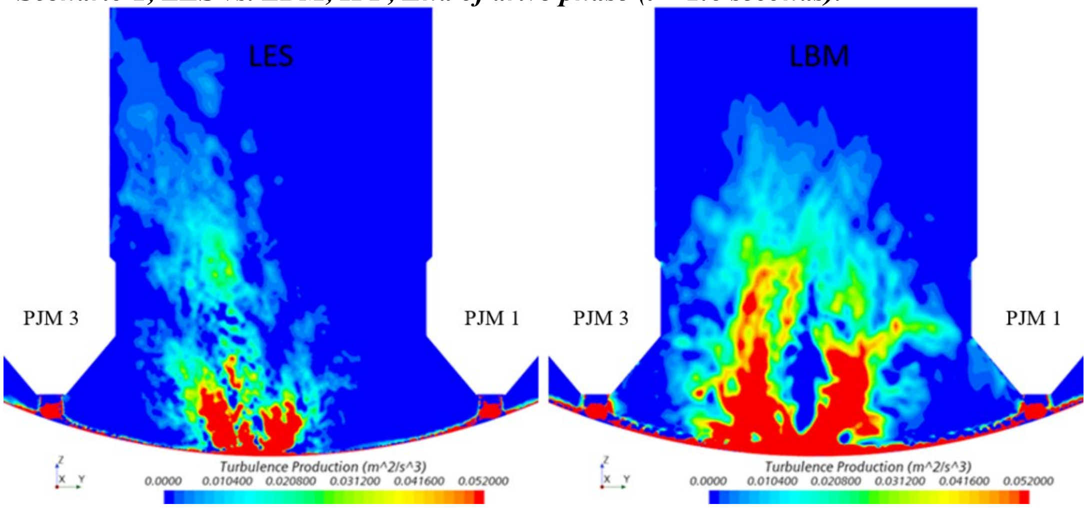

Figure 86. Turbulence production scalar contour plots from LES (left) and RANS (right). LES shows high values around the nozzles, dish bottom, and central plume. Larger areas are covered with high values in RANS especially around the exaggerated vortices captured in RANS (Figure 48).

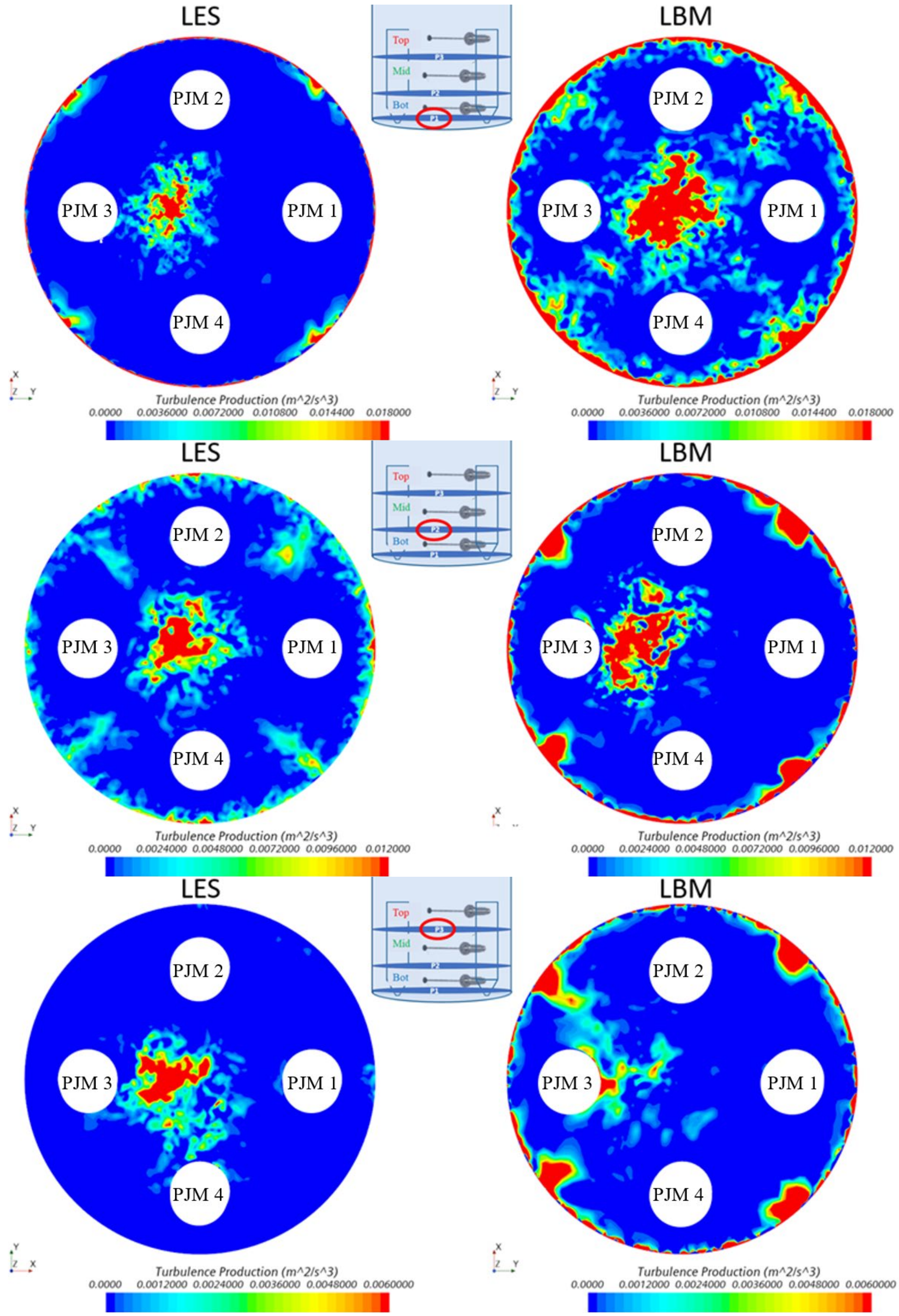

Figure 87. Turbulence production from LES (left) and LBM (right) IPP cases reported on P1 (top row), P2 (middle row), and P3 (bottom row). In comparison to LES, LBM produces higher turbulence production near the curved boundaries (dish bottom and vessel wall).

1. A list of publications on which the student is either the first author or a co-author. Provide the full citation (title, all authors, DOI, etc.). Subdivide into:

a. Publications that have appeared in print: specify full citation

- B.A. Minnick, J.W. Kim, D.I. Ko, R.V. Calabrese "Flow and power characteristics of an axial discharge rotor-stator mixer",Chem. Eng. Res. and Design, Vol. 136, pp. 477–490, (2018) doi: 10.1016/j.cherd.2018.05.015.

- Han, J. Y., Krasniqi, B., Kim, J., Keckley, M. & DeVoe, D. L. Minia-turization of hydrocyclones by high-resolution 3D printing forrapid microparticle separation. Adv. Mater. Technol. 5,1901105 (2020)

b. Publications that have been submitted and are under review: specify dates

c. Publications that will be submitted after the defense: specify tentative titles, and dates

- J. W. Kim, R. V. Calabrese "CFD Simulation of a Pulse Jet Mixed Vessel for Nuclear Waste Processing" Chem. Eng. Res. and Design. Sep. 2023

2. A list of conference presentations on which the student is either the first author or a co-author. Provide full details (title, authors, etc.). Specify speaker. Subdivide into:

a. Presentations that have been delivered

NAMF Mixing (XXVI) 2018: "CFD Simulation of a Pulse Jet Mixed Vessel"

AIChE 2017: (452d) "CFD Simulation of a Pulse Jet Mixed Vessel"

ASME 2016: "Verification and Validation Process of PJM Vessel CFD Simulations"

AIChE 2015: "(376b) CFD Simulation of a Pipeline Rotor-Stator Mixer"

AIChE 2015: "(301f) Comparison of PIV Measurements with CFD Simulation Results in a Rotor-Stator Mixer"

b. Presentations that have been scheduled (abstract accepted): specify dates

Mixing 17 (2023): "CFD Simulation of a Pulse Jet Mixed Vessel for Nuclear Waste Processing", July 2-5

c. Presentations for which abstracts will be submitted: specify tentative titles, and dates

Bibliography

[1] L. A. Hanson, "Radioactive waste contamination of soil and groundwater at the Hanford Site.," *Principles of Environmental Toxicology,* pp. 11-12, 2000.

[2] J. K. Fredrickson, J. M. Zachara, D. L. Balkwill and D. Kennedy, "Geomicrobiology of high-level nuclear waste-contaminated vadose sediments at the Hanford Site, Washington State.," *Applied and environmental microbiology ,* vol. 70, no. 7, pp. 4230-4241, 2004.

[3] A. Goel, J. S. McCloy, R. Pokorny and A. A. Kruger, "Challenges with vitrification of Hanford High-Level Waste (HLW) to borosilicate glass – An overview," *Journal of Non-Crystalline Solids,* 2019.

[4] J. A. FORT, P. A. Meyer, J. A. Bamberger, C. W. Enderlin, P. A. Scott, M. J. Minette and P. A. Gauglitz, "Scaled testing to evaluate pulse jet mixer performance in waste treatment plant mixing vessels," in *WM2010 Conference*, Pheonix, 2010.

[5] P. A. Meyer, "Pulse Jet Mixing Tests with Non-Cohesive Solids," Pacific Northwest National Laboratory, Richland, 2009.

[6] C. Xu and Y. Huang, "Maintenance-free pulse jet mixer," *Power Technology,* vol. 230, pp. 158-168, 2012.

[7] J. M. Bates, J. W. Brothers, J. M. Alzheimer, D. E. Wallace and P. A. Meyer, "Test results for pulse jet mixers in prototypic ultrafiltration feed process and high-level waste lag storage vessels," Pacific NorthWest, 2004.

[8] C. Guenther, B. Gopalan, D. Miller and R. Garg, "NETL's informational scoping-test data to support development of single-liquid assumption for WTP low-solids vessels," National Energy Technology Laboratory, Morgantown, WV, 2015.

[9] B. E. Wells, J. A. Bamberger and K. P. Recknagle, "Applying Hanford Tank Mixing Data to Define Pulse Jet Mixer Operation," in *ASME International Mechanical Engineering Congress and Exposition*, Houston, 2015.

[10] D. Liu, "Comparison of laminar model, RANS, LES and VLES for simulation of liquid sloshing," *Applied Ocean Research,* vol. 59, pp. 638-649, 2016.

[11] N. Gourdain, "Prediction of the unsteady turbulent flow in an axial compressor stage. Part 1: Comparison of unsteady RANS and LES with experiments," *Computers & Fields,* vol. 106, pp. 119-129, 2013.

[12] T. van Hooff, "On the accuracy of CFD simulations of cross-ventilation flows for a generic isolated building: Comparison of RANS, LES and experiments," *Building and Environment,* vol. 114, pp. 148-165, 2017.

[13] S. B. Pope, Turbulent Flows, New York: Cambridge University Press, 2000.

[14] F. Ducros, F. Nicoud and T. Poinsot, "Wall-Adapting Local Eddy-Viscosity models for simulations in complex geometries," *Numerical Methods for Fluid Dynamics ,* vol. VI, pp. 293-299, 1998.

[15] F. Nicoud and F. Ducros, "Subgrid-Scale Stress Modelling Based on the Square of the Velocity Gradient Tensor," *Flow, Turbulence and Combustion,* no. 62, pp. 183-200, 1999.

[16] Y. Yu, Q. Li, Z. X. Wen and R. Z. Huang, "Investigation on boundary schemes in lattice Boltzmann simulations of boiling heat transfer involving curved surfaces featured," *Physics of Fluids,* vol. 32, no. 6, 2020.

[17] R. Mei, W. Shyy, D. Yu and L.-S. Luo, "Lattice Boltzmann Method for 3-D Flows with Curved Boundary," *Journal of Computational Physics,* vol. 161, no. 2, pp. 680-699, 2000.

[18] E. Aslan, I. Taymaz and A. Benim, "Investigation of LBM curved boundary treatments for unsteady flows," *European Journal of Mechanics - B/Fluids,* vol. 51, pp. 68-74, 2015.

[19] A. Kajzer, J. Pozorski and K. Szewc, "Large-eddy simulations of 3D Taylor-Green vortex: comparison of Smoothed Particle Hydrodynamics, Lattice Boltzmann and Finite Volume methods," in *XXI Fluid Mechanics Conference*, Krakow, 2014.

[20] V. Schulz, N. Abbaspour and T. Baumeister, "Lattice-Boltzmann Simulation and Experimental Validation of a Microfluidic T-Junction for Slug Flow Generation," *ChemEngineering ,* vol. 3, no. 2, 2019.

[21] N. Mehdi, "Stirred Tank Fluid Flow Simulation With Two Lattice Boltzmann Methods," *JOURNAL OF SOLID MECHANICS IN ENGINEERING,* vol. 10, no. 2, pp. 21-33, 2017.

[22] W. S. Gosset, "The probable error of a mean," *Biometrika,* vol. 6, pp. 1-25, 1908.

[23] B. Godderidge, S. Tunock, C. Earl and M. Tan, "The effect of fluid compressibility on the simulation of sloshing impacts," *Ocean Engineering,* vol. 36, pp. 578-587, 1991.

[24] H. P. Tran and H. T. Ahn, "Air Compressibility Effect in CFD-based Water Inpact Analysis," *Journal of the Society of Naval Architects of Korea,* vol. 48, no. 6, pp. 581-591, 2011.

[25] E. de Villiers, "The Potential of Large Eddy Simulation for the Modeling of Wall Bounded Flows," *Imperial College of Science, University of London, UK,* vol. Thesis, 2006.

[26] A. Sadiki, S. Agrebi, M. Chrigui and A. Doost, "Analyzing the effects of turbulence and multiphase treatments on oxy-coal combustion process predictions using LES and RANS," *Chemical Engineering Science,* vol. 166, pp. 283-302, 2017.

[27] A. Sadiki, A. Maltsev, B. Wegner, F. Flemming, A. Kempf and J. Janicka, "Unsteady methods (URANS and LES) for simulation of combustion systems," *International Journal of Thermal Sciences,* vol. 45, pp. 760-773, 2006.

[28] T. Hilderman and D. Wilson, "Predicting plume meandering and averaging time effects on mean and fluctuating concentrations in atmospheric dispersion simulated in a water channel," *Boundary-Layer Meteorology,* vol. 122, pp. 535-575, 2007.

[29] Z. Jaworski and H. Murasiewicz, "LES and URANS modelling of turbulent liquid–liquid flow in a static mixer: Turbulent kinetic energy and turbulence dissipation rate," *Chemical Papers ,* pp. 182-192, 2010.

[30] S. Rhea, M. Bini and M. Fairweather, "RANS modelling and LES of a single-phase, impinging plane jet," *Computers & Chemical Engineering,* vol. 33, no. 8, pp. 1344-1353, 2009.

[31] L. W. Chew, "Buoyant flows in street canyons: comparison of RANS and LES at reduced and full scales," *Building and Environment,* vol. 146, pp. 77-87, 2018.

[32] Y. Yang, S. C. Chang and C. Chiou, "Lattice Boltzmann method and large-eddy simulation for turbulent impinging jet cooling," *International Journal of Heat and Mass Transfer,* vol. 61, pp. 543-553, 2013.

[33] R. Kao and R. Yang, "An investigation into curved and moving boundarytreatments in the lattice Boltzmann method," *Journal of Computational Physics,* vol. 227, pp. 5671-5690, 2008.

[34] R. Mei, L. Luo and W. Shyy, "An accurate curved boundary treatment in the Lattice Boltzmann Method," *Journal of Computational Physics,* vol. 155 , pp. 307-330, 1999.

[35] Z. Guo and C. Zheng, "An extrapolation method for boundary conditions in lattice Boltzmann method," *Phys. Fluids,* vol. 14, pp. 2007-2010, 2002.

[36] P. A. Meyer and A. W. Etchells, "Mixing with Intermittent Jets with Application in Handling radioactive Waste Sludges," *Chemical Engineering Research and Design,* vol. 85, no. A5, pp. 691-696, 2007.

[37] H. Wurps, G. Steinfeld and S. Heinz, "Grid-Resolution Requirements for Large-Eddy Simulations of the Atmospheric Boundary Layer," *Boundary-Layer Meteorology,* vol. 175, pp. 179-201, 2020.

[38] V. Michelassi and J. G. Wissink, "Turbulent Kinetic Energy Production in the Vane of a Low-Profile Linear Turbine Cascade with Incoming Wakes," *Internaltional Journal of Rotating Machinery,* 2015.

[39] O. Filippova and D. Hänel, "Grid refinement for lattice-BGK models," *Journal of Computational Physics,* vol. 147 , pp. 219-228, 1998.

[40] P. Durbin, "Near-wall turbulence closure modeling without damping functions," *Theoretical and Computational Fluid Dynamics,* vol. 3, pp. 1-13, 1991.

[41] L. Stival, J. Brinkerhoff, J. Vedovotto and F. Oliveira de Andrade, "Wake modeling and simulation of an experimental wind turbine using large eddy simulation coupled with immersed boundary method alongside a dynamic adaptive mesh refinement," *Energy Conversion and Management,* vol. 268, 2022.

[42] C. Lyu, P. Liu and T. Hu, "Hybrid method for wall local refinement in lattice Boltzmann method simulation," *Physics of Fluids,* no. 35, 2023.

[43] Z. Liu, J. Ruan, W. Song, L. Zhou, W. Guo and J. Xu, "Parallel Scheme for Multi-Layer Refinement Non-Uniform Grid Lattice Boltzmann Method Based on Load Balancing," vol. 15, no. 7884, 2022.